Czech
Technical
University
in Prague

F3

Faculty of Electrical Engineering
Department of Circuit Theory

Master's Thesis

Optimizing an EIT-Oxygenator Interface for Early Blood Clot Detection

Filip Šlapal

Supervisor: **Diogo Silva, M.Sc. (RWTH Aachen University, Germany)**
Second supervisor: **Ing. Jan Havlík, PhD.**
Field of study: **Medical Electronics and Bioinformatics**
Subfield of study: **Medical Instrumentation**
Turn-in date: **August 2023**

MASTER‘S THESIS ASSIGNMENT

I. Personal and study details

Student's name: **Šlapal Filip**
Personal ID number: **474446**
Faculty / Institute: **Faculty of Electrical Engineering**
Department / Institute: **Department of Circuit Theory**
Study program: **Medical Electronics and Bioinformatics**
Specialisation: **Medical Instrumentation**

II. Master’s thesis details

Master’s thesis title in English:

Optimizing an EIT-Oxygenator Inferface for Early Blood Clot Detection

Master’s thesis title in Czech:

Optimalizace rozhraní EIT-Oxygenátor pro brzkou detekci krevních sraženin

Guidelines:

Extracorporeal membrane oxygenation (ECMO) is a technique widely used for therapeutics and surgical interventions in the scope of cardiorespiratory conditions. Oxygenators are crucial devices for this technique, which allows carbon dioxide to be removed from incoming blood, and oxygen to be absorbed by it. However, given this effect is ensured by forcing the blood through a closed compartment with semipermeable microfibers, there is a high chance of hemostasis and clotting, both often fatal. The use of heparin-coated fibers mitigates this issue, but might result in hemorrhaging, and allergic or inflammatory reactions.
A non-invasive, early detection system embedded in the device could prevent further clotting without additional substances. Electrical impedance tomography (EIT) is a non-invasive imaging technique which allows conductivity maps from within a structure coated by electrodes to be reconstructed in real-time. Since blood clots have different conductivity than blood, these could be detected and characterized using EIT. Additionally, this method could provide spatiotemporally resolved data useful for investigating and preventing hemostasis and thrombosis using different strategies (e.g. control).
The goal of this thesis is to enhance a pre-existing EIT-Oxygenator interface by selecting injection-measurement EIT patterns, electrode configurations, and image reconstruction and processing software to optimize clot detection and classification capability of the system. Finally, the concept will be validated through FEM simulations and blood experiments.
Guidelines:

- Simulation of prototype electrode configurations, and injection-measurement patterns in EIDORS, and selection of the best parameters according to defined figures of merit
- Investigation and implementation of image reconstruction and processing techniques to optimally reconstruct blood clots
- Development of robust post-processing approaches to identify and characterize blood clots
- Validation of the final setup with ground-truth obtained from blood trials with the prototype

Bibliography / sources:

[1] Leonhardt, Steffen, and Burkhard Lachmann. 2012. “Electrical Impedance Tomography: The Holy Grail of Ventilation and Perfusion Monitoring?” Intensive Care Medicine 38 (12): 1917–29. https://doi.org/10.1007/s00134-012-2684-z.
[2] Dowrick, T, C Blochet, and D Holder. 2015. “In Vivo Bioimpedance Measurement of Healthy and Ischaemic Rat Brain: Implications for Stroke Imaging Using Electrical Impedance Tomography.” Physiological Measurement 36 (6): 1273–82. https://doi.org/10.1088/0967-3334/36/6/1273.
[3] Nguyen, D., W. Chik, R. Kosobrodov, M. Barry, J. Pouliopoulos, C. Jin, A. McEwan, and A. Thiagalingam. 2013. “Pulmonary Embolism Detection with Electrical Impedance Tomography.” Heart, Lung and Circulation 22 (January): S192–93. https://doi.org/10.1016/j.hlc.2013.05.459.
[4] Dornia, Christian, Alois Philipp, Stefan Bauer, Matthias Lubnow, Thomas Müller, Karla Lehle, Christof Schmid, et al. 2014. “Analysis of Thrombotic Deposits in Extracorporeal Membrane Oxygenators by Multidetector Computed Tomography.” ASAIO Journal 60 (6): 652–56. https://doi.org/10.1097/MAT.0000000000000133.
[5] Conway, Robert G, Jiafeng Zhang, Jean Jeudy, Charles Evans, Tieluo Li, Zhongjun Jon Wu, and Bartley P Griffith. 2021. “Computed Tomography Angiography as an Adjunct to Computational Fluid Dynamics for Prediction of Oxygenator Thrombus Formation.” Perfusion 36 (3): 285–92. https://doi.org/10.1177/0267659120944105.
[6] Kaesler, Andreas, Felix Hesselmann, Mark O. Zander, Peter C. Schlanstein, Georg Wagner, Philipp Bruners, Thomas Schmitz Rode, Ulrich Steinseifer, and Jutta Arens. 2019. “Technical Indicators to Evaluate the Degree of Large Clot Formation Inside the Membrane Fiber Bundle of an Oxygenator in an In Vitro Setup.” Artificial Organs 43 (2): 159–66. https://doi.org/10.1111/aor.13343.

Name and workplace of master’s thesis supervisor:

Diogo Silva, MSc.   RWTH Aachen University

Name and workplace of second master’s thesis supervisor or consultant:

Ing. Jan Havlík, Ph.D.   Department of Circuit Theory, FEE

Date of master’s thesis assignment: **16.02.2023**   Deadline for master's thesis submission: **31.08.2023**

Assignment valid until: **22.09.2024**

Diogo Silva, MSc. Supervisor’s signature	doc. Ing. Radoslav Bortel, Ph.D. Head of department’s signature	prof. Mgr. Petr Páta, Ph.D. Dean’s signature

III. Assignment receipt

The student acknowledges that the master’s thesis is an individual work. The student must produce his thesis without the assistance of others, with the exception of provided consultations. Within the master’s thesis, the author must state the names of consultants and include a list of references.

.

Date of assignment receipt   Student’s signature

Acknowledgements

I would like to thank everyone who helped me throughout the whole double-degree program at RWTH and during the completion of this thesis. First and foremost, I would like to thank to my supervisor Diogo Silva, M.Sc. for his encouragement and insightful feedback during the thesis development. I would also like to extend my appreciation to my CTU supervisor, Ing. Jan Havlík, Ph.D., for unwavering support and an ever-present willingness to help.

My heartfelt appreciation goes to my family for their unconditional support, love and encouragement. Their attitude has been a source of motivation for me throughout the whole German adventure. Last but not least, a huge thanks goes to my former girlfriend, who became my wife during my work on this thesis. I am extremely grateful for the time you invested in the thesis including countless hours of thesis related discussions and proofreading of the draft. I am looking forward to spending the following years by your side.

Some of computational resources were provided by the e-INFRA CZ project (ID:90254), supported by the Ministry of Education, Youth and Sports of the Czech Republic. Thank you very much for providing the scientific community with such amazing possibilities.

Declaration

I declare that the presented work was developed independently and that I have listed all sources of information used within it in accordance with the methodical instructions for observing the ethical principles in the preparation of university theses.

In Prague, on ______________

____
Signature

Abstract

Thrombus formation and deposition is the most frequent reason for a forced oxygenator exchange during extracorporeal support. However, the risk of complication is much higher for these emergent oxygenator exchanges as opposed to planned ones, which is especially dangerous for patients in a critical state. They are the ones who can most benefit from a reliable method for early blood clot detection. This master's thesis focuses on utilizing electrical impedance tomography (EIT) for oxygenator blood clot detection. During the course of this work, a complete optimization pipeline was designed and implemented in MATLAB. Electrode positions and injection-measurement (I-M) pattern were optimized first, which lead to more homogeneous and sensitive measurements. Next, two reconstruction algorithms were used to reconstruct thrombi in the 3D space of the oxygenator. A Graz consensus Reconstruction algorithm for EIT (GREIT) reconstruction matrix was trained on targets emphasizing reconstruction mainly in areas with a higher likelihood of thrombi deposition (oxygenator edges and corners). A LeNet reconstruction convolutional neural network (CNN) was trained as well. Thrombus detection and thrombosis severity assessment followed. Four fully connected (FC) neural networks were trained to detect clots and assess thrombosis severity based on voltage measurements and reconstructed images. Information from the voltage measurements turned out to be more useful for classification, whose final accuracy reached over 90 %. The proposed approaches were evaluated on real oxygenator mock. It was shown that oxygenator clot detection with EIT should be possible and is worth further research. The entire optimization pipeline was set up to facilitates easy modifications of the implemented algorithms in the future. In this way it, the thesis enables simple research continuity.

Keywords:

electrical impedance tomography, extracorporeal membrane oxygenation, membrane oxygenator, thrombi, electrode optimization, image reconstruction, thrombi detection, neural networks

Abstrakt

Vznik a depozice trombů je nejčastější příčinou pro nucenou výměnu oxygenátorů při mimotělní podpoře krevního oběhu. Výskyt komplikací je ovšem mnohem častější v případě nucené výměny než u výměny plánované. Neplánovaná výměna je extrémně nebezpečná především pro pacienty v kritickém stavu. Spolehlivá metoda pro včasnou detekci trombů v oxygenátorech by tedy byla velmi přínosná. Tato diplomová práce se soustředí na využití elektrické impedanční tomografie (EIT) pro detekci krevních sraženin v oxygenátorech. V rámci práce byl v MATLABu navržen a implementován kompletní nástroj pro optimalizaci EIT měření. Nejprve byly optimalizovány pozice elektrod a metoda pro vysílání a snímání signálu, což vedlo k homogennějším a citlivějším měřením. Následně byly použity dva algoritmy pro rekonstrukci trombů v 3D prostoru oxygenátoru. Rekonstrukční matice GREIT (*Graz consensus Reconstruction algorithm for EIT*) byla natrénována na sraženinách v oblastech vysoké pravděpodobnosti vzniku trombů (hrany a rohy oxygenátoru) v rámci optimalizace rekonstrukce. Dále byla natrénována konvoluční neuronová síť architektury LeNet. Následovala detekce trombů a určení závažnosti krevních sraženin. Za tímto cílem byly natrénovány čtyři neuronové sítě z plně propojených vrstev. Vstupem pro ně byly napětí z elektrod a také rekonstruovaný obraz. Ukázalo se, že napětí jsou pro klasifikaci výrazně užitečnějším vstupem a výsledná přesnost klasifikace překročila 90 %. Navržené postupy byly ověřeny na reálném modelu oxygenátoru. Výsledky práce ukazující potenciál využití EIT pro detekci krevních sraženin v oxygenátorech. V rámci práce vznikl komplexní a snadno modifikovatelný nástroj, který může pomoci v budoucímu výzkumu problematiky.

Klíčová slova:

elektrická impedanční tomografie, extrakorporální membránová oxygenace, membránový oxygenátor, krevní sraženiny, optimalizace elektrod, rekonstrukce obrazu, detekce krevních sraženin, neuronové sítě

Contents

Part I
Theoretical background and literature research

Part II
Materials and Methods

Part III
Results and Discussion

Appendices

Figures

Tables

Used acronyms

AR amplitude response 22, 24, 53, 89, 90

ARDS acute respiratory distress syndrome 8

CDF cumulative distribution function 40–42

CEM complete electrode model 17, 22

CNN convolutional neural network vi, 54, 98

CO_2 carbon dioxide 7, 11, 13

CoG center of gravity 23, 24

CT computed tomography 15, 20

ECLS extracorporeal life support 8

ECMO extracorporeal membrane oxygenation x, 1, 2, 5, 7–14

EIDORS Electrical Impedance and Diffuse Optical tomography Reconstruction Software 36, 42, 43, 48, 53, 89, 98

EIT electrical impedance tomography vi, 2, 5, 14–20, 22, 23, 25, 26, 36, 52, 54, 56, 67, 71, 79, 98, 99

ELSO Extracorporeal Life Support Organization 8

FC fully connected vi, 27, 28, 30, 50, 55–58, 60, 98

FEM finite element method 17, 22, 23, 36–38, 40, 42, 48

FoM figures of merit xi, 22–24, 53, 89, 90

FP forward problem 16, 17, 20, 37, 43

GREIT Graz consensus Reconstruction algorithm for EIT vi, xi–xiv, 22, 25, 52, 53, 56, 57, 60, 61, 89–91, 94, 96, 98, 134, 135

I-M injection-measurement vi, x, xi, 16, 18, 19, 26, 35–37, 41–49, 51, 52, 54, 57, 59, 61, 65, 67, 69–71, 77–79, 82, 84, 89, 98

ICU intensive care unit 8

IP inverse problem 16, 19, 37, 43

ML membrane lung 10, 12, 13

NF noise figure xi, xiii, 25, 53, 57, 60, 61, 89–91, 134, 135

NN neural network x–xiv, 26–31, 41, 42, 49–61, 79–85, 89, 92–95, 97–99, 124–126, 136, 137

$\mathbf{O_2}$ oxygen 7–9, 11, 13

OSLGN one-step linear Gauss-Newton 21

PE position error 22, 24, 53, 89, 90

PH primary hemostasis 5

PMP poly-methyl pentene 10, 11, 37

PSF point spread function 24

RBF radial basis function 56

ReLU rectified linear unit 27, 50, 55, 57, 58

RES resolution 24, 53, 90

RMSE root-mean-square error xi, xii, 80, 83, 92, 124, 125

RNG ringing 22, 25, 53, 89, 90

RWTH Aachen Rheinisch-Westfälische Technische Hochschule Aachen 61

SD shape deformation 22, 24, 53, 89, 90

SH secondary hemostasis 6

SNR signal-to-noise ratio 25, 54, 57, 59

SVD singular value decomposition 22, 46, 50, 51

SVM support vector machine 56

tanh hyperbolic tangent 27

VA venoatrial 8, 9, 13

VV venoventricular 8, 9

vWF von Willebrand factor 5, 13

Chapter 1

Introduction

Extracorporeal membrane oxygenation (ECMO) is a method which has been around for decades. While the procedure has helped many patients survive long enough to enable their treatment and aided the safer execution of heart surgeries, there are still many issues connected to it. Among these, the formation of blood clots inside the oxygenator itself is most common. Since the occurrence of thrombi in oxygenators can become detrimental to their function, early and reliable detection of these clots is needed. The detection methods used today are either not robust enough to detect all blood clots, have a significant detection lag time, or require the activity of already over-stretched medical staff.

The potential of impedance analysis for early blood clot detection in ECMO has been well documented in recent literature sources. The main goal of this thesis is, therefore, to exploit this potential and find the best approach for the detection and localization of thrombi in oxygenators. The optimization of this detection method is divided into four main tasks, which are addressed in this thesis according to the workflow depicted in Figure 1.1.

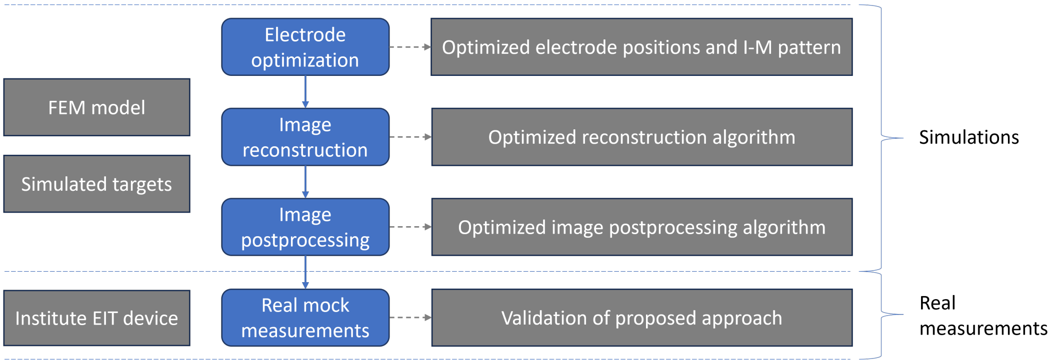

Figure 1.1: Simplified thesis workflow. Blue rectangles represent consecutive thesis goals and grey rectangles represent inputs and outputs.

- The first task is the optimization of electrode configurations and injection-measurement patterns. This optimization should result in more sensitive measurements capable of revealing thrombi locations mainly in regions with the highest probability of occurrence.
- The following task is to enhance image reconstructions and processing for optimal clot detection. Enhancements should lead to better image reconstruction resistant to measurement noise and without significant artifacts.

- The third task is the development of robust post-processing methods for thrombus identification and characterization. This will enable a quick assessment of the clotting severity in the oxygenator.
- The last step lies in the practical validation of the proposed approach on a mock oxygenator fabricated over the course of a previous thesis.

This thesis is divided into three main segments. Part one describes ECMO as a method, explains the issues of thrombus formation tied to it including the principles behind blood clotting. It also explains the principles behind electrical impedance tomography (EIT) and of methods used for the optimization of the used method. Part two is dedicated to the description of materials and methods (both experimental and statistical) used during modeling, optimization and measurements on the mock oxygenator. In part three, the results of the experiment are shown and discussed.

Part I

Theoretical background and literature research

In this section, I will give a brief introduction to the topics and principles tied to blood clot detection in extracorporeal membrane oxygenation (ECMO) oxygenators. I will start with a short introduction to blood and the hemostasis mechanism, focusing mainly on the mechanisms of clot formation. Subsequently, I will introduce the principles and applications of ECMO and issues that can arise during its use. The main problem discussed here will again be thrombus formation, this time inside oxygenators. In this section, the principles of thrombus detection based on electrical impedance tomography (EIT) will also be presented. The main focus of the final section of this theoretical introduction will be neural networks, which were often used in my implementation of the EIT algorithm.

Chapter 2

Blood

Blood is the body fluid with the greatest volume (ca. 5 – 6 liters in adults). It fulfills several functions crucial to our survival. Namely, it is responsible for transportation through the body, bringing oxygen and nutrients to cells and removing carbon dioxide and metabolic waste. It regulates our body temperature and prevents blood loss through clot formation. Additionally, it plays a vital role in the correct immune functions by transporting both antibodies and white blood cells. Blood comprises two main components - plasma and cells. Plasma is a watery solution containing proteins (e.g. hemoglobin or fibrinogen) and electrolytes (e.g. sodium or potassium) and forms roughly 55 % of the total blood volume. In addition to these (bio)chemical components, there are three basic cell types present in blood: erythrocytes (responsible for gas transport; ca. 5 million cells/µl), thrombocytes (responsible for primary hemostasis; ca. 300 thousand cells/µl) and leukocytes (responsible for immune responses; ca. 8 thousand cells/µl). The volumetric fraction of these cellular components in blood is called hematocrit and is usually around 45 %.

2.1 Hemostasis

One of the crucial functions of the cells and proteins contained in blood is hemostasis, the physiological reaction to vascular injury. It involves several steps which plug the damaged part of a vessel and so stop the bleeding. The first step of the hemostasis process is vasoconstriction, during which the vessel narrows, slows blood flow and increases shear rates. As a result of this fast response, the wound is closed by a plug made of activated thrombocytes in a process called primary hemostasis (PH). The increase of shear rate during PH activates thrombocytes in the blood stream via two distinct mechanisms. The cells can either be activated directly by shear rate changes or indirectly through bonds to the von Willebrand factor (vWF).

This factor is found in blood as a globular polymer, which exposes only few binding sites to its surroundings. However, under the changes in shear rate, the globular polymer is elongated to a linear one, which uncovers more binding sites. These binding sites can then attach both collagen exposed in the vessel defect area and thrombocytes.[1] Both these activation pathways lead to aggregates of thrombocytes at the site of injury.

After the thrombocytes initially cover the wound, a plasmatic reaction called secondary hemostasis (SH) begins. During this reaction, the protein fibrin is produced in order to reinforce the thrombus (a clot created by thrombocytes). Since large amounts of fibrin are needed, this reaction takes place via mediators (in this case thrombin), which can amplify fibrin formation over the course of three distinct stages. In the initial stage of SH (called initiation), tissue factor bearing cells are uncovered and a prothrombinase complex activated by the exposed tissue factor forms the initial amount of thrombin. The second stage, called amplification, is characterized by massive thrombin dissociation from tissue factor bearing cells. Throughout the last stage, called propagation, a thrombin burst occurs, which stimulates a massive thrombin conditioned fibrinogen to fibrin activation. In the end, a solid durable clot is formed from thrombocytes and fibrin.[2]

There are two basic types of thrombi based on the environment and conditions under which they are formed. White thrombi are formed in regions with high shear rates and are composed mainly of thrombocytes and fibrin. They are formed via the previously outlined mechanism. On the other hand, thrombi of a red color are formed in regions with lower shear rates and are composed mainly of erythrocytes and fibrin. While the latter are found mainly in veins, the former appear most often in arteries. It should be noted that there is a continuous spectrum of thrombus composition with the rule being that erythrocytes are increasingly likely to form a thrombus with decreasing shear rates.[3]

2.2 Hemostasis antagonists

Under normal circumstances, the pro-coagulation factors in the bloodstream (such as fibrin and thrombin) are in balance with anti-coagulation substances. When these factors are out of balance, blood may be less likely to coagulate in case of bleeding and cause massive blood loss or internal bleeding, or more likely to coagulate and create unwanted thrombi in the blood stream, which may then lead to thrombosis (the blocking of veins or arteries by blood clots). The development of thrombosis is governed by three main factors (Virchow's triad): hypercoagulability, stasis, and vessel damage. When at least 2 of the 3 factors occur concurrently, there's an increased risk of developing a thrombosis. Stasis is characterized by a turbulent or stagnating flow of blood. It occurs most commonly at vessel bifurcations or stenotic regions and is considered to be the most common thrombosis-inducing factor. In combination with either hypercoagulability or vessel damage, stenosis usually leads to clot formation. While hypercoagulability is caused by abnormalities in elements of the coagulation pathway, which leads to easier thrombus formation, vascular damage encompasses any abnormality resulting in the disruption of vascular endothelium (causes span from surgical intervention, to chemotherapy or sepsis).[4]

To keep the concentration of pro- and anti-coagulatory factor in balance, several physiological hemostasis antagonists, each with its unique anti-coagulation mechanism, are permanently released from a healthy endothelium (e.g. antithrombin III or the tissue factor pathway inhibitor) or based in healthy plasma (e.g. heparin, which amplifies antithrombin III).[5,6]

When the body's hemostasis system is out of balance, however, clinicians may prescribe or administer a myriad of anticoagulants to help counteract coagulation factors. This can prevent clotting-related issues such as myocardial infarctions, strokes or deep vein thrombosis. Among the most often clinically-used anticoagulants are:

- Heparin – injected subcutaneously or using an IV line, administration leads to an increase in its physiological concentration
- Coumarins – oral long-term medication, these molecules block vitamin K, which is necessary for the production of coagulation proteins in the liver
- New oral anticoagulants – oral medication, these pharmaceuticals affect specific coagulation factors and are therefore easy to monitor
- Citrate – infused into blood, this molecule binds free Ca^{2+} (coagulation factor IV)

Each of these anticoagulants has its advantages and disadvantages and should be administered by a clinician based on the patient's state and medical history. Additionally, we still lack a universal substance that would work well for all hemocoagulation-related issues.[7,8]

Chapter 3

Extracorporeal Membrane Oxygenation

Under normal circumstances, the heart drives blood through the body in order for it to fulfill its transportation function. The blood is also driven through lungs, where it is decarboxylized (carbon dioxide (CO_2) is removed) and oxygenated (oxygen (O_2) is bound to hemoglobin molecules). In cases of severe system failure, the function of the heart or lungs may be compromised and blood can no longer distribute O_2 to tissues and remove CO_2. When such problems arise, clinicians may use extracorporeal membrane oxygenation (ECMO). During this procedure, the function of the patient's heart, lungs, or both heart and lungs is temporarily substituted using an oxygenator in combination with a blood pump. The pump drives blood through the oxygenator, where blood is decarboxylized (the CO_2 is removed) and oxygenated (the O_2 is added) before being returned to the blood stream.[9]

3.1 A Brief History of ECMO

Oxygenators first came into use in the 50s in cardiopulmonary bypasses, which enabled the conducting of surgeries on stopped hearts. The earliest oxygenators were bubble-type, meaning that blood came into direct contact with bubbles of air of defined dimensions. However, the direct contact of blood with air often led to thrombus formation, cell damage due to prolonged contact, or the occurrence of air embolisms. The addition of a gas exchange membrane separating air from blood led to a radical improvement in these areas and allowed for longer and more efficient ECMO use. Such membrane oxygenators are used to this day. With the help of ECMO and anti-coagulation drugs (e.g. heparin), the survival time of patients on ECMO increased from several hours to several days in the 70s. Since then, two distinct forms of ECMO have been developed – venoatrial (VA) ECMO and venoventricular (VV) ECMO – where the latter provides only respiratory support and the heart must still pump oxygenated blood into the systemic circuit on its own, while the former fully compensates both the heart and lungs. Today, ECMO is mainly used in the intensive care unit (ICU) treatment of acute respiratory distress syndrome (ARDS) patients.

With the increasing use of ECMO devices in clinics all around the world came a need for their coordination and procedure standardization. This led to the foundation of the Extracorporeal Life Support Organization (ELSO) – a nonprofit consortium of institutions, researchers and industry partners working on ECMO and ECLS. To this day, there are more than 550 centers all around the world in the ELSO registry. Among other advantages, the formation of this organization allows for more comprehensive analysis of patients on ECMO and extracorporeal life support (ECLS). A report giving statistics on patients from 1990 to 2022 was published by ELSO in 2023. It shows that over the course of these years, 67 % of patients survived the procedure and 54 % of patients survived to discharge or transfer. It also documents a greater chance for a neonatal or pediatric patient to survive the procedure as opposed to an adult. Detailed statistics are depicted in Figure 3.1.[10–12]

3.2 The ECMO circuit

Figure 3.2 shows a simplified schematic of an ECMO circuit. From it, we can see the main components - the blood pump and the oxygenator. The circuit also includes cannulas, which secure the drainage of blood from the patient's bloodstream into the oxygenator as well as its return into the body. While it is possible to return the blood at the same site as it is drained (called single site cannulation), dual site cannulation (during which blood is drained and returned to the body in different locations) is still a more common procedure. In dual site cannulation the drainage cannula is usually inserted into the femoral vein for both VV and VA cases. Through the drainage cannula, deoxygenated (venous) blood is drained and flows through the blood pump to the oxygenator. Here, the blood is oxygenated and decarboxylated on a gas exchange membrane. The exchange rate is driven by partial pressure gradients and diffusion and is regulated by the O_2 concentration in the incoming air and air flow. Thanks to the integration of a heat exchanger, the circulating blood may also

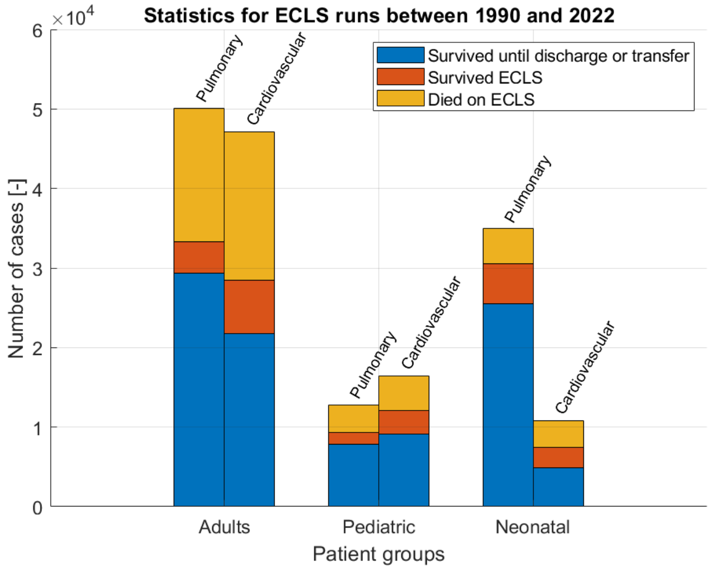

Figure 3.1: ECLS survival statistics between the years 1990 and 2022.

be cooled or warmed according to current medical needs. From the oxygenator, blood is returned back to the patient's body via a return cannula. This cannula is usually placed in the femoral artery for VA ECMO and in the internal jugular vein for VV ECMO. This way the body gets blood of an ideal O_2 content and temperature, which is then distributed to the organs.

3.2.1 Blood pumps for ECMO

There are two main pump technologies used in ECMO devices. The first option is a roller pump, in which blood is pushed through a soft tube in a peristalsis-like manner. A pump roller first squeezes the tube behind the volume of blood to be transported to prevent back-flow and then pushes the blood forward though the tube. The second option is a centrifugal pump, in which an impeller rotates to drive blood through the system. Both these pumps have their advantages and disadvantages. While roller pumps require an additional blood reservoir, as the actual drainage of blood is gravity-driven, centrifugal pumps have no spacial limitations, as the initial priming with blood is enough for the pump to continue pumping. Apart from spatial constraints, the safety of these pumps is also a big concern. A study conducted by Halaweish et al. in 2015[13] revealed that despite lower doses of heparin (an anti-coagulant) administered with centrifugal pumps, there was a higher incidence of bleeding as opposed to roller pumps. Another study, conducted by Papadimas et al. in 2021,[14] showed that roller pumps are associated with a lower incidence of hemolysis, cardiac complications, renal complications and death in children. However, newly developed centrifugal pumps with low priming volumes and minimal blood trauma could enable the development of much smaller and cheaper ECMO devices for children.[15] Nowadays, the overall trend is to replace roller pumps with centrifugal pumps. This transition was documented to lead to better results in terms of hemolysis

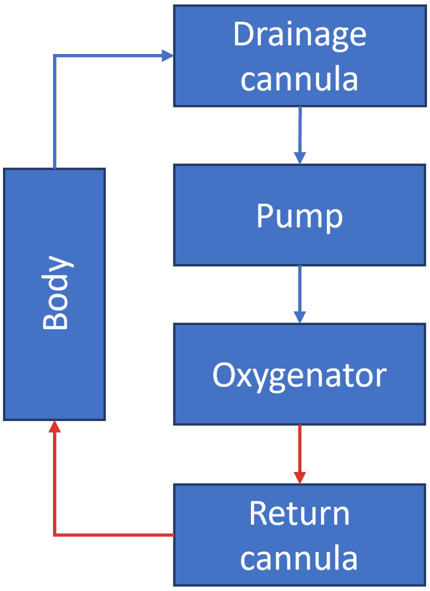

Figure 3.2: A simplified schematic of an ECMO circuit based on [9]. Blue arrows represent deoxygenated and carboxylized blood while red arrows represent oxygenated and decarboxylized blood.

occurrence in some cases (e.g. [16]), but other studies couldn't prove these beneficial outcomes (e.g. [17]).

3.2.2 Membrane Oxygenators

Modern oxygenators are exclusively membrane gas exchangers and often carry the name "membrane lung" (ML). The main goal of oxygenators is to facilitate oxygen and carbon dioxide exchange. There are three important oxygenator components that ensure this objective is achieved as harmlessly as possible for the patient.

- Oxygenator body
- Membrane
- Heat exchanger

The body of the ML comprises a cuboidal or cylindrical volume through which the patient's drained blood flows. There are different flow patterns present in the oxygenator depending on the shape of the body. Several inlets and outlets are incorporated for gas and fluid flow.[11] Inside the oxygenator body, gas exchange takes place on a membrane with a surface area that can reach several m^2, which consists of hollow fibers usually made from either silicone, microporous polypropylene, or poly-methyl pentene (PMP).

Original silicone hollow fibers were of a bigger diameter (ca. 800 µm) and wall thickness (ca. 200 µm) then they are today. They had poor gas permeability but were free of plasma leakage, a dangerous phenomenon when the blood plasma leaks into the gas compartment and may result in the formation of condensation on the gas side or the presence of very high driving pressures. On the other hand, microporous polypropylene fibers have better gas transfer capabilities but once the micropores lose their hydrophobic character, plasma leakage becomes a big issue. In PMP fibers, gas exchange takes place through a plasma tight polymer matrix with hydrophobic properties. This enhances the separation of the blood and gases and prevents plasma leakage. PMP oxygenators also have a low priming volume (the volume of blood needed in the system for the pump to begin functioning) and a reduced pressure drop (the difference in pressures upstream and downstream of the oxygenator), which makes them most used today.[18–20] However, novel fine silicone materials with sufficient mechanical strength are being developed (e.g. in Japan[21,22]). These new fibers can support a wall thickness of 50 µm and a diameter of 300 µm under sufficient gas transfer performance for long-term ECMO support and are therefore a promising candidate for future use.

Apart from membranes for gas exchange, oxygenators may also encompass heat exchangers, which are responsible for adjustments of the patient's blood temperature. They are usually made from polyurethane, polyester or stainless steel and their surface area varies approximately from 0.1 to 0.7 m^2. With a temperature gradient present between water in the heat exchanger and the patient's blood, a thermal bridge is created and temperature adjustments to blood are possible. There is a reasonable belief that inducing hypothermia (lower temperature) may help minimize several pathological pathways that pose a thread to ECMO patients. However, clinical proof for this claim is still low.[11,23]

There are currently many companies on the market offering different oxygenators, some of them with advanced sensors measuring oxygen saturation, hematocrit or blood temperature (e.g. Maquet Cardiopulmonary GmbH, Rastatt, Germany).[11,24]

Today, one of the crucial hurdles that needs to be overcome in regards to oxygenator safety is the fact that the oxygenator poses the largest blood-ECMO contact area. This may lead to complications for patients on ECMO. The correct choice of oxygenator is therefore crucial.[9,11] There are several important parameters that are evaluated when comparing different oxygenators and their influence on patients including:

- Priming volume (when it is low enough, little donor blood may be needed to prepare the oxygenator),
- Membrane gas permeability for O_2 and CO_2 (good permeability enables the ideal oxygenation and decarboxylation of blood),
- Plasma leakage (plasma may leak through micropores in membrane fibres into the gas compartment, decreasing the efficiency of gas exchange),
- Pressure drop (a bigger pressure drop indicates more resistance of the oxygenator to blood flow),
- Shear stress and flow characteristics (these influence hemolysis and thrombogenicity inside the oxygenator),
- Biocompatibility of materials (this lessens the toxicity and thrombogenicity of the oxygenator).

Of the parameters influencing oxygenator safety, biocompatibility stands out as the one most easily adapted over multiple oxygenator types. When blood comes into contact with a foreign surface, the human body reacts almost instantly. Within milliseconds coagulation and inflammatory systems are activated and the process of rejecting the foreign material begins. This process poses a big problem for all medical devices interacting with human blood. Therefore, a systemic anti-coagulation together with the utilization of biocompatible materials and coatings is necessary, particularly for long-term ECMO applications. Biocompatible coatings are based on antithrombotic biomolecules such as heparin, polymers or glycoproteins. The most frequently used coatings in ECMO devices are based on heparin (e.g. the Carmeda coating).[11]

3.3 Thrombus formation in the ECMO circuit

As seen in the previous section, there are many parameters influencing thrombus formation. A thrombotic clot within the ML is a serious and quite common problem which occurs during ECMO treatment. Acute thrombosis of the oxygenator or blood pump happens in 35 % of the cases. Unfortunately, the details of the ML thrombus formation are still not precisely understood. It is however documented that fibrous or cellular deposits residing on the membrane fibers can lead to:

- an increase in blood flow resistance and risk of hemolysis,
- a reduction of oxygenation and decarboxylation capabilities,
- further activation of coagulation processes, and
- an induction of thromboembolic complications if dislodged.

Clotting necessitates an imminent exchange of the ML, which is a dangerous procedure for patients in critical conditions.

When blood comes into contact with the foreign ECMO surface, a layer of plasma proteins (mainly fibrinogen) is created on the surface. This triggers thrombocyte adhesion to the fibrinogen receptors and also starts the coagulation cascade, which results in thrombin production. This reaction is slowed by biocompatible surfaces and coatings but hemocompatibility is still limited. Therefore, proper clot monitoring in the ECMO circuit is necessary, mainly in areas with turbulent or stagnant flow (e.g. tubing, fittings or cannulas). Flow plays an important role in cell movement and thrombus formation. While increased shear rates activate thrombocytes, in low shear rate conditions, erythrocytes, leukocytes and thrombocytes can from stable aggregates. Therefore, a solution is not as simple as just decreasing the shear rates inside the oxygenator, as the fluctuation of shear rates in either direction may cause clots to form.

In a study conducted by Conway et al. in 2020,[25] the clot burden from explanted oxygenators was compared to a computational fluid dynamics simulation of clot formation. The largest clot burden was found in the corners, likely caused by an insufficient regional wash combined with a lower volume to surface area ratio that enables clots to adhere well. Several studies have already reported on thrombus composition, which might lead to a better understanding of underlying drivers for clotting mechanism. A study conducted in 2022 by Staessens et al.[26] focused on VA-ECMO thrombi. They found out that these thrombi were mainly heterogenous with fibrin and vWF being the main components. Based on composition differences, two distinct thrombus types were identified. The first type was rich in erythrocytes and poor in fibrin and the second type was poor in erythrocytes and rich in fibrin. Interestingly, the location of these thrombi within the device wasn't type-specific.

Another study conducted by Hastings et al. in 2017[27] focused on analysing clots from pediatric ECMO patients and the relation between their location and hemodynamic simulations. They came to a statistically significant conclusion that most clots were adherent to the junctions made by the tubing and connectors rather than randomly disturbed throughout the circuit tubing. Nonadherent coiled clots with a length of more than 5 cm were also found in the upstream part of the oxygenator. The comparison to hemodynamic simulations revealed that clots coincided directly with low shear rate zones. The conducted histology revealed a thrombus composition consistent with coagulation caused by low shear rates (clots were rich in fibrin and erythrocytes with minimal thrombocytes presence). The study also showed a higher occurrence of clots in centrifugal pumps as opposed to roller pumps.[11,28–30]

3.4 Thrombus detection in the ECMO circuit

Various parameters are being monitored in clinics in order to detect clots during ECMO treatment. Three main methods exist for clot detection, each with its own benefits and drawbacks. The simplest check performed regularly is a visual inspection of the externally visible parts of the oxygenator and tubing. However, this method will not reveal thrombi hidden within the oxygenator. Research was conducted on the relationship between externally visible clots and internal clots, but no significant correlation was found. Additionally, visual thrombus detection also requires manual inspection by a nurse or clinician, thus adding to the workload of medical personnel.

The second method of clot detection in ECMO is based on the measurement of partial O_2 and CO_2 pressures in the oxygenator outlet, which are directly influenced by thrombus formation on the membrane surface. Gas transfer capabilities are limited by the presence of the thrombus and oxygenation and decarboxylation efficiency is decreased. This method is only targeted at thrombi localized on the membrane surface, however.

The most commonly-used method measures pressure drops on the oxygenator. One pressure sensor is placed upstream and a second sensor downstream of the ML, with the difference between the pressure at these two senors being called the pressure drop. Accumulated thrombi cause an increase in flow resistance, which translates into an increased pressure drop. When the pressure drop increases too much, the oxygenator needs an acute exchange. There is a direct relationship between the pressure drop and the clot volume and progression, but it is not possible to make a reliable analysis based just on this parameter.[31,32]

In order to circumvent sudden ECMO problems related to thrombi formation resulting in an imminent need for oxygenator exchange, an automatic and reliable method for early blood clot detection would be extremely beneficial.

3.5 Detection of blood clots based on bioimpedance

One such a method could be distinguishing blood from blood clots based on their bioimpedance.[33] The difference in bioimpedance between blood and thrombi has been shown in a study conducted by Noshiro et al. in 2007.[34] In a frequency range from 100 kHz to 800 kHz, the authors observed a conductivity difference around 4 mS.cm^{-1} = 0.4 S.m^{-1} between normal and coagulated blood. This difference decreases with increasing frequencies over 800 kHz. According to a study conducted by Gelfan and Quigley in 1930,[35] thrombus impedance starts to rise sharply ca. ten minutes after the start of coagulation. Although this principle of blood clot detection has been utilised by several researchers, there are some factors complicating its use. Blood impedance is dependent not only on the blood coagulation state, but also on the hematocrit value, flow, erythrocyte orientation or temperature. The impedance of the blood clot alone is also influenced by clot composition adding in more variables to consider for method development.

In a study conducted in 2021 by Chen et al.,[36] a portable EIT device was developed for thrombus detection under stationary and dynamic (moving thrombus) conditions. The device used 8 electrodes and an iterative reconstruction algorithm. Authors were able to reliably detect thrombi 3 mm and 5 mm in size with good positional precision in both cases. Another study conducted by Türkmen et al. in 2023[31] demonstrated that bioimpedance analysis can reliably indicate clot formation inside a blood-perfused test chamber. A special impedance-measuring device was used (AFE4300, Texas Instruments Inc., Dallas, TX, USA) for the bioimpedance measurements. A direct correlation between bioimpedance increase and clot formation was observed. No change in bioimpedance also implicated no clotting activity. Authors also monitored pressure drop over the test chamber and compared clot detection and prediction abilities of these two approaches. A significantly earlier response was observed in the increase of bioimpedance than in pressure drop, with the time difference between these two methods being 8 minutes. Pressure drop monitoring acted as a detector only if extensive clotting occurred and the flow path was dramatically constricted, whereas bioimpedance changed even when only marginal blood cell residues were present in the test chamber.

In a different study conducted in 2015 by Sapkota et al.,[37] electrical resistance tomography was applied to thrombus visualization in blood, both under static and dynamic (moving thrombus) conditions. Thrombi of sizes larger than 3 mm were detected under static conditions. Smaller thrombi didn't cause a significant increase in measured resistivity. Authors suggest that higher resistivity is caused mainly by the local hematocrit value and orientation of erythrocytes. Under dynamic conditions, the authors observed that variation of blood flow from 0.55 l.min^{-1} to 2.68 l.min^{-1} caused a higher relative resistivity change than a thrombus. However, thrombi bigger than 3 mm in diameter were successfully detected in both static and dynamic conditions.

The mentioned studies prove that thrombus detection based on impedance change is feasible and has a great potential to enhance the current state of thrombus detection in ECMO circuits. EIT could bring automated and reliable early thrombus detection to clinics and thus make this method safer for patients and relieve the workload for medical personnel.[38]

Chapter 4

Electrical impedance tomography

The detection or mapping of the electrical properties of objects (such as the bioimpedance of blood and thrombi) is called electrical impedance tomography (EIT). More specifically, EIT allows for the depiction of inner conductivity distributions based on impedance measurements at surface electrodes. EIT devices are small, quick to set-up, non-invasive, relatively cheap and radiation-free, which gives them superiority over computed tomography (CT) or magnetic resonance imaging (MRI). The resulting images have a relatively low spatial resolution, but a high temporal resolution (few tens of ms). During EIT, high-frequency (above 50 kHz) low-amplitude (less than 5 mA) electrical currents are injected through pairs of electrodes. The resulting electric potentials are measured on the surface (again between pairs of electrodes) and reconstruction algorithms are then used to compute conductivity distribution. This problem is ill-posed and nonlinear.[39]

Bedside monitoring is the main use-case for EIT nowadays. Doctors are able to monitor pulmonary and heart activity virtually in real time and make necessary adjustments (for example to ventilator parameters) to better suit the patient's needs and avoid a ventilator-induced lung injury. The most common way to perform EIT is through a belt with incorporated electrodes (typically 16) placed on the patient's thorax. In this case, reconstructed conductivity values lie in a 2D plane specified by the belt electrodes.[40–43]

4.1 Bioimpedance measurements

When used for measurements on living organisms, the property measured using EIT is bioimpedance. This is a physical quantity that reveals how much the respective tissue opposes the flowing current, which, in the case of organisms, takes the form of moving ions. Different tissues modify the current differently; some have a mostly resistive character and some have a significantly capacitive behaviour. The differences between these characters allow us to map the inside of the studied space. In our case, we will look more closely at blood as a target of bioimpedance measurements. Blood is one of the best conductors inside the body with constituent cells effectively behaving as capacitors. Its resistivity is largely dependent on current frequency as a low-frequency current can't enter the cells and travels around them and a high-frequency current penetrates them. Based on these properties, a cellular impedance model can be constructed as an electronic circuit with two resistors and one capacitor as seen in Figure 4.1.

Impedance is a complex quantity, which is usually denoted as Z and is defined by

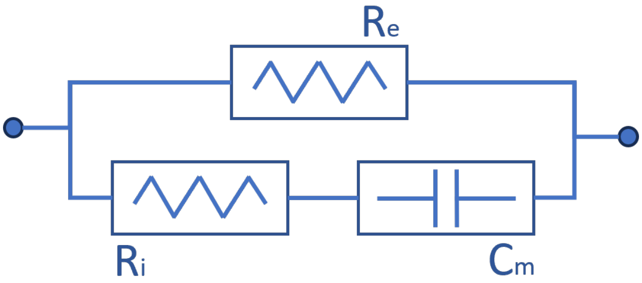

Figure 4.1: A cellular impedance model based on [42]. R_i represents intracellular resistance, R_e represent extracellular resistance and C_m represents membrane capacitance of cells.

Equation (4.1)

$$Z = R + j.X \tag{4.1}$$

where R represents resistance (the real part) and X represents reactance (the complex part connected to the capacitive behaviour). Impedance can be computed using Ohm's law according to Equation (4.2)

$$Z = \frac{V}{I} \tag{4.2}$$

where V represents voltage and I represents current.

EIT devices inject a known current into the patient and measure voltage, which allows for the computation of impedance from Ohm's law. Electrodes are usually able to measure both the voltage amplitude and phase shift, but most image reconstruction algorithms use only the amplitude. Thus, it is common to use only the real part of the computed impedance, which is inverted into conductivity according to Equation (4.3).

$$\sigma = \frac{1}{\Re\{Z\}} \tag{4.3}$$

Based on measured and computed values, an inner conductivity map can be created. EIT contains two mathematical problems which map the inner conductivity distribution to surface potentials at the electrodes (the forward problem (FP)) and vice versa (the inverse problem (IP)) based on used injection-measurement (I-M) patterns. The solution of the FP is the used to learn how to map the conductivity distribution in the IP. Thus, both problems need to be solved for the development of EIT-based methods.

4.2 Forward problem

The forward problem (FP) calculates potentials on the boundary using an estimation of model of the conductivity distribution and can be expressed as (4.4)

$$\boldsymbol{v} = F(\boldsymbol{\sigma}, \boldsymbol{q}) \tag{4.4}$$

where $\boldsymbol{v}$ represents the vector of measured voltages at surface electrodes, $\boldsymbol{\sigma}$ represents the matrix of conductivity distribution and $\boldsymbol{q}$ represents the vector of the current injection pattern.

The most common model developed to solve the FP is called the complete electrode model (CEM), which incorporates skin-electrode impedance. It is based on Maxwell equations and boundary conditions. Time and spatial discretization is used to solve the partial differential equations resulting from this model, as the analytical solution is too complex to compute.[44,45]

4.2.1 The finite element method

The prevailing approach to the numeric solution of the FP is the finite element method (FEM). Complex problems defined in geometrical domains are reduced to finding a solution in a finite number of points (nodes), which divide the domain into smaller regions (finite elements). Simplices (triangles for 2D space and tetrahedra for 3D space) created by triangulation are commonly used as these finite elements. A continuous function of the unknown field variable of interest (in our case electrical voltage or current) is approximated from solutions at the given nodes using piece-wise linear functions in each finite element. The finite elements in the mesh are tied together via a set of linear algebraic simultaneous equations.

The number of finite elements and their size determine the solution resolution. For the purposes of EIT, it is better to choose smaller elements (a denser mesh) around the electrodes and bigger elements (a sparser mesh) elsewhere to save computation power and keep accuracy. Meshes for forward and inverse problems are often different with the inverse mesh being coarser. This is done to prevent so called inverse crime.[46]

4.2.2 Sensitivity matrices

Based on the FP, we can compute a sensitivity matrix (also called a Jacobian matrix or a Jacobian). This gives us a way to investigate how sensitive each voltage measurement is to small conductivity changes in the FEM mesh and therefore how well our EIT method reacts to these changes. This matrix is defined by Equation (4.5)

$$\boldsymbol{J}_{i,j} = \frac{\partial \boldsymbol{v}_i}{\partial \boldsymbol{\sigma}_j} \tag{4.5}$$

where $\boldsymbol{J} \in \mathbb{R}^{n_V \times n_M}$ is a sensitivity matrix with dimensions given by the number of voltage measurements (n_V) and the number of finite elements (n_M), $\boldsymbol{J}_{i,j}$ represents position i,j in the sensitivity matrix, $\boldsymbol{v}_i$ represents the i-th voltage measurement, and $\boldsymbol{\sigma}_j$ represents the j-th finite element. All of the measurements of one frame are squeezed into one column and all of the finite elements are squeezed into one row. This way all of the sensitivity information is contained just in a single matrix.

Regions well covered by each voltage measurement are easily identifiable based on the sensitivity matrix. This way, the FP can help us tune measurement parameters such as electrode positions. These can be adjusted based on the information from sensitivity matrix in order to enhance the sensitivity in specific regions of interest.[44]

4.3 Injection and measurement patterns

In addition to electrode positions, injection-measurement (I-M) patterns may be tuned for better imaging. These patterns tell us which electrodes will inject a signal into the measured volume and which will measure it. A four-terminal method (also called the bipolar method) is the prevailing I-M system for EIT. Four electrodes are simultaneously used during these measurements - two electrodes (the injecting pair) deliver an AC current and two different electrodes (the measuring pair) measure the resulting voltage.[33] With 16 electrodes being the most common for EIT devices, it is possible to measure at 13 other electrode pairs for one injecting pair. There are 16 possible shifts of the injection pair which results in a total of $16 \times 13 = 208$ voltage measurements. Because of the reciprocity principal, which states that a swap of injecting and measuring pair yields the same conductivity data, there are only 104 independent measurements available. This corresponds to a general Equation (4.6) giving the number of independent measurements from N electrodes for the bipolar method published by Brown in 2003:[47]

$$N_{im} = \frac{N \times (N-3)}{2} \tag{4.6}$$

where N_{im} represents the number of independent voltage measurements.

Such a bipolar method eliminates the influence of skin-electrode impedance on the measurement because skin-electrode impedance is negligible compared to the input impedance of the measuring electrode pair. In order to speed up data acquisition, it is also possible to concurrently measure voltages at all other available electrode pairs. The chosen data acquisition pattern influences which parts of the studied volume will be most sensitively scanned and also the quality of the final reconstruction.[48]

4.3.1 Adjacent pattern

The most commonly used I-M pattern is the adjacent-adjacent pattern. Adjacent electrodes are used as both injection and measurement pairs. While the adjacent-adjacent pattern has by far the greatest sensitivity around the electrodes, it has problems with objects in the middle of the measured volume. From a distinguishability measure developed by Adler et al. in 2011[49] (based on the signal-to-noise ratio and the probability of conductivity change detection in regions of interest), the adjacent-adjacent I-M pattern turned out to have to poorest performance out of all examined patterns. Based on their findings they encourage clinics to start using other I-M patterns (for example trigonometric patterns or pair I-M patterns separated over 90 degrees).

4.3.2 General injection-measurement patterns for the bipolar method

A sequence (also called frame) of measurements of a bipolar configuration is finished when all injecting and measuring pairs have systematically rotated around the diameter and switched all possible positions. Any arbitrary I-M pattern may be described by an I-M number combination. Both I and M give the number of positions between the electrodes (offset), which is fixed during rotation. Adjacent electrodes have an offset of 1 position, so the adjacent-adjacent pattern covered in previous section can be labeled as a 1-1 pattern. On the other hand, the opposite pattern, which utilizes electrodes directly opposing each other for both injection and measurement, can be labeled as an 8-8 pattern.

In a study conducted in 2022 by Smela,[48] all 36 independent I-M combinations for 16 electrodes were analyzed. Most of the configurations with less than 104 independent measurements had a bad spatial resolution and performed poorly. It was observed that adjacent-adjacent and opposite-opposite patterns performed significantly worse than patterns 3-3 or 7-7. Both of these patterns are reasonably sensitive both in the center and near the edge.

4.4 Time-difference EIT

There are different EIT modalities based on the goal of the reconstruction. The most common approach in the medical field is difference EIT, which compares a set of two measurements. Time-difference EIT uses two sets of voltage measurements recorded at different points in time to reconstruct changes in conductivities. Usually, the first measurement is called a reference or homogeneous measurement and doesn't contain any targets or abnormal anatomical features. This measurement is commonly averaged to improve stability and lower the effect of random noise. The second measurement, on the other hand, contains inhomogenities that we want to see as significant in the reconstructed difference image. The difference voltage is often normalized to the reference voltage according to Equation (4.7).

$$\Delta \boldsymbol{v} = \frac{\boldsymbol{v}_{inhom} - \boldsymbol{v}_{ref}}{\boldsymbol{v}_{ref}} \tag{4.7}$$

where $\Delta \boldsymbol{v}$ represents a vector of normalized difference voltages, $\boldsymbol{v}_{ref}$ represents a vector of reference homogenous voltage measurements and $\boldsymbol{v}_{inhom}$ represents a vector of inhomogenous voltage measurements. The main factor contributing to the broad use of difference EIT is the fact that it compensates time-invariant errors caused by noise, the device setup, and electrode or domain shape inaccuracies. The only drawback is that information about absolute conductivity is lost.

Another approach, mostly used in geological sciences, is absolute EIT. It is more technically challenging, because systemic errors will stay in the measurements. Therefore, much stricter requirements on parameters of the EIT device itself apply. System accuracy is highly dependent on channel-to-channel variations and errors must be mitigated as much as possible.[39, 42, 50]

4.5 Inverse problem

The inverse problem (IP), which is also called reconstruction, lies in the reconstructing of the conductivity distribution from voltage measurements and can be formalized using Equation (4.8)

$$\boldsymbol{\sigma} = F^{-1}(\boldsymbol{v}, \boldsymbol{q}) \tag{4.8}$$

where $\boldsymbol{\sigma}$ represents a matrix of the conductivity distribution, $\boldsymbol{v}$ represents a vector of measured voltages at surface electrodes, and $\boldsymbol{q}$ represents a vector of the current injection pattern.

In the reconstruction algorithms of methods such as computed tomography (CT), it is possible to assume that beams pass through the object in a straight trajectory and their attenuation is caused only by the elements along their path. This imaging method property is called local and unfortunately doesn't apply in EIT. In the case of EIT, scattering is present a lot more and almost every voxel in the image is projected into all measured signals. As a result it is necessary to solve a system of simultaneous equations relating every voxel to every measurement in order to find the reconstructed image.

Another unpleasant property of EIT is its non-linearity. This causes large conductivity changes to produce much smaller voltage differences. Additionally, measured voltages will saturate for large conductivity contrasts. Superposition also doesn't apply to EIT. A measurement of two spatially close regions doesn't yield the same result as combination of these two separate measurements. However, the biggest problem for EIT is the severe ill-posedness of the reconstruction problem. In the best case 104 independent measurements are available for one frame for a typical reconstruction grid of $32 \times 32 = 1024$ pixels for the 2D case. For this reason regularization techniques are applied to tackle the under-determined problem. Let us now focus on reconstruction algorithms for time-difference EIT.[42]

4.5.1 Backprojection

The first reconstruction algorithms were developed on the basis of filtered backprojection used in CT reconstruction. Their principle lies in the superposition of high-pass filtered projections over the reconstructed image. In the case of EIT, backprojection can be performed along equipotential lines. The historically most-used algorithm called Sheffield Backprojection differs slightly from this principle by using regularization. It performed reasonably well on experimental data, was quick and not overly demanding resource-wise. However, compared to state-of-the-art algorithms, it lacks quality and reconstructed images regularly contain radial artifacts.[42,51]

4.5.2 Linear reconstruction algorithms

A second family of reconstruction algorithms simplifies the EIT forward problem by assuming that measured voltages are linearly dependent on the conductivity changes through the Jacobian. This means a linear approximation of the FP around initial conductivity distribution $\boldsymbol{\sigma}_0$ can be expressed by Equation (4.9):

$$F(\boldsymbol{\sigma}, \boldsymbol{q}) \approx F(\boldsymbol{\sigma}_0, \boldsymbol{q}) + \boldsymbol{J}\Delta\boldsymbol{\sigma} \tag{4.9}$$

where $\boldsymbol{J}$ represents the Jacobian and other parameters are the same as in the general formulation of the FP in Section 4.2. Therefore, Equation (4.10) applies to time-difference imaging as follows:

$$\Delta \boldsymbol{v} = \boldsymbol{J}\Delta\boldsymbol{\sigma} + \boldsymbol{n} \tag{4.10}$$

where $\Delta\boldsymbol{v}$ represents the vector of measured difference voltages, $\boldsymbol{J}$ represents the Jacobian, $\Delta\boldsymbol{\sigma} \in \mathbb{R}^{n_M \times 1}$ represents the flattened matrix with conductivity changes, and $\boldsymbol{n}$ represents ideal uncorrelated white Gaussian noise.

The general goal of these linear algorithms is to perform an approximation of Jacobian inversion and compute a reconstruction matrix $\boldsymbol{R} \in \mathbb{R}^{n_M \times n_V}$ to perform reconstruction based on Equation (4.11).

$$\hat{\boldsymbol{\sigma}} = \boldsymbol{R}\Delta\boldsymbol{v} \tag{4.11}$$

One-step linear Gauss-Newton

One of the approaches to Jacobian inversion by utilizing linear approximation is the one-step linear Gauss-Newton (OSLGN) method. As the name suggests, it calculates the reconstructed image in just one iteration. The reconstructed conductivity distribution $\hat{\boldsymbol{\sigma}}$ is calculated so that it is faithful to both the measured voltages and "reasonable assumptions" while utilising Tikhonov regularization. The solution is derived from Equation (4.12):

$$\min \|\Delta\boldsymbol{v} - \boldsymbol{J}\hat{\boldsymbol{\sigma}}\|^2_{\Sigma_n^{-1}} + \|\hat{\boldsymbol{\sigma}}\|^2_{\Sigma_\sigma^{-1}} \tag{4.12}$$

where $\Sigma_n^{-1} \in \mathbb{R}^{n_V \times n_V}$ represents the diagonal covariance matrix of measurement noise $\boldsymbol{n}$ with single elements $\Sigma^{-1}_{n[i;i]} = \sigma_i^2$, σ_i^2 represents the noise variance of voltage measurement i, and $\Sigma_\sigma^{-1} \in \mathbb{R}^{n_M \times n_M}$ represents the expected image covariance. Both covariance matrices are usually modelled heuristically based on prior considerations. Two more matrices are define to simplify the final equation. Matrix V (given by Equation (4.13)) models measurement accuracy and matrix P (given by Equation (4.14)) is a regularization matrix which models the prior likelihood of image elements and their interactions.

$$\boldsymbol{V} = \sigma_n^2 \boldsymbol{\Sigma}_n \tag{4.13}$$

σ_n^2 represents the average measurement noise amplitude. Matrix V is equal to the identity matrix for identical measurement channels ($\boldsymbol{V} = \boldsymbol{I}$).

$$\boldsymbol{P} = \sigma_\sigma^2 \boldsymbol{\Sigma}_\sigma \tag{4.14}$$

σ_σ^2 represents the amplitude of the expected conductivity change.

Solving Equation (4.12) yields solution (4.15):

$$\hat{\boldsymbol{\sigma}} = \boldsymbol{R}\Delta\boldsymbol{v} = (\boldsymbol{J}^T\boldsymbol{V}^{-1}\boldsymbol{J} + \lambda^2\boldsymbol{P}^{-1})^{-1}\boldsymbol{J}^T\boldsymbol{V}^{-1}\Delta\boldsymbol{v} \tag{4.15}$$

where $\lambda = \frac{\sigma_n}{\sigma_\sigma}$ is a regularization hyperparameter which controls the $\frac{\text{resolution}}{\text{noise attenuation}}$ tradeoff. The solution from Equation (4.15) can be simplified as Equation (4.16) if $\boldsymbol{V} = \boldsymbol{I}$.

$$\hat{\boldsymbol{\sigma}} = \boldsymbol{R}\Delta\boldsymbol{v} = (\boldsymbol{J}^T\boldsymbol{J} + \lambda^2\boldsymbol{P}^{-1})^{-1}\boldsymbol{J}^T\Delta\boldsymbol{v} \tag{4.16}$$

Image elements can be assumed independent with identical variance for a simplified reconstruction, which leads to $\boldsymbol{P} = \boldsymbol{I}$ and 0-th order Tikhonov regularization. This reconstruction tends to push reconstructed noise towards boundaries and make the reconstruction more sensitive to objects placed at these boundaries. Other priors can be utilized as well, such as NOSER ($\boldsymbol{P}$ is scaled by the sensitivities of each element) or a Laplacian filter. Other regularization approaches are also possible; Tikhonov regularization can be replaced by truncated singular value decomposition (SVD) or iterative reconstruction techniques.[52]

GREIT

A consensual reconstruction algorithm called Graz consensus Reconstruction algorithm for EIT (GREIT) was assembled during an EIT conference in 2009 in Graz by Adler et al.[52] It is now the most frequently used reconstruction algorithm. It depends on the forward model, noise model and desired performance metrics and results in reconstructed images on a grid of 32 × 32 pixels. The forward model is based on a CEM, utilizes an FEM mesh and also contains information about electrode size and contact impedance.

The first type of noise considered in the noise model is electronic measurement noise. It is considered uniform and Gaussian, although some calibrated EIT measurements show non-Gaussian and inter-channel-varying behavior. Authors therefore recommend using a pre-measurement calibration protocol and an integrating model of the specific hardware into the forward model. The second type of noise considered is caused by electrode movement artefacts. They usually originate in posture change or breathing. It is possible to mitigate the influence of movements by augmenting the forward model based on conductivity change and electrode movement.

A training set of "desired images" ($\tilde{\boldsymbol{\sigma}}_t{}^{(k)}$) is created based on figures of merit (FoM). At first, small "point" conductivity changes called targets are created ($\boldsymbol{\sigma}_t^{(k)}$). They are randomly and uniformly spread throughout the medium with a diameter smaller than 5 percent of the medium size. This means they are smaller than the inherent EIT resolution. The desired image corresponding to the conductivity target has the same center, but also a defined circular area which accounts for blurring. This allows GREIT to achieve a more uniform resolution throughout the whole domain.

For each desired image for training $\tilde{\boldsymbol{\sigma}}_t{}^{(k)}$, image weighing $\boldsymbol{w}^{(k)}$ may be defined, which allows for the tuning of the relative importance of FoM in all pixels of the image. There is an inner circular zone around the target center where the reconstructed image amplitude should reach maximum and be flat to satisfy the amplitude response (AR) and position error (PE) performance metrics. Then there is an outer circle which marks the boundary of where the reconstructed image should be zero to satisfy the ringing (RNG) and shape deformation (SD) performance metrics. In these two regions the corresponding weights $\boldsymbol{w}^{(k)}$ are large to provide a penalty for images reconstructed outside of the specified region. Between these two circles there is a transition zone where the reconstructed amplitude should gradually decrease down to zero. In this zone small values of $\boldsymbol{w}^{(k)}$ allow for flexible adjustments of other specifications. The structure of a desired image is depicted in Figure 4.2.

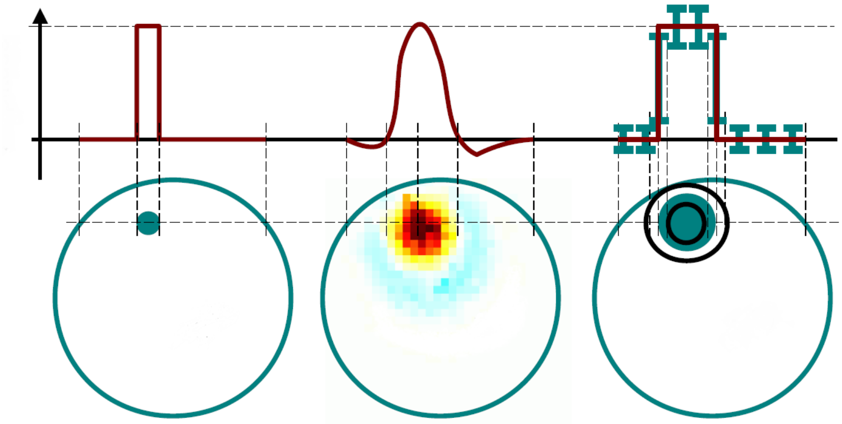

Figure 4.2: The upper row contains image amplitudes on the dashed line crossing the target center while the lower row contains the images alone. Left: $\boldsymbol{\sigma}_t^{(k)}$ - A simulated target with the same maximum amplitude in the whole target region. Center: $\hat{\boldsymbol{\sigma}_t}^{(k)}$ - A reconstructed image with visible artefacts of deformed circular shape and significant ringing. Right: $\tilde{\boldsymbol{\sigma}_t}^{(k)}$ - A desired image with highlighted inner and outer circles forming three important zones with different desired amplitudes, weights $\boldsymbol{w}^{(k)}$ are symbolized by error bar lengths. This figure was adapted from [52].

Another training group is based only on noise and artefacts. Random noisy images are generated with corresponding desired images of zeros. Training on noise should make reconstruction less prone to amplifying noise.

Iterative evaluation over the whole training set based on FoM leads to the final reconstruction matrix $\boldsymbol{R}$. The optimization criterion is determined by Equation (4.17) and the whole minimization process results in a generalized Tikhonov regularization.

$$\epsilon^2 = \sum_k \|\tilde{\boldsymbol{\sigma}_t}^{(k)} - \boldsymbol{R}\Delta\boldsymbol{v}^{(k)}\|^2_{\boldsymbol{w}^{(k)}} \tag{4.17}$$

For a single training target k: $\tilde{\boldsymbol{\sigma}_t}^{(k)}$ represents the desired image, $\boldsymbol{R}$ represents the reconstruction matrix, $\Delta\boldsymbol{v}^{(k)}$ represents the FEM simulated voltage difference vector between homogenous and inhomogenous (without target and with target) cases and $w^{(k)}$ represents the pixel weighing matrix.[52]

Figures of merit

Desired performance measures of an ideal EIT reconstruction algorithm are established and organized in several FoM. These FoM are valid for point targets with properties listed in Section 4.5.2. A $\frac{1}{4}$-amplitude set labeled as $\hat{\boldsymbol{\sigma}}_q$ contains all reconstructed image pixels $[\hat{\boldsymbol{\sigma}}]_i$ greater than $\frac{1}{4}$ of the maximum amplitude in the reconstructed image. The center of gravity (CoG) of both $\hat{\boldsymbol{\sigma}}$ and $\hat{\boldsymbol{\sigma}}_q$ is calculated. Parameters r_t and r_q then represent the distance of the CoG from the domain center.

Amplitude response

The amplitude response (AR) metric indicates the ratio of pixel amplitudes in the target image to the reconstructed image. A spherical target of a conductivity of σ_t with a volume of V_t in the electrode plane in a body of a homogenous reference σ_r is assumed. AR is the most important FoM and should be constant for any target position. Reconstruction matrices are often scaled in a way that AR $= 1$ for small spherical targets with $\frac{\sigma_t - \sigma_r}{\sigma_r} \approx 1$ in the center of the domain. AR is calculated according to Equation (4.18).

$$\mathrm{AR} = \frac{\Sigma_k [\hat{\boldsymbol{\sigma}}]_k}{V_t \frac{\sigma_t - \sigma_r}{\sigma_r}} \tag{4.18}$$

Position error

The position error (PE) metric indicates the extent to which reconstructed images faithfully represent target position and should be ideally small and similar for all radial target positions. It is calculated according to Equation (4.19).

$$\mathrm{PE} = r_t - r_q \tag{4.19}$$

A positive PE value indicates a push of the reconstructed image to the domain center.

Resolution

The resolution (RES) metric indicates the size of the reconstructed target as fraction of the domain and is equivalent to the point spread function (PSF). It should be uniform and small at all domain locations to accurately represent the shape of the target conductivity distribution. RES is calculated according to Equation (4.20).

$$\mathrm{RES} = \sqrt{\frac{\Sigma_k [\hat{\boldsymbol{\sigma}}_q]_k}{\mathrm{A}_0}} \tag{4.20}$$

where $\Sigma_k [\hat{\boldsymbol{\sigma}}_q]_k$ represents the area of the $\frac{1}{4}$-amplitude set and A_0 represents the area of the entire reconstructed domain in pixels.

Shape deformation

The shape deformation (SD) metric indicates the extent of non-circular artefacts that occur when reconstructing circular targets. It corresponds to the fraction of the reconstructed $\frac{1}{4}$-amplitude set which doesn't fit within a circle of an equal area and should be small and uniform. Reconstructed images will otherwise lead to an incorrect interpretation of results. SD is calculated according to Equation (4.21)

$$\mathrm{SD} = \frac{\Sigma_{k \notin C} [\hat{\boldsymbol{\sigma}}_q]_k}{\Sigma_k [\hat{\boldsymbol{\sigma}}_q]_k} \tag{4.21}$$

where C represents a circle centered at the CoG of $\hat{\sigma}_q$ with an area of $\frac{1}{4}$-amplitude given in pixels.

Ringing

The ringing (RNG) metric indicates how much the main reconstructed target area is surrounded by areas of an opposite sign. It can be compared to an overshoot of a second-order system. RNG should be low and uniform. Big overshoots might easily result in the incorrect interpretations of the reconstructed images. One example is negative ringing between lungs. This produces a conductive pattern which might be mistaken for the heart. RNG expresses the ratio of image amplitude of an opposite sign outside circle C to image amplitude within C and is computed according to Equation (4.22).

$$\mathrm{SD} = \frac{\sum_{k \notin C \& [\hat{\boldsymbol{\sigma}}]_k < 0} [\hat{\boldsymbol{\sigma}}]_k}{\sum_{k \in C} [\hat{\boldsymbol{\sigma}}_q]_k} \tag{4.22}$$

Noise figure

The noise figure (NF) metric indicates how much random measurement noise is amplified in the reconstructed image. It corresponds to the ratio of output to input signal-to-noise ratio (SNR). In the case of EIT, SNR is defined as $\mathrm{SNR} = \frac{\mathrm{mean}|\mathrm{signal}|}{\mathrm{std}(\mathrm{signal})}$ in terms of image amplitude. The reason behind the modification of the SNR function (as opposed to its typical counterpart) is the tendency of linear image reconstruction to conserve amplitude rather than energy. A trade-off between good noise performance and other figures of merit is always present. NF should be low and ideally tuned to the EIT device used for measurements. It is generally recommended to keep $\mathrm{NF} = 0.5$ for GREIT. NF is computed according to Equation (4.23).

$$\mathrm{NF} = \frac{\mathrm{SNR}_{out}}{\mathrm{SNR}_{in}} = \frac{\frac{\mathbb{E}[\mathrm{mean}|\hat{\boldsymbol{x}}_t|]}{\mathbb{E}[\mathrm{std}(\hat{\boldsymbol{x}}_n)]}}{\frac{\mathbb{E}[\mathrm{mean}|\boldsymbol{y}_t|]}{\mathbb{E}[\mathrm{std}(\hat{\boldsymbol{y}}_n)]}} \tag{4.23}$$

Chapter 5

Neural networks

The optimization over many parameters without the need for excessive measuring is crucial to EIT method development. To achieve this, neural networks (NNs) are often used to optimize not only electrode positions and I-M patterns, but also image reconstruction.

The first simple systems mimicking human brain behaviour emerged in the 1940s. However, these so called artificial NNs only started gaining in popularity with the massive increase in computational power in recent years. Nowadays they play a crucial role in many fields such as image processing or autonomous driving. The main idea behind NNs is inspired by neurons. Neurons pass information to further neurons only when time and spatial summation of the incoming signal exceeds a certain threshold. This non-linear behavior is applied in modern NNs.[53]

5.1 Perceptron

The elementary element of an NN is called a perceptron. It is similar to a neuron and has several real number inputs, internal trainable weights and bias, and one real number output. All inputs are weighed with perceptron weights and then summed. Finally, an activation function is applied and the output is computed. The specific behavior of a perceptron with output o is defined by Equation (5.1)

$$o = f\left\{\sum_{k=1}^{n} w_i x_i + b\right\} \tag{5.1}$$

where n represents the number of inputs and weights, f represents the activation function, w_i represent perceptron weights, x_i represent inputs, and b represents bias. This perceptron alone can be trained as a binary linear classifier with an output of either 0 or 1 if a binary step function with a learned threshold is used as the activation function.[53]

5.2 Activation functions

Activation functions are responsible for the non-linear behavior of NNs. There are more variants which are used, depending mainly on NN type and use.

5.2.1 Sigmoid

One of the most widely used activation functions is the sigmoid. It maps the whole real axis to a range of $[0,1]$ and is therefore mostly used for probabilistic outputs. It is differentiable and has a smooth gradient, which is beneficial for the learning process. The output is defined by Equation (5.2).

$$f(x) = \frac{1}{1+e^{-x}} \tag{5.2}$$

5.2.2 Tanh

The hyperbolic tangent (tanh) activation function is very similar to the sigmoid in shape. As opposed to the sigmoid function, however, the tanh function maps the whole real axis to a range of $[-1,1]$. It is often used in inner layers of NNs and helps with centering data for next layers. It also supports easy learning thanks to differentiability and a smooth gradient. The output is defined by Equation (5.3).

$$f(x) = \frac{e^{x}-e^{-x}}{e^{x}+e^{-x}} \tag{5.3}$$

5.2.3 ReLU

Other activation functions aren't differentiable in the whole domain and therefore require definition of derivatives in specific points. One example is the rectified linear unit (ReLU) function, which consists of two linear functions with an output defined by Equation (5.4).

$$f(x) = \max(0,x) \tag{5.4}$$

All negative inputs are mapped to zero and only the maximum positive input is taken into consideration and directly fed through to the output. ReLU is simple to implement and very popular mainly in convolutional layers. There is a slight modification called leaky ReLU which maps negative values linearly to smaller negative values. It helps the network produce a non-zero gradient for negative inputs as well as for positive ones. Leaky ReLU is defined by Equation (5.5).[53,54]

$$f(x) = \begin{cases} x & \dots \quad x>0 \\ ax & \dots \quad x\leq 0 \end{cases} \tag{5.5}$$

All mentioned activation functions are depicted in Figure 5.1

5.3 Fully connected layers

A NN completely composed of perceptrons is called fully connected (FC). All neurons in one layer are connected to all neurons in both the previous and next layers. This way each neuron influences all neurons in the following layer and is influenced by all neurons in the preceding one. To train the whole NN, all weights

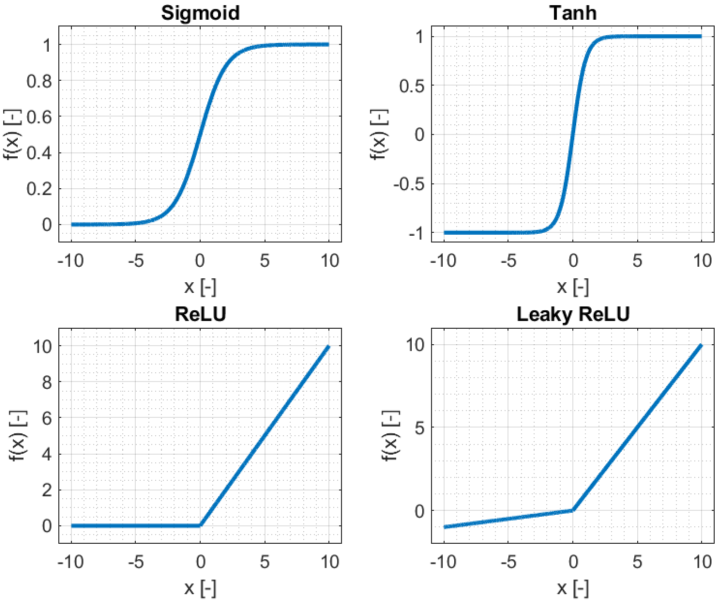

Figure 5.1: Activation functions for NNs.

and biases for all perceptrons have to be learned, which is very memory-demanding. When processing an image with a size of 2 megapixels, just the input layer would have to contain 2 million neurons. Perceptrons of FC layers are present as the output in nearly all classification NNs. An example of FC layer with 4 inputs, 1 hidden layer and 3 outputs is depicted in Figure 5.2.

5.4 Convolutional layers

Due to the pitfalls of using FC NNs for tasks concerning images such as classification or segmentation, a better approach was designed based on convolution. Convolution is utilized in the form of matrix multiplication, where a learnable kernel of a predetermined size is convolved with the input image. Usually a square kernel slides along the whole input image and extracts local features into an output called a feature map. There are several key parameters in the convolution process. Apart from an input image and kernel, stride and padding determine the output feature map. A simple example of a kernel might be a diagonal 3x3 matrix which detects diagonal edges in the input image during convolution.[54] The principle on fimage convolution may be seen in Figure 5.3.

5.4.1 Padding

An inherent property of convolution in that it shrinks the output compared to the input depending on the stride size. Therefore, padding may be added to the input image to keep the original dimensions in the output image as well. Several padding types are commonly used depending on the application.[54,55]

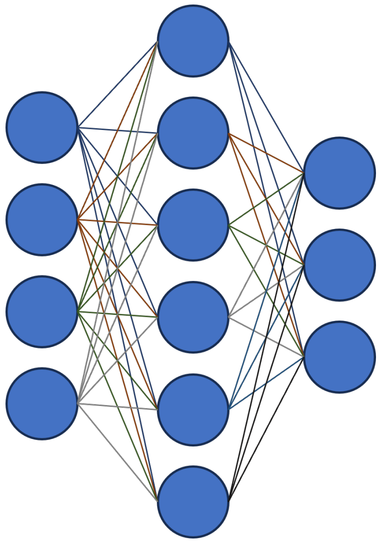

Figure 5.2: A fully connected NN with neural connections indicated by colored lines.

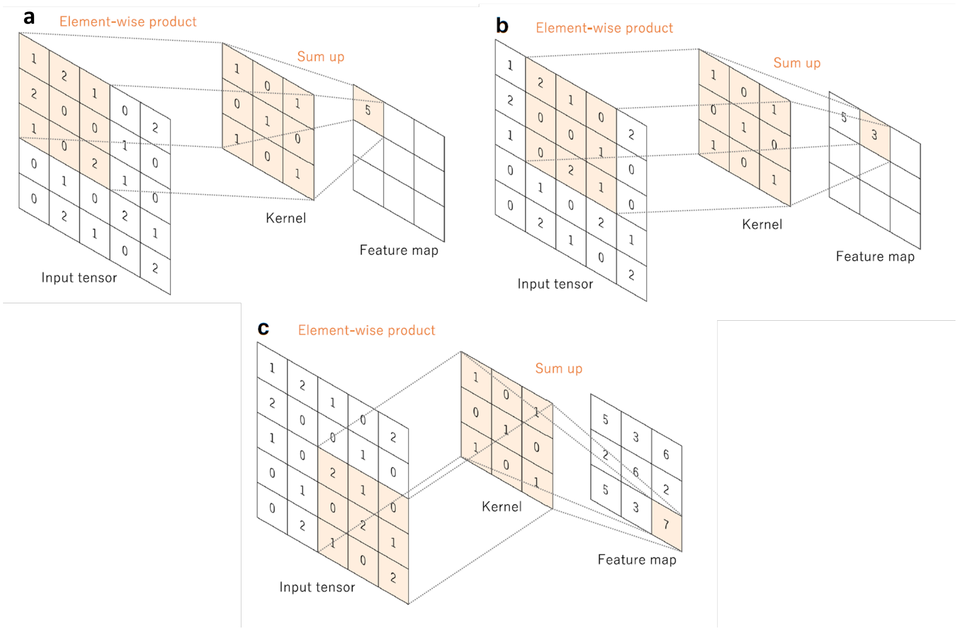

Figure 5.3: The principle of a convolutional neural network. Subfigures a, b, and c show steps 1, 2, and 9 of the convolution, respectively. This figure was taken from [54].

- Zero padding adds zeros around the image.
- Replication padding repeats values nearest to the padded pixels.
- Reflection padding mirrors values from inside the image to the padded pixels.

An example of the convolution of a padded image may be viewed in Figure 5.4.

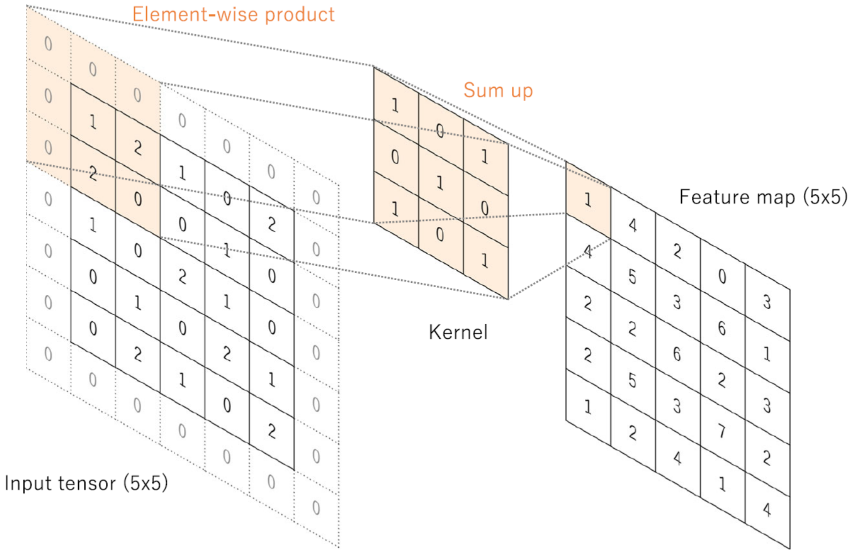

Figure 5.4: The principle of padding in a convolutional neural network. Here a simple zero padding was added to the input image increasing its size by one pixel in each direction. This figure was taken from [54].

5.4.2 Pooling

In order to extract abstract features and lower image dimensions, a pooling operation may be used. It is also applied through convolution and is based on mathematical operations. The non-learnable kernel with a predefined mathematical operation slides along the whole image and extracts features.[54, 56]

- Min pooling extracts the minimum value from the image within the current kernel position.
- Max pooling extracts the maximum value from the image within the current kernel position.
- Average pooling computes the average value of all pixels within the current kernel position.

5.5 Network training

The main purpose of NN training is to learn the weights of convolutional and FC layers. In the beginning, random weights are assigned to all learnable parameters and then a set of training samples is fed to the NN together with ground truth information. During a forward pass, an output is generated which is then compared to the ground truth. In the process of back-propagation governed by gradient descent, network weights are adjusted according to computed derivatives based on the output difference. The overall goal of the training process is the minimization of a loss function $\mathcal{L}$ usually defined as the mean square error (MSE) between NN output $\sigma(\theta)$ and ground truth σ_{ref} according to Equation (5.6).

$$\mathcal{L}_{MSE}(\sigma, \sigma_{ref}, \theta) = \frac{1}{N}\sum_{k=1}^{N}(\sigma(\theta)^k - \sigma_{ref}^k)^2 \tag{5.6}$$

where σ_{ref}^k represents the k-th pixel of the ground truth output, θ represents NN parameters and N represents the number of pixels.[53]

5.5.1 Regularization

A regularization term can be added to the loss function $\mathcal{L}$ which takes into account the size of the NN parameters. The hyperparameter λ, which sets the importance of the regularization term in the loss function, then enables balancing variance and bias according to Equation (5.7).

$$\mathcal{L}(\sigma, \sigma_{ref}, \theta) = \frac{1}{N}\sum_{k=1}^{N}(\sigma(\theta)^k - \sigma_{ref}^k)^2 + \lambda\|\theta\| \tag{5.7}$$

It is important not to overfit the NN to training data and let it generalize for input data not matching the training dataset as well. Therefore, the input dataset is usually divided into training, validation and test parts. The validation dataset is used during training to monitor the capability of the NN to generalize outside the training dataset. Finally, performance is evaluated on the test dataset.[57]

5.5.2 Normalization

Some features entering the neural network might not be of the same scale as others, which might confuse the NN. Normalization is therefore performed for both the input and also inner layers to improve performance. Coefficients are usually scaled to a range of $[0, 1]$ or $[-1, 1]$. If the data has a normal distribution, it is advantageous to perform normalization to the mean and standard deviation, which leads to a standard normal distribution $\mathcal{N}(0, 1)$. Normalization leads to a more stable gradient descent behavior and prevents values from getting either extremely high or low.[58] There are several normalization types commonly used for NN layers, however, the main two are:

- Layer normalization - performs normalization over one layer.
- Batch normalization - performs normalization of small batches of training data over one layer.

Part II

Materials and methods

In this section, I will explain the approach I used during the implementation of the thesis goals. Firstly, I will describe the SW, HW and mock oxygenator used for all simulations and measurements. The second part will cover electrode position and injection-measurement pattern optimization. The third part will concern image reconstruction and processing. Even though only 3D reconstructions are considered in this thesis, resulting reconstructions will be referred to as images. The fourth part will be devoted to the post-processing of reconstructed images and thrombus identification and characterization. The final part will show the validation of the proposed methods on a real mock oxygenator.

Chapter 6

Support materials

In this section, I will cover materials that helped me in the completion of my thesis goals. I will also describe the code structure used throughout the thesis. All the materials mentioned in this section act as building blocks for simulations and measurements.

6.1 Used HW and SW

While some problems were computed on a personal laptop (Lenovo IdeaPad 5 Pro 14ITL6 laptop with a 4-core Intel i5-1135G7 processor, a maximum frequency of approximately 4.2 GHz, and 16 GB of RAM), more complex simulations were carried out on CESNET metacentrum[59] clusters with AMD EPYC 7543 32-core processors, a maximum frequency of approximately 3.8 GHz, and 16 GB of allocated RAM. Models, neural networks, statistical analysis and all other operations were programmed in MATLAB, where version 2023a[60] was installed. Unless stated otherwise, the described functions and structures were implemented by me.

6.1.1 Sciospec

A commercial Sciospec ISX-3 device produced by Sciospec Scientific Instruments GmbH (Bennewitz, Germany) with 16 electrodes was used for actual measurements. It is a single channel impedance analyzer capable of measuring in a frequency range between 100 mHz and 10 MHz and covers a significant impedance range of 300 dB (from several mΩ to several TΩ). Measurements with two to four electrodes are available, which means that bipolar measurements with a defined I-M pattern are possible. The device is depicted in Figure 6.1.[61]

Figure 6.1: The Sciospec ISX-3 impedance analyzer by Sciospec Scientific Instruments GmbH (Bennewitz, Germany), image taken from [61].

6.1.2 EIDORS

For all simulations, the Electrical Impedance and Diffuse Optical tomography Reconstruction Software (EIDORS) software suite[62] was used. It is an open-source software created with the goal to provide a free service for image reconstruction in EIT. It provides reference implementations of algorithms that researchers may use for comparison with newly developed techniques. A new version called EIDORS3D facilitates the possibility to solve 3D reconstructions, which was very useful for this thesis. There are also NETGEN[63] features integrated, which make it possible to easily create model meshes and thereby process the entire EIT simulation pipeline in EIDORS.

EIDORS operates with four primary objects represented by structures. The `fwd_model` object contains information about the FEM model, electrodes and I-M pattern properties. The FEM model is described by spatial coordinates of nodes (`nodes`), composition of FEM elements from nodes (`elements`) and boundary nodes (`boundaries`). Electrodes are described by respective nodes (`nodes`) and contact impedances (`z_contact`). The I-M pattern is described by stimulation type (voltage or current; `stimulation`), injecting electrode pairs (`stim_pattern`) and measuring electrode pairs (`meas_pattern`). The `data` object contains information about the simulated data frame. All the measurements done according to the selected I-M pattern are stored in the `meas` vector. The `inv_model` object contains information necessary for image reconstruction. A specific EIT modality can be chosen under `reconst_type`, a prior matrix can be adjusted under `R_prior` and a hyperparameter may be specified under `hyperparameter`. The `image` object contains the reconstructed or simulated conductivities of FEM elements under `elem_data`.[44]

Several EIDORS and NETGEN functions were frequently used throughout the thesis and are listed below.[44]

- The `ng_mk_gen_models` function was used for generating the model mesh and `fwd_model` object based on input parameters. Mesh shape was generated according to a `.geo` file or string description of individual geometric components forming its boundaries. The generated mesh is denser around specified electrodes and its refinement can be adjusted.

- The `ng_mk_fwd_model` function was used to create a `fwd_model` object according to a `.vol` mesh.
- The `mk_image` function then created an `image` according to the `fwd_model` object and specified conductivity values.
- The `calc_jacobian` function was used to compute the Jacobian for a given `image` according to the perturbation method.
- The `mk_stim_patterns` function was used to specify an I-M pattern structure according to the selected number of electrodes and I-M number combination.
- The `fwd_solve` function then solved the FP for given conductivities according to the selected I-M pattern.
- The `inv_solve` function was used to solve the IP for given homogeneous and inhomogenous measurements according to the selected reconstruction algorithm.
- The `show_fem_enhanced` function enabled nice customized visualizations of FEM models.

6.2 Mock oxygenator

An oxygenator from Maquet Cardiopulmonary GmbH (Rastatt, Germany) called HLS Module Advanced (depicted in Figure 6.2) was chosen as the main research object. It comprises two compartments divided by a separation grid and two pairs of inlets and outlets for air and blood, respectively. In the first compartment blood passes through both gas-exchange fibers (made from PMP) and heat exchange fibers (made from polyurethane). In the second compartment only gas-exchange takes place.

In previous work a mock oxygenator was designed and fabricated according to the HLS Module Advanced. This mock is used for all simulations and real measurements. It shares the same inner-volume dimensions (a width and depth of 9 cm and a height of 5 cm) where blood flows and is being oxygenated. Additionally, the mock includes drilled holes prepared for electrodes which facilitate direct contact with blood. The electrode positions are placed at both top and bottom planes in a symmetrical grid. Because of the construction of the actual oxygenator, it wouldn't be possible to insert electrodes on the sides, therefore no holes were drilled there. A separation grid was created in the middle of the mock to emulate the compartment divider. The mock is constructed only for static tests without any possibility for circulation. For fabrication simplification all fibers were left out.

6.2.1 FEM model

The FEM model was created using the `ng_mk_gen_models` function. It is composed of three basic geometrical primitives, one block and two planes. The `orthobrick` command created the block for given extremes in x,y and z axes. The middle of the block lies in the coordinate system origin with extremes for each axis (Ex_{ax})

Figure 6.2: HLS Module Advanced oxygenator by Maquet Cardiopulmonary GmbH (Rastatt, Germany).[24]

being: $Ex_x = [-4.5, 4.5]$ cm, $Ex_y = [-4.5, 4.5]$ cm, $Ex_z = [-2.5, 2.5]$ cm. The first plane coincides with top of the brick and contains all possible electrodes. It would be possible to make a separate FEM model for different electrode positions, but it is computationally much more efficient to create just one model with all possible electrode positions densely meshed. The maximal mesh-size was set to 2 mm as a compromise of good simulation accuracy and feasible memory requirements. The final generated mesh (depicted in Figure 6.3) includes 373,202 elements and 70,914 nodes. The separation grid, with a conductivity of 1×10^{-6} S.m^{-1} is modeled as individual rods according to cylinder equation $(x - x_c)^2 + (z - z_c)^2 < r_r^2$ or $(y - y_c)^2 + (z - z_c)^2 < r_r^2$ depending on rod direction. Variables x_c, y_c and z_c correspond to rod center coordinates and r_r corresponds to the rod radius. The separation grid consists of elements that are inside cylinders described by the equations above. It would be possible to generate the separation grid more realistically with finer mesh, but far more elements and memory would be needed, which is not worth the benefit of slightly better accuracy.

6.3 Electrode position generation

During the process of FEM model creation, nodes corresponding to respective electrodes were saved for all plausible electrode positions limited by the holes drilled into the mock oxygenator. The `findNearestPlausibleElectrodePosition` was implemented for finding the nearest plausible electrode position according to the L2 norm. When plausible Euclidean coordinates of an electrode are determined, my implemented `getElectrodeNodes` function finds corresponding nodes, which are then used in the `fwd_model.electrode` to specify used electrodes.

A `generateElectrodePositions` function for the generation of electrode positions was also created. The number of electrodes at the top and bottom plane of the

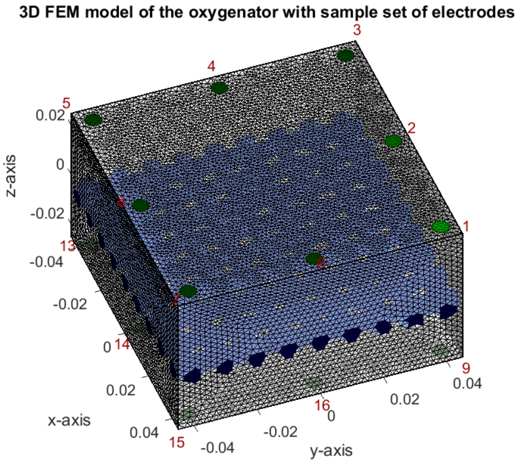

Figure 6.3: The generated FEM model of the oxygenator with a sample set of electrodes (depicted in green) and separation grid (depicted in blue). Red is used to number visualized electrodes.

oxygenator can be specified. There is nothing to suggest that one side of the oxygenator should be disproportionately populated with electrodes, so a balanced case is considered in this thesis. Eight electrodes are therefore generated on the top and eight electrodes at the bottom. Generated electrode centers lie on radials evenly dividing the top and bottom planes (radials are $\frac{360°}{8} = 45°$ apart). A sample set of electrodes together with highlighted radials is depicted in Figure 6.4. This function enables both random and constrained position generation on the radials. Random distances from top or bottom plane centers are generated from a normal distribution $\mathcal{N}(\mu_{pos}, \sigma_{pos})$ of a given mean μ_{pos} and standard deviation σ_{pos}.

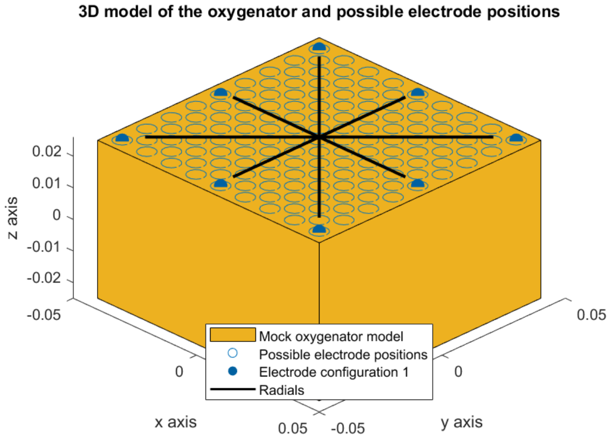

Figure 6.4: A sample set of generated electrode locations with highlighted radials.

6.4 Target generation

For inhomogenous simulations, spherical targets are generated using the function `generateTargets`. A probability function of thrombi occurrence was derived based on the assumed flow distribution. There weren't any available data on flow patterns in the HLS Module Advanced specifically, so a simple Gaussian approximation was chosen. A 3D Gaussian with mean values $\mu_x = 0$, $\mu_y = 0$ and $\mu_z = 0$ and standard deviations of $\sigma_x = 0.045$, $\sigma_y = 0.045$ and $\sigma_z = 0.025$ was designed based on Equation (6.1).

$$p(x, y, z) = \frac{1}{\sigma_x \sigma_y \sigma_z (2\pi)^{\frac{3}{2}}} e^{-\frac{(x-\mu_x)^2}{\sigma_x^2} - \frac{(y-\mu_y)^2}{\sigma_y^2} - \frac{(z-\mu_z)^2}{\sigma_z^2}} \tag{6.1}$$

A likelihood function of thrombi occurrence was created by analytically inverting the probability density function values for all voxels inside the FEM model according to equation 6.2.

$$\mathcal{L}(x, y, z \in \text{oxygenator}) = \sigma_x \sigma_y \sigma_z (2\pi)^{\frac{3}{2}} e^{\frac{(x-\mu_x)^2}{\sigma_x^2} + \frac{(y-\mu_y)^2}{\sigma_y^2} + \frac{(z-\mu_z)^2}{\sigma_z^2}} \tag{6.2}$$

The highest likelihood of thrombus occurrence based on this model is in the corners of the oxygenator where flow tends to stagnate the most. A histogram of likelihood values is depicted in Figure 6.5a. This distribution doesn't apply for the real measurements which are static without any flow.

A cumulative distribution function (CDF) (depicted in Figure 6.5b) was created for the possibility of the pseudo-random selection of thrombi locations based on a given CDF percentile. Random noise of a low amplitude was added to the CDF value which results in slightly different thrombi locations even for the same CDF values. The likelihood distribution is symmetrical with respect to the center of the oxygenator with ellipsoidal isolines. Therefore more voxels with the same respective thrombi likelihood exist for one concrete CDF value. A random sample is chosen from these, which leads to better coverage of the entire model volume. An example of a generated set of thrombi is depicted in Figure 6.5c

Targets are incorporated into the model in the same way as the separation grid. All FEM elements which are inside the generated target are selected based on the sphere equation $(x - x_c)^2 + (y - y_c)^2 + (z - z_c)^2 < r_t^2$, where x_c, y_c and z_c represent center coordinates of the target and r_t represents the target radius. Respective conductivities are then adjusted.

The conductivity of blood in the FEM model is set at 6.62×10^{-1} S.m^{-1} according to the IT'IS Foundation database.[64] The conductivity of targets emulating clots was set to approximately one tenth of blood conductivity (6.62×10^{-2} S.m^{-1}) according to.[34] This difference in conductivities for blood and thrombi is probably higher than an average conductivity difference in vivo and represents the best case scenario for thrombus detection.

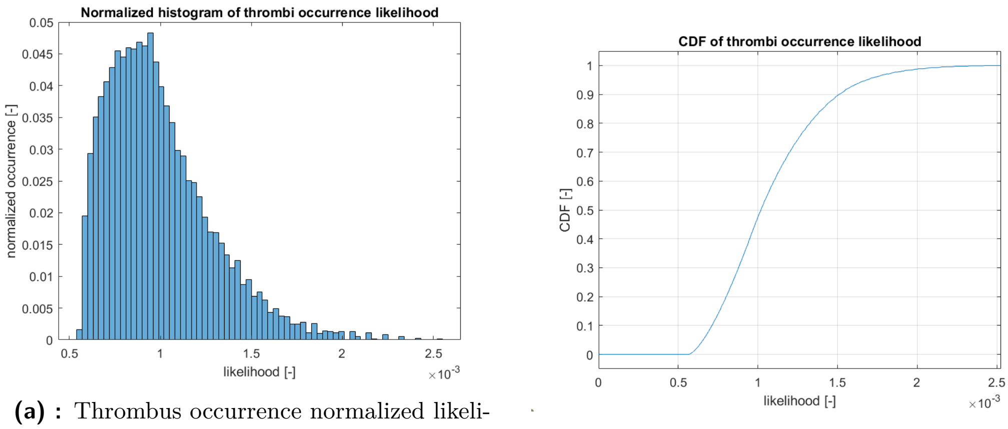

(a) : Thrombus occurrence normalized likelihood histogram.

(b) : Thrombus occurrence likelihood CDF.

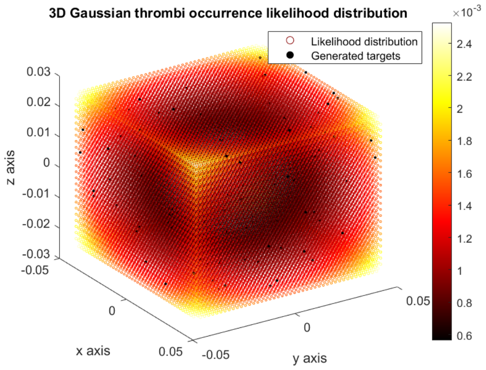

(c) : 3D thrombus occurrence likelihood distribution with a sample set of generated thrombi.

Figure 6.5: Thrombus occurrence likelihood representation.

6.5 Oxygenator object structure

An `oxygenator` structure containing all simulation parameters was created to enable simple global parameter changes. It contains several substructures with data organized coherently in all of them:

- The `data` structure contains information about oxygenator dimensions and extremes.
- The `electrodes` structure contains specifications of the electrode generation process or electrode diameters.
- The `FEM` structure contains forward and inverse model images, I-M pattern information, all plausible electrode position nodes, and homogeneous conductivity values.
- The `NNdetection` structure contains parameters for the NN used for thrombi

detection.

- The `NNelectrodes` structure contains parameters for the NN optimization of electrode positions.
- The `NNreconstruction` structure contains parameters for the reconstructive NN.
- The `reconstruction` structure contains reconstruction parameters used for both the EIDORS `inv_solve` function and the NN.
- The `separationGrid` structure contains all information about the separation grid.
- The `targets` structure specifies parameters for target generation such as target diameter or default CDF generation percentiles.
- The `visualizations` structure contains specifications for FEM visualization and color options for other visualizations.

The `setOxygenatorParam` function is responsible for saving all required data and exporting the structure which is later loaded into other scripts.

Chapter 7

Preliminary experiments

Many preliminary simulations were conducted to assess the influence of various parameters on measured voltages and the Jacobian. Four electrode sets (depicted in Figure 7.1) were constructed for the sake of these experiments. They were created under the assumption that thrombi are likely to be present in the corners and on the edges of the oxygenator according to the inverted Gaussian distribution described earlier by Equation (6.2). Electrode set 1 covers the full oxygenator volume and therefore should be able to catch all possible conductivity changes. The problem of this arrangement is a low sensitivity near the center of the oxygenator. Electrode sets 2 and 3 should better cover the center of the oxygenator and still be able to sufficiently cover its edges and corners. Electrode set 4 should be able to perfectly cover corners and edges, but will again have a lower sensitivity to thrombi found in the center of the oxygenator.

7.1 Injection-measurement pattern design

The reciprocal geometry of the oxygenator and electrodes is unique and no recommended I-M pattern exists for this arrangement. A general I-M pattern was designed

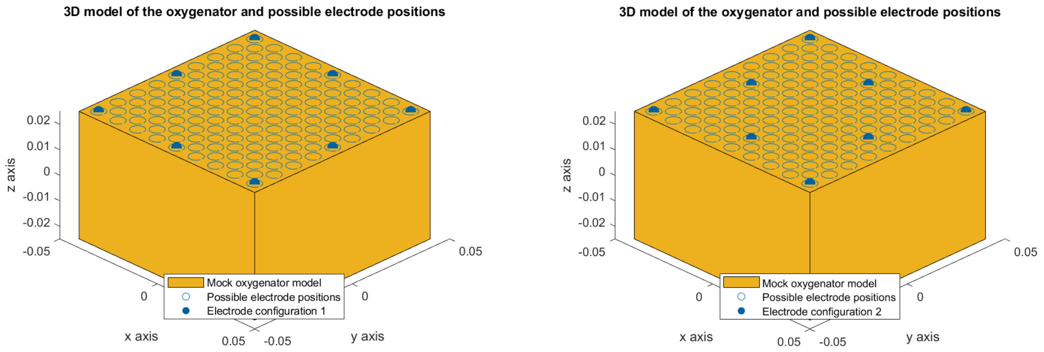

(a) : Electrode set 1.

(b) : Electrode set 2.

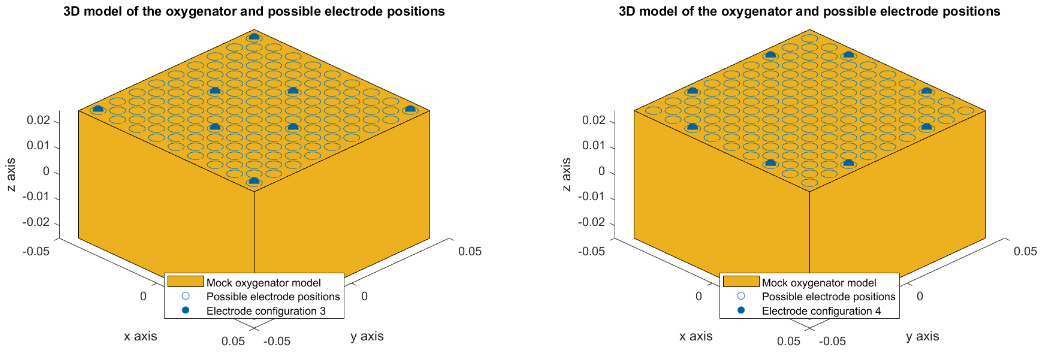

(c) : Electrode set 3.

(d) : Electrode set 4.

Figure 7.1: Electrode sets for preliminary experiments.

based on electrode set 1 (depicted in 7.1a). All sensible pairs of electrodes were chosen and semi-automatically inserted into the EIDORS `fwd_model.stimulation` structure. Chosen electrode pairs are depicted in figures 7.2 and 7.3. They were chosen in such a way, that their signals would include both intra-plane and inter-plane excitations and measurements. All electrode pairs were used as both injecting and measuring. Only independent measurements in the sense of reciprocity were taken into account. When deciding between reciprocal measurements, the electrode pair with the lowest electrode number was selected as the injecting pair. This means that for a measurement two hypothetical electrode pairs 5-8 and 6-7, the 5-8 pair would be selected as injecting and the 6-7 pair as measuring. This leads to an overall pattern with non-equal number of measuring pairs for each injecting pair. EIDORS forward and inverse solvers are capable of handling this case, however, so no adjustments were necessary for the FP and IP solution.

The designed I-M pattern includes 1,560 measurements on 61 stimulating pairs of electrodes. This is a significant increase compared to the generally used 104 non-reciprocal measurements for a typical adjacent I-M pattern. It is also clear that some of the measurements are of a low sensitivity. For example, when injecting current into two adjacent electrodes on one side of the oxygenator, not much useful information can be gained by measuring on an adjacent pair of electrodes on the other side of the oxygenator. Therefore, the most sensitive measurements were selected, enabling the acquisition of useful signal without overly amplifying noise.

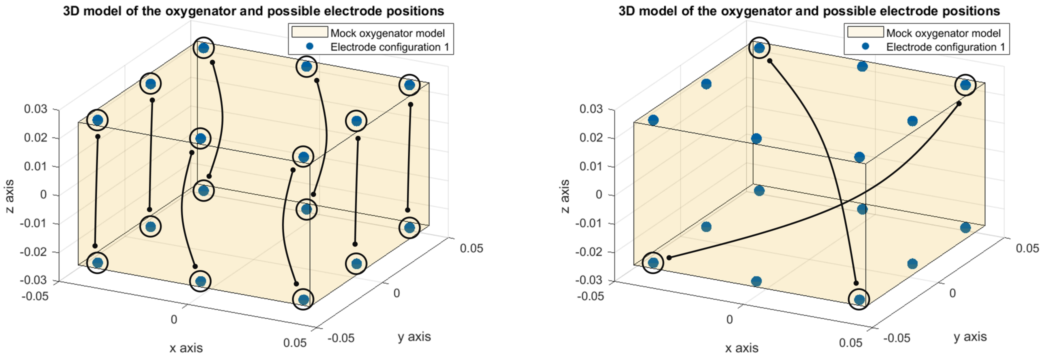

(a) : Straight inter-plane pairs covering oxygenator walls.

(b) : Inter-plane corner diagonal pairs covering oxygenator diagonals.

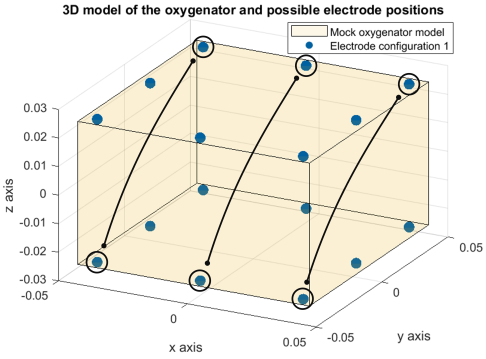

(c) : Inter-plane edge diagonal pairs covering walls and the oxygenator center, other sets of pairs generated by 90, 180 and 270 degrees rotation of these along z-axis.

Figure 7.2: Inter-plane pairs in a general I-M pattern.

7.1.1 Selecting most sensitive measurements

Three methods based on Jacobian analysis were considered for measurement selection. Two of them - the L1- and L2-norms - assess individual measurement sensitivity. These selection methods stem from the idea that the greater the magnitude of the sensitivity Jacobian vectors (rows with elements corresponding to the given measurement), the better the ability of the measurement to mirror conductivity changes to voltage changes. Vectors with greater magnitude are also more robust to noise and lead to smaller posterior variance for the inverse problem. Both the L1-norm and L2-norm were used to sort measurements according to equations (7.1) and (7.2), respectively.[65]

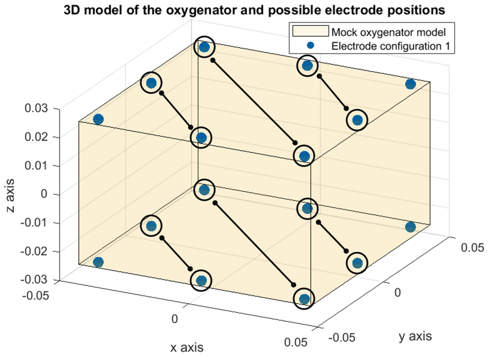

(a) : Intra-plane diagonal pairs covering the inner space of the plane, other sets of pairs were generated by a 90 degree rotation of these along z-axis.

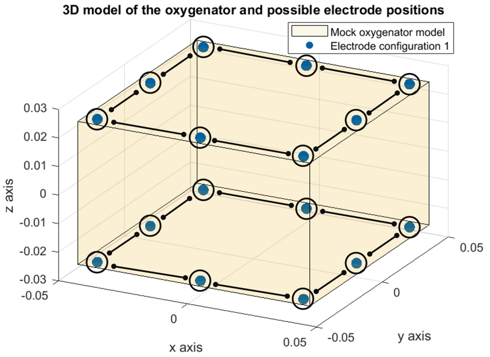

(b) : Adjacent intra-plane pairs covering oxygenator edges.

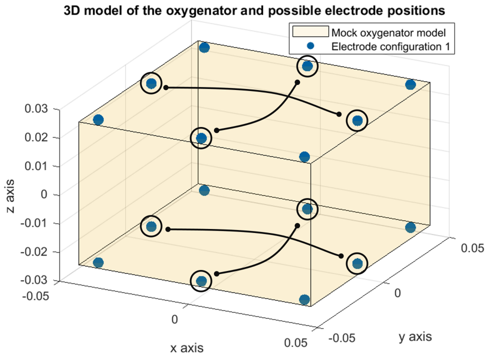

(c) : Intra-plane cross pairs covering oxygenator walls.

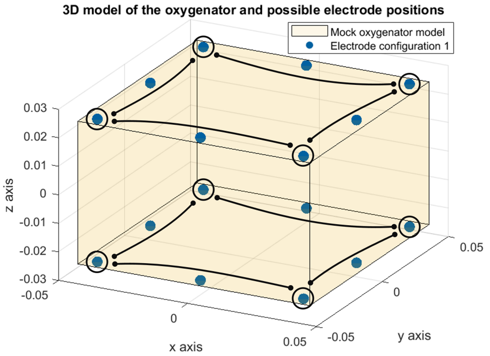

(d) : Intra-plane corner-corner pairs covering oxygenator edges for cases where central electrodes are moved closer to the center.

Figure 7.3: Intra-plane pairs in a general I-M pattern.

$$\|J_{meas}\|_1 = \sum_{k=1}^{n_M} |J_{meas,k}| \tag{7.1}$$

$$\|J_{meas}\|_2 = \sqrt{\sum_{k=1}^{n_M} (J_{meas,k})^2} \tag{7.2}$$

In this equation, J_{meas} represents a single Jacobian element corresponding to measurement and n_M represents the number of finite elements. However, these norms are computed for each measurement independently and may lead to the choosing of similar element during final selection. While both the chosen measurements may then have high L1- or L2-norm values, they will not bring additional information to the solution when used together as opposed to just one being utilized.

The third method is based on an approach developed by Onsager et al. in 2021[65] and is aimed at finding the most sensitive I-M pattern that doesn't contain these similar measurements. Similar measurements are characterized by their corresponding sensitivity vectors being almost parallel (i.e. they cover the same elements). Independent measurements are, on the other hand, characterized by their corresponding sensitivity vectors being orthogonal (they cover different elements). The selection of independent measurements is beneficial, as it results in a smaller posterior covariance for the inverse problem. The best I-M patterns chosen based on this selection method include long and mutually orthogonal sensitivity vectors. The sensitivity parallelotope volume, formed by constituent sensitivity vectors, is a good measure for the previously described features. For the case of two sensitivity vectors, the parallelotope forms a part of 2D plane. A parallelotope consisting of three vectors forms a 3D body. The volume of an n-dimensional parallelotope may be computed in two basic ways. One approach utilizes SVD. The Jacobian J may be decomposed according to Equation (7.3) into a total of three matrices U, Σ and V. Matrices U and V are positive semi-definite and contain left u_i and right v_i singular vectors. They can be derived by the eigendecomposition of matrices J^TJ and JJ^T, respectively, and represent rotation. The Σ matrix, which represents scaling, is a diagonal matrix containing the singular values σ_i of J.

$$J = U\Sigma V^T \tag{7.3}$$

The n-dimensional parallelotope formed by n sensitivity vectors has a volume of V_n, which is calculated according to Equation (7.4) as the square root of the multiplied singular values.

$$V_n = \sqrt{\prod_{k=1}^{n} \sigma_k} \tag{7.4}$$

An equivalent option to get the volume is to calculate the square root of the determinant of the $J_{meas}J_{meas}^T$ matrix according to Equation (7.5). Matrix J_{meas} contains only the selected sensitivity vectors from the Jacobian, from which we wan to compute the volume.

$$V_n = \sqrt{\det(J_{meas}J_{meas}^T)} \tag{7.5}$$

An algorithm for selecting measurements based on the largest parallelotope volume is described in Algorithm 1. It was necessary to scale the Jacobian using specific coefficients to keep the resulting volume within a reasonable range. Without any correction, the value was close or equal to either zero or infinity after only a few tens of iterations. Overall results of measurement selection are described in Section 12.1.

7.2 Influence of input parameters on measurements

In order to assess if the I-M protocol optimization can lead to better measurements, several simulations were done. The goal was to observe changes in voltage measurements and the Jacobian caused by the change of input parameters (e.g. electrode positions, I-M pattern, or target conductivity). The influence of these parameter changes was observed individually to allow for the unambiguous determination of changes caused. Noise wasn't considered in these simulations.

Algorithm 1 Pseudocode for the selection of measurements based on largest parallelotope volume

Used variables: n ... number of selected measurements, J ... Jacobian, n_V ... total number of measurements in the I-M pattern, cF ... a flag for finding a suitable coefficient for Jacobian, cI ... an iteration counter for the suitable coefficient search, v ... the computed volume, J_p ... a matrix containing selected sensitivity vectors with candidate vectors, I ... indices of measurements chosen in ascending order, σ_k ... k-th singular value, mV ... maximum volume, mVI ... maximum value index
Inputs: J, n
Output: I

```
procedure selectMostSensitiveMeasurements($J$, $n$)
    for $m \leftarrow 1$ to $n$ do    ▷ Until number of measurements wanted is achieved
        $mV \leftarrow 0$, $mVI \leftarrow 0$
        for $p \leftarrow 1$ to $n_V$ do
            if $p \notin I$ then    ▷ Except for measurements already selected
                $cF \leftarrow$ false
                while $cF$ is false do    ▷ Search for coefficient scaling volume
                    $J_p \leftarrow [J(I); J(p)]$    ▷ Add potential measurement to the existing selection
                    $\sigma_k \leftarrow \mathrm{SVD}(J_p J_p^T)$, $v \leftarrow \sqrt{\prod_{k=1}^{n} \sigma_k}$    ▷ Find $\sigma_k$, compute volume
                    if $v < 10^{-200}$ then    ▷ Volume too small
                        $J \leftarrow J1.3^{\frac{1}{cI}}$
                    else if $v > 10^{100}$ then    ▷ Volume too large
                        $J \leftarrow J1.2^{\frac{1}{cI}}$
                    else
                        $cF \leftarrow$ true
                    end if
                    $cI \leftarrow cI + 1$
                end while
                break    ▷ Correct scaling found, continue to measurement selection
            end if
        end for
        for $p \leftarrow 1$ to $n_V$ do    ▷ All measurements are considered possible
            if $p \notin I$ then    ▷ Except for those already selected
                $J_p \leftarrow [J(I); J(p)]$    ▷ Add the potential measurement to the selection
                $\sigma_k \leftarrow \mathrm{SVD}(J_p J_p^T)$, $v \leftarrow \sqrt{\prod_{k=1}^{n} \sigma_k}$    ▷ Find $\sigma_k$, compute the volume
                if $v > mV$ then    ▷ The volume is largest so far
                    $mV \leftarrow v$, $mVI \leftarrow p$
                end if
            end if
        end for
        $I$(end+1) $\leftarrow mVI$    ▷ Add the index corresponding to largest volume to the output
    end for
end procedure
```

7.2.1 Influence of electrode positions

To evaluate influence of electrode positions on voltage measurements and the Jacobian, the four electrode sets previously introduced in Section 7 and depicted in Figure 7.1 were used. A homogeneous simulation was conducted with the separation grid present in the FEM model. A grid of 600 targets (each with a diameter of 1 cm) spanning the entire oxygenator was created for inhomogenous simulations. Target centers were equidistantly chosen in all dimensions for the thrombi not to overlap. Sparsely generated targets are shown solely in the first quadrant (for easier orientation) in Figure 7.4. Inhomogenous simulations were carried out individually for all generated targets in the grid. Therefore, the sensitivity of measurements to target position could be assessed in all oxygenator areas. Both absolute and relative voltage differences between homogeneous and inhomogenous simulations were considered. The Jacobian was computed for homogeneous cases using the `calc_jacobian` function. The designed I-M pattern introduced in Section 7.1 was used for simulations. Results are described in Section 12.2.

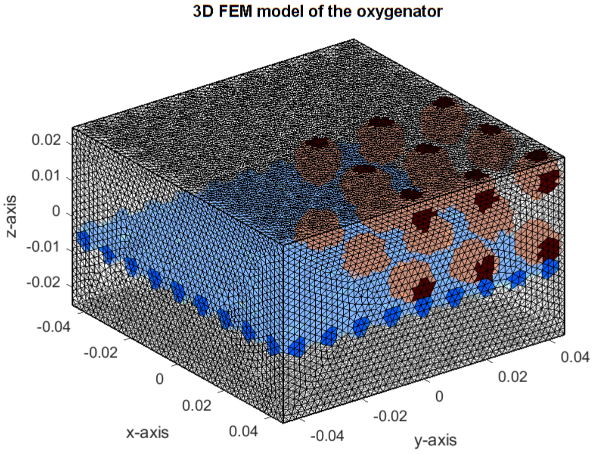

Figure 7.4: Part of generated target grid for preliminary experiments.

7.2.2 Influence of the I-M pattern

To evaluate the influence of the I-M pattern on voltage measurements and the Jacobian, electrode set 1 (introduced in Section 7 and depicted in Figure 7.1a) was used. I-M patterns were generated using the EIDORS `mk_stim_patterns` function according to the I-M convention mentioned in Section 4.3.2. These conventional I-M patterns were compared to the I-M pattern introduced is Section 7.1. Similar simulations were run as in the previous case. Results are described in Section 12.3.

7.2.3 Influence of target conductivity

To evaluate the influence of target conductivity on voltage measurements, the previously created target grid was used and conductivity was varied between 10^{-6} and 10^3 multiples of background conductivity (6.62×10^{-1} S.m^{-1}). All physiological conductivity values of human tissues are safely within this range. This extreme extent of target conductivities was chosen in order to allow general conclusions to be made based on voltage changes for conductivity values of different orders of magnitude. Electrode set 1 was used in combination with the fully designed I-M pattern (containing all 1560 measurements). Results are described in Section 12.4.

Chapter 8

Electrode position and I-M pattern optimization

Preliminary experiments revealed that optimizing electrode positions and the I-M pattern can lead to better signal acquisition. Therefore, the next step consisted of the optimization of these parameters. It was decided that electrode position and I-M pattern optimization would be decoupled from optimization of image reconstruction. The reason behind this is the bias that various reconstruction algorithms introduce into the overall optimization process. A possible approach, which would certainly lead to optimized I-M patterns and electrode positions, would be to simulate all possible combinations and choose the best one. This approach would, however, take up too much computational time and consume too many resources. Instead, a neural surrogate based on Smyl and Liu (2020)[66] was taught to understand the relationship between chosen features and electrode positions. Results are described in Section 12.3.

8.1 Training data for NN optimization of electrode position

Training data for the NN were generated using simulations and subsequent feature extraction. Firstly, 8000 random electrode sets in different spatial arrangements were generated using the `generateElectrodePositions` function. Both electrode sets with the same electrode placement and different electrode placement in the top and bottom planes were generated. Together with variations in the symmetry of electrode placement in one plane, 2918 unique electrode sets were selected using the `checkDupliciteElectrodeSets` function for NN training. An electrode set was considered unique only in cases where at least 2 electrodes differed in position from all other electrode sets. Overall, 35016 input sample vectors were at disposal.

I decided to keep only 208 measurements from the designed I-M pattern to correspond with the standard number of measurements used in practice. Measurements were selected according to the maximization of the L1- and L2-norms of sensitivity vectors and parallelotope volumes as described in Section 7.1.1. Previously calculated measurements for electrode sets 1 to 4 were used, because they are representative of randomly generated electrode positions. 36 measurements maximizing the parallelotope volume, 8 measurements maximizing the L1-norm of the sensitivity vector and

8 measurements maximizing the L2-norm of the sensitivity vector were used for each of the four electrode sets. This summed up to the required 208 measurements.

Twelve sets with six targets each were generated using the `generateTargets` function. All six targets within one set were randomly drawn from the thrombus likelihood distribution described in Section 6.4. This was done to ensure sensitivity to conductivity changes in all areas of the oxygenator. Percentiles for generation were chosen equidistantly spread from 5 to 98. All targets used for training are depicted in Figure 8.1.

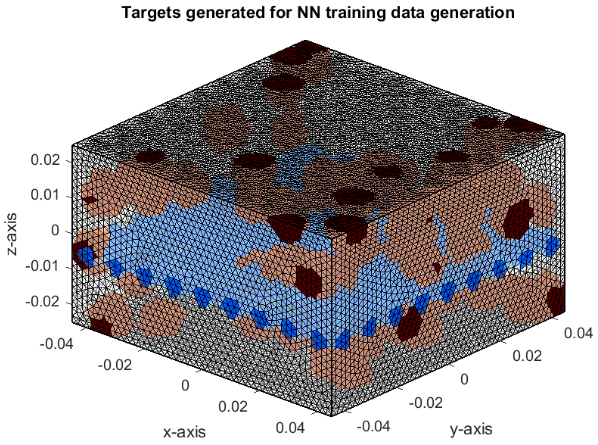

Figure 8.1: Targets for NN training data generation in red and separation grid in blue.

Several features were extracted from the simulations and then used as inputs for the NN. The Jacobian was calculated for each electrode set and a relative voltage difference was calculated from the forward problem solutions of all combinations of generated target sets and electrode sets. SVD as well as L1-norm calculation was performed on the Jacobian of all 208 sensitivity vectors corresponding to individual measurements. Features described in Table 8.1 were designed based on these calculations.

8.2 NN architecture

The used NN consists of two FC hidden layers with the number of neurons in layer 1 given by Equation (8.1) and the number of neurons in layer 2 given by Equation (8.2). Each inner layer is followed by a leaky ReLU activation function layer.

$$n_{l1} = \text{floor}\left(\sqrt{(N+2)n_{elSets}} + 2\sqrt{\frac{n_{elSets}}{N+2}}\right) \tag{8.1}$$

$$n_{l2} = \text{floor}\left(N\sqrt{\frac{n_{elSets}}{N+2}}\right) \tag{8.2}$$

The input of the NN is composed of neurons accepting selected features, while the output consists of a regression layer. This layer compares a flattened vector of the 3D coordinates of electrode positions corresponding to the respective input feature

#	Feature	Description
1	mean ΔV	mean voltage difference of the measurements
2	median ΔV	median voltage difference of the measurements
3	$Q_1(\Delta V)$	first quartile of the voltage difference of the measurements
4	$Q_3(\Delta V)$	third quartile of the voltage difference of the measurements
5	min ΔV	minimum voltage difference of the measurements
6	max ΔV	maximum voltage difference of the measurements
7	mean J	mean L1-norm of the sensitivity vectors
8	median J	median L1-norm of the sensitivity vectors
9	$Q_1(J)$	first quartile of the L1-norm of the sensitivity vectors
10	$Q_3(J)$	third quartile of the L1-norm of the sensitivity vectors
11	min J	minimum L1-norm of the sensitivity vectors
12	max J	maximum L1-norm of the sensitivity vectors
13	max σ_k	maximum singular value of the Jacobian SVD decomposition
14	min σ_k	minimum singular value of the Jacobian SVD decomposition
15	rank(J)	rank of the Jacobian based on the number of singular values bigger than one hundredth of the maximum singular value

Table 8.1: Features designed for NN optimization for electrode position training.

values to electrode positions computed by the NN based on input values. For the 16 electrodes in three dimensions used in this thesis a regression layer with 48 neurons was needed.

8.3 NN training

In total, five neural networks were trained for five different sets of input features, each of which was scaled to a range of $[0, 1]$ before training. Input features were selected based on correlation analysis in order to exclude redundancies. Input data were randomly divided into three parts to form training, validation and test datasets. 80 percent of the data was used for training and 10 percent for either validation or tests. MATLAB's `trainNetwork` function was used to train a network with parameters given in Table 8.2. A stochastic gradient descent with momentum and a gradually decreasing learning rate of an initial value of 1×10^{-3} was selected as a solver. The regularization of NN parameters was included as well as a regularization factor of 1×10^{-6}. Validation checks were performed regularly to prevent overfitting to the training dataset. Overall, 200 training epochs were completed.

8.4 Final electrode positions and I-M pattern selection

Electrode positions acquired using the optimizing NN were evaluated as un-suitable for the oxygenator case, where thrombi are most probably formed on edges and in corners. The final electrode set was therefore chosen from the designed electrode sets. Electrode sets 2 and 3 were selected as final candidates. Both of them were assigned the best I-M pattern consisting of 208 measurements combined based on

Parameter	Value
Optimizer	Stochastic gradient descent with momentum
MiniBatchSize	128
MaxEpochs	100
InitialLearnRate	1×10^{-3}
LearnRateSchedule	piecewise
LearnRateDropFactor	0.1
LearnRateDropPeriod	40
L2Regularization	1×10^{-6}
Shuffle	every-epoch

Table 8.2: Parameters of NN optimizing electrode positions.

the precomputed max L1-norm, L2-norm and parallelotope volume of the sensitivity vectors. The previously mentioned grid of 600 targets with diameters of 1 cm spanning the entire oxygenator was used for voltage difference analysis. Sensitivity analysis was conducted as well as electrode utilization analysis. Detailed results are available in Section 13.4. Finally, electrode set 2 with respective I-M pattern was selected for further research.

Chapter 9

Image reconstruction and processing

After the selection of the electrode set and I-M pattern, image reconstruction commenced. Firstly, different existing approaches were considered in the context of reconstruction and their feasibility was inspected. Backprojection algorithms perform poorly even on more complex cases in 2D, so they were omitted from consideration. Linear reconstruction algorithms still bring simplifications, but perform reasonably well and have become the gold standard for EIT reconstruction. Iterative algorithms based on Hessian matrix computations were unfortunately not feasible in this case, because of the memory demands posed by matrix computation alone. For meshes with a higher number of finite elements, none of these algorithms is usable. On the other hand, it is possible to train a reconstruction matrix using the GREIT algorithm, as it makes use of matrices with a lower number of elements. The utilization of NNs is also possible, as the number of trainable parameters can easily be adjusted using the NN architecture, which can be set as arbitrarily complex.

9.1 GREIT reconstruction

Firstly, GREIT reconstruction was optimized for the oxygenator case. Electrode set 2 with the respective I-M pattern selected in Section 13.4 was used. To prevent inverse crime a coarser mesh was created for the inverse model using the `ng_mk_gen_models` function. Parameter `-maxh` was increased tenfold from the forward model to 2×10^{-2}. This resulted in a model with 99,133 finite elements and 22,561 nodes. A reconstruction model was created using the `mk_voxel_volume` function, which maps the inverse model to an output reconstruction grid of 20 × 20 × 10 cubic voxels. This 4,000 voxel cubic grid was also used for the NN reconstruction.

The Graz consensus Reconstruction algorithm for EIT (GREIT) reconstruction matrix learning process can be influenced in more ways to reflect the user's needs. The main goal in this case was for the reconstruction matrix to perform as well as possible in the areas where thrombi are most likely deposited (oxygenator edges and corners). This can be approached in two ways. Firstly, the voxels of desired image described in Section 4.5.2 can be weighed to skew the importance of certain areas. This feature is not yet implemented in EIDORS, however, so another approach leading to the same results was prioritized. This approach is based on the specific choice of training target locations. Training targets can be easily set as input parameters of GREIT reconstruction in EIDORS. They were generated by the already implemented `generateTargets` function according to a predefined scheme based on the thrombus likelihood distribution. For each selected percentile range, a given number of thrombi was randomly drawn from the thrombus likelihood distribution. Targets were drawn on percentiles which were equidistantly spread between the limit values. In total, 6600 training targets were generated, details are described in Table 9.1.

Thrombi likelihood CDF range	Number of targets
$[0.02, 0.1]$	200
$[0.1, 0.2]$	200
$[0.2, 0.3]$	300
$[0.3, 0.4]$	400
$[0.4, 0.5]$	500
$[0.5, 0.6]$	600
$[0.6, 0.7]$	700
$[0.7, 0.8]$	800
$[0.8, 0.9]$	900
$[0.9, 0.95]$	1000
$[0.95, 0.98]$	1000

Table 9.1: Description of training targets generated for GREIT reconstruction.

GREIT reconstruction was trained on the absolute difference voltage data simulated for previously generated targets with a goal NF of 1, 2 and 3. These values were selected according to general recommendations. An NF of 0.5 is also broadly used, but wasn't achievable for this case. Target center positions from the previously mentioned grid of 600 targets were used. However, targets inside the grid were of a diameter corresponding to five percent of the oxygenator width, which is a value typically used for GREIT training. The EIDORS `eval_GREIT_fig_merit` function was used to calculate figures of merit (AR, PE, RES, SD, and RNG). Computations follow the equations described in Section 4.5.2. The resulting reconstruction matrices were compared based on these FoMs. A few test targets for all considered NF values were analyzed as well.

9.2 Reconstruction NN

There have already been several attempts to solve the EIT reconstruction problem using NNs. In this thesis a convolutional neural network (CNN) LeNet based approach based on work done by Tan et al.[67] in 2019 was utilized. It performed very well on the 2D cases presented in the article and its possible extension to 3D was inspected here.

9.3 Training data for reconstruction NN

Training data for the NN were generated using simulations with electrode set 2 and the respective I-M pattern selected in Section 13.4. Firstly, an enlarged target grid with a total of 3,971 targets each 1 cm in diameter was created for inhomogenous simulations. In this grid, targets overlapped by half of their diameter for denser oxygenator coverage. Target conductivity was randomly varied around the standard value based on a normal distribution $\mathcal{N}(0, \frac{\sigma_{target}}{10})$, where σ_{target} represents the standard target conductivity. A second group of training data consisted of noise-only simulations that were used to provide the NN with a negative control. Noise-only measurements were created as simulations on a homogeneous environment with normal random noise of a $\mathcal{N}(0, \frac{\sigma_{back}}{100})$ distribution, where σ_{back} represents background conductivity. Simulated voltage measurements for both groups were augmented with 15 dB SNR noise. Overall, 3,971 inhomogenous simulations and 3,971 noise simulations were created for training.

CNNs rely on the relationships between information from points spatially close to each other. To satisfy this spacial request, a measurement mapping function (`generateNNinputMapping`) was implemented. It converts 208 measurements to a 2D grid with a size of 16 × 13. In each row only measurements containing a specified electrode number are utilized. I chose a system where row number 1 contains only measurements with electrode number 1 being utilized as an injecting or measuring electrode. Row number n then contains only those measurements in which electrode number n is utilized as injecting or measuring. Relative voltage differences between homogeneous and inhomogenous cases resulting from 208 measurement simulations were used as input pixel values. This is done, because the selected I-M pattern contains 56 different injection pairs with different numbers of respective measuring pairs. Hence, it is not possible to create a matrix with each injecting pair measurements in one row.

As mentioned in Section 9.1, a 20 × 20 × 10 cubic voxel grid was used for reconstruction. Targets used for training were mapped to the respective voxels of this grid as the NN output. To emulate the desired image approach in GREIT a transition zone was created around voxels belonging to targets by filtering the image using a 3D Gaussian kernel with a standard deviation for all axes of $\sigma_{x,y,z} = 1$. The resulting NN output data vector contains ones for voxels that belong to the targets, values in range $[0, 1]$ in close proximity to the target and zeros elsewhere. These values can also represent probabilities of thrombus presence in voxels. This is utilized by a softmax layer of the NN, which converts these values to probabilities for the final output.

9.4 NN architecture

The used NN consists of layers with parameters described in Table 9.2. For a simpler orientation, the following labels were used: S ... stride, K ... filter size (only K × K filters were used), nF ... number of filters, P ... padding. Two convolution layers together with max pooling layers were used, as well as two FC layers. ReLU and leaky ReLU activation functions were used for better learning and a softmax layer was placed at the output to map NN output values to thrombus probabilities for individual voxels.

Layer #	Layer type	Layer parameters
1	input layer	accepts 16 × 13 input measurements
2	convolution layer	S=1, K=3, nF=32, padding=1
3	leaky ReLU layer	activation layer
4	max pooling layer	K = 2
5	convolution layer	S=1, K=3, nF=64, padding=1
6	leaky ReLU layer	activation layer
7	max pooling layer	K = 2
8	dropout layer	prevention of overfitting
9	FC layer	3200 neurons
10	ReLU	activation layer
11	FC layer	4000 neurons (output size)
12	softmax layer	conversion to probabilities
13	regression layer	comparison with ground truth values

Table 9.2: Overview of layers for the reconstruction NN.

9.5 NN training

Input data were randomly divided into three parts to form training, validation and test datasets. 80 percent of the data was used for training and 10 percent for either validation or tests. MATLAB's `trainNetwork` function was used to train a network with parameters given in Table 9.3. A stochastic gradient descent with momentum and a gradually decreasing learning rate of an initial value of 1×10^{-3} was selected as a solver. The regularization of NN parameters was included as well as a regularization factor of 1×10^{-6}. Validation checks were performed regularly to prevent overfitting to the training dataset. Overall, 300 training epochs were completed.

Unfortunately, the network wasn't able to converge during learning and the

Parameter	Value
Optimizer	Stochastic gradient descent with momentum
MiniBatchSize	128
MaxEpochs	300
InitialLearnRate	1×10^{-3}
LearnRateSchedule	piecewise
LearnRateDropFactor	0.1
LearnRateDropPeriod	40
L2Regularization	1×10^{-6}
Shuffle	every-epoch

Table 9.3: Parameters of the NN optimizing electrode positions.

reconstruction problem couldn't be solved reasonably.

Chapter 10

Thrombus detection and characterization

A rough reconstruction was successfully performed using the GREIT reconstruction algorithm, which gave an approximate idea whether any thrombi are present in the oxygenator. In this section the most important outcome of this thesis for clinical practice is discussed. It is thrombus detection and characterization. Several classifiers were implemented with the aim of thrombus detection and thrombosis severity assessment.

10.1 Detecting thrombus presence

The most fundamental question is whether any thrombi are deposited in the oxygenator. This detection was implemented for both the measured voltages and reconstructed images. Firstly, the possibility of thrombus detection based on measured voltages was inspected. Two types of classifiers were tested for this task. A support vector machine (SVM) classifier was the first choice. In this classifier, a radial basis function (RBF) kernel was used to better represent the nonlinear nature of the EIT measurements. Data standardization was performed on the input. The second choice of classifier was a NN with FC layers and one classification neuron. Next, the possibility of thrombus detection based on reconstructed images was inspected. Only an NN approach was selected in this case because of the more complex nature of the problem. Parameters described in Table 10.1 were used for the training of all the NNs. Input data were randomly divided into three parts to form training, validation and test datasets. 80 percent of the data was used for training and 10 percent for either validation or tests.

Parameter	Value
Optimizer	Stochastic gradient descent with momentum
MiniBatchSize	128
MaxEpochs	100
InitialLearnRate	1×10^{-3}
LearnRateSchedule	piecewise
LearnRateDropFactor	0.1
LearnRateDropPeriod	60
L2Regularization	1×10^{-6}
Shuffle	every-epoch

Table 10.1: Parameters for the thrombus detection NNs.

10.1.1 Training data for thrombus presence classifiers based on voltage measurements

Training data were generated using simulations with electrode set 2 and the I-M pattern selected in Section 13.4. The standard enlarged target grid with 3,971 targets, each 1 cm in diameter, was used for inhomogenous simulations. One target only was used for each inhomogenous simulation to test the classifier for the basic case of one thrombus presence. Target conductivity was randomly varied around the standard value based on a normal distribution of $\mathcal{N}(0, \frac{\sigma_{target}}{10})$, where σ_{target} represents the standard target conductivity. A second group of training data consisted of noise-only simulations as a negative control. Noise-only measurements were created as simulations on a homogeneous environment with normal random noise with a distribution of $\mathcal{N}(0, \frac{\sigma_{back}}{100})$, where σ_{back} represents background conductivity. Simulated voltage measurements for both groups were augmented with 15 dB SNR noise. Overall, 3,971 inhomogenous simulations and 3,971 noise simulations were created for training. Relative voltage difference data were used as NN input.

10.1.2 NN architecture for thrombus presence classification based on voltage measurements

The NN has an input layer accepting measured voltages in the form of a 208-element vector. It further consists of two FC inner layers paired with a ReLU activation function. The output of the NN is composed of a FC layer with two neurons and a softmax layer. This arrangement enables classification into two groups – thrombi present × thrombi missing. The entire network scheme is described in Table 10.2.

10.1.3 Training data for thrombus presence classifier based on reconstructed images

Training data for the classifier based on reconstructed images stem from the previously mentioned grid of 600 targets with 1 cm in diameter spanning the entire oxygenator volume. Target conductivities were varied in the same fashion as described in Section 10.1.1. Absolute voltage difference data were reconstructed using the GREIT reconstruction matrix corresponding to NF = 1 described in Section 9.1.

Layer #	Layer type	Layer parameters
1	input layer	accepts vector of 208 input measurements
2	FC layer	200 neurons
3	ReLU layer	activation layer
4	FC layer	100 neurons
5	ReLU layer	activation layer
6	FC layer	2 neurons corresponding to two classes
7	softmax layer	conversion to probabilities
8	classification layer	classifies to more probable class

Table 10.2: Overview of layers for a thrombus detection NN based on voltage measurements.

The output of this reconstruction is a vector with 4,000 reconstructed voxels which is directly used as an input to the NN. Overall, 600 training samples of noisy inhomogenous simulations and 600 training samples of noise-only simulations were utilized.

10.1.4 NN architecture for thrombus presence classification based on reconstructed images

The NN has an input layer accepting the mentioned vector with 4,000 reconstructed voxels. It also utilizes three FC inner layers paired with a leaky ReLU activation function. The output of the NN is composed of a FC layer with two neurons and a softmax layer. The architecture is based on the NN detecting thrombus based on voltage measurements. One inner layer is added to compensate the increased number of input elements. The entire network scheme is described in Table 10.3.

Layer #	Layer type	Layer parameters
1	input layer	accepts 4000 reconstructed voxel values
2	FC layer	400 neurons
3	ReLU layer	activation layer
4	FC layer	200 neurons
5	ReLU layer	activation layer
6	FC layer	100 neurons
7	ReLU layer	activation layer
8	FC layer	2 neurons corresponding to two classes
9	softmax layer	conversion to probabilities
10	classification layer	classifies to more probable class

Table 10.3: Overview of layers for a thrombus detection NN based on reconstructed images.

10.2 Assessing thrombosis severity

To assess thrombosis severity, a metric (η) was designed. It is computed as the ratio of overall thrombus volume to oxygenator volume. This reflects the fact that an increase in oxygenator thrombosis comes with big risks for patients. The greater the volume occupied by thrombi, the worse the gas exchange and the greater the pressure drop over the oxygenator. Two NNs were used to assess the value of η. The first NN works with voltage differences and the second with reconstructed images as inputs. Ten classes were created according to Table 10.4 to obtain η values.

Class #	η value range
1	$[0, 0.1]$
2	$(0.1, 0.2]$
3	$(0.2, 0.3]$
4	$(0.3, 0.4]$
5	$(0.4, 0.5]$
6	$(0.5, 0.6]$
7	$(0.6, 0.7]$
8	$(0.7, 0.8]$
9	$(0.8, 0.9]$
10	$(0.9, 1]$

Table 10.4: Values of η and the respective classes.

10.2.1 Training data for the thrombosis severity classifier based on voltage measurements

Training data were generated using simulations with electrode set 2 and the respective I-M pattern selected in Section 13.4. The mentioned target grid with 600 targets, each 1 cm in diameter, was used for inhomogenous simulations. Different levels of clotting severity were simulated by varying the number of randomly chosen targets. The amount of targets spanned between 1 and 600. The total thrombus volume for each simulation was computed by summing the volume of finite elements making up the thrombi. Only data for groups 1 to 4 were generated, because a higher thrombus presence isn't realistic. The representation of η groups in training data was skewed by noise-only simulations that also belong to group 1. There were also less samples for group 4. Target conductivity for a single training target distribution was randomly varied around the standard value based on a normal distribution $\mathcal{N}(0, \frac{\sigma_{target}}{10})$, where σ_{target} represents the standard target conductivity. A second group of training data consisted of noise-only simulations. Noise-only measurements were created as simulations on a homogeneous environment with normal random noise with a distribution of $\mathcal{N}(0, \frac{\sigma_{back}}{100})$, where σ_{back} represents background conductivity. Simulated voltage measurements for both groups were augmented with 15 dB SNR noise. Overall, 1,200 measurements with different numbers of targets present were simulated.

10.2.2 NN architecture for the thrombosis severity classifier based on voltage measurements

The architecture stems from the NN used for thrombus presence detection based on voltage measurements described in Section 10.1.2. The only changes being different amounts of neurons used in each FC layer in the hidden architecture. 600 neurons are used in FC layer # 1 instead of 200 and 200 neurons are used in FC layer # 2 instead of 100. The output layer contains four neurons enabling the network to classify the inputs into four groups based on presumed thrombosis severity.

10.2.3 Training data for the thrombosis severity classifier based on reconstructed images

Training data for the thrombosis severity classifier based on reconstructed images stem from the training data described in Section 10.2.1. Absolute voltage difference data were reconstructed using the GREIT reconstruction matrix corresponding to NF = 1 described in Section 9.1. The output of this reconstruction is a vector of 4,000 reconstructed voxels which is directly used as an input of the NN.

10.2.4 NN architecture for the thrombosis severity classifier based on reconstructed images

The architecture stems from the NN used for the thrombus presence detection based on reconstructed images described in Section 10.1.4. The only changes in hidden architecture being the different amounts of neurons used in each FC layer. 500 neurons are used in FC layer # 1 instead of 400 and 300 neurons are used in FC layer # 2 instead of 200. The output layer contains four neurons enabling the network to classify each case into one of four groups according to presumed thrombosis severity.

Chapter 11

Real mock experiments

To demonstrate the functionality of the proposed approaches, a set of measurements was conducted on the mock oxygenator stationed at the institute for Medical Information Technology (MedIT) at RWTH Aachen (Aachen, Germany). My colleagues at the institute conducted this experiment with the Sciospec device described in Section 6.1.1. Data was measured using 16 electrodes placed at locations according to electrode set 2 (depicted in Figure 7.1b) and the optimized I-M pattern with 208 measurements described in Section 13.4. The electrodes were connected to the device via crocodile clips and extension cords. A saline solution (0.9 % NaCl) was used as the background medium. The separation grid was included in both the homogeneous and inhomogenous measurements. An AC current with a frequency of 750 kHz with an amplitude of 10 mA was used for all injections. A balloon of an approximately spherical shape filled with air was used for inhomogenous measurements. For the sake of following computations, the diameter of the target was set to 1 cm. Inhomogenous measurements for three different balloon positions were conducted. Approximate balloon target positions together with respective labels are depicted in Figure 11.1. The experimental setup is depicted in Figure 11.2.

11.1 Thrombus reconstruction and detection

Every measurement was repeated five times in close time proximity and averaged in order to lower the influence of noise. The device is able to measure complex impedance, but only the real part was considered. After the measurements were acquired, reconstruction using the GREIT reconstruction matrix was conducted. The same reconstruction matrix corresponding to NF = 1 as described in Section 9.1 was used. Absolute voltage differences were reconstructed. Afterwards, the measured and reconstructed data were fed to classification NNs to find out whether the thrombi were detected. Thrombosis severity was tested as well by the respective NN. Already trained NNs were utilized. Complete description of architectures and parameters of the NNs is described in section 10.

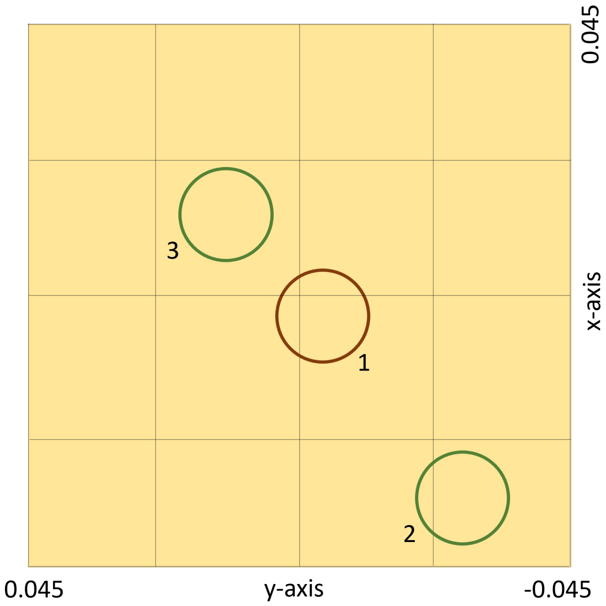

Figure 11.1: Approximate balloon target positions with respective labels, the green color represents a position in the top part of the oxygenator over the separation grid and the brown color position in the bottom part under the separation grid.

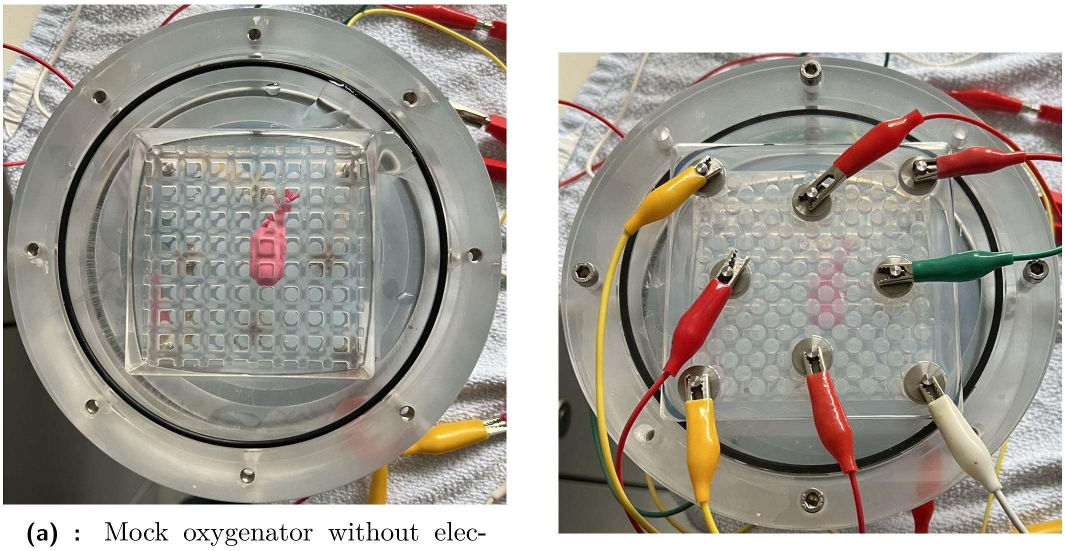

(a) : Mock oxygenator without electrodes, target inserted under the separation grid.

(b) : Mock oxygenator with electrodes present and target inserted.

Figure 11.2: Experiment setup for real mock measurements at the institute.

Part III

Results and discussion

In this section, results and corresponding discussions will be presented. The structure is organized similarly to the Materials and Methods section (Chapter II) for easier orientation. Only representative examples of results are depicted in this section, the rest can be found in Appendix A.

Chapter 12

Preliminary experiments

The preliminary experiments in this thesis were aimed at uncovering whether changes in electrode positions, I-M patterns, and target conductivity translated to statistically significant differences in measurements. This helped to conclude which parameters to include in the subsequent optimization steps.

12.1 Selecting the most sensitive measurements

Firstly, all 1560 measurements from the designed I-M pattern (depicted in figures 7.2 and 7.3) for the four predefined electrode sets (depicted in Figure 7.1) were sorted. The goal was to attempt to uncover useful measurements and forego the amplification of present noise caused by including too many measurements. The sorting was conducted based on three parameters - the L1- and L2-norms of measurement sensitivity vectors, and their parallelotope volumes. Even with Jacobian scaling, it was not possible to choose more than approximately 180 measurements based on the parallelotope volume. The rank of the Jacobian is approximately 104 in all cases, which leads to the small singular values of any further sensitivity vectors (e.g. 10^{-14}) and the resulting inability of the computer to numerically express the parallelotope volume.

Simulations for measurement selection were conducted on all four electrode sets and three sets of 104 measurements. Each set was selected based on one of the three described sorting methods. This resulted in 12 unique combinations of electrode sets and sorting methods. The three selection methods were compared based on simulated data.

Firstly, selections were compared in terms of utilized electrodes and their spatial arrangement. Observations were made about the frequency of individual electrode use and the most commonly utilised electrode pairs. Of particular interest was the fact whether the most sensitive measurements include inter-plane or intra-plane injecting and measuring pairs. Measurements were therefore divided into five groups according to the spatial arrangement of the participating pairs.

- Group 1: Inter-plane injection and measurement
- Group 2: Inter-plane injection, intra-plane measurement

- Group 3: Intra-plane injection, inter-plane measurement
- Group 4: Intra-plane injection and measurement in one plane
- Group 5: Intra-plane injection and measurement in opposite planes

It appears from the statistical analysis on electrode set 1 (depicted in Figure 12.1) that parallelotope volume maximization leads to the most homogenous incidence of both the electrodes used and spatial arrangement groups present. This confirms the hypothesis that this approach leads to the homogenous coverage of the entire oxygenator volume. For both L1-norm and L2-norm-based measurement selection, one of the spatial arrangement groups is typically not represented at all. Bottom electrodes are also more heavily utilized than top electrodes adding to the asymmetry of these measurements.

The possible generalization of the findings based on electrode set 1 was confirmed by the other three electrode sets, where similar patterns were uncovered. Based on these four models, the following can be induced: parallelotope volume maximization results in all electrodes being evenly utilized and all spatial arrangement groups being represented. L1- and L2-norm maximization leads to uneven electrode utilization with the prioritization of bottom electrodes. L2-norm maximization consistently avoids group 4 measurements, which tend to have a lower overall sensitivity. This is caused by the need for the penetration of the oxygenator volume together with the separation grid by the injecting current, which allows it to influence the measuring pair on the other side of oxygenator. Measurement group distributions for both parallelotope volume maximization and L2-norm maximization are stable over all four electrode placement options. Parallelotope volume maximization results in a large proportion of group 1 measurements and low proportion of group 5 measurements. On the other hand, L2-norm maximization leads to a large proportion of group 3 measurements. This is caused by the spatial proximity of injecting and measuring pairs, because the elements surrounding electrodes have the greatest sensitivity. Statistics for electrode sets 2, 3 and 4 are depicted in Appendix A.

In addition to the analysis of electrode use and electrode arrangement, the sensitivity distribution of finite elements was explored over the four proposed electrode placements according to the following procedure. Absolute values of Jacobian sensitivity vectors were summed over selected measurements for all finite elements in the oxygenator excluding the ones belonging to the separation grid. Distributions were compared both in spatial and value domains. It appears from the analysis depicted in figures 12.2 and 12.3 that a few general conclusions, independent of electrode configuration, can be drawn. Median sensitivity is highest for L1-norm selected measurements, followed by L2-norm selected measurements. This reflects the fact that L1-norm is more robust and isn't influenced that much by outliers as L2-norm. Parallelotope volume selected measurements lead to sensitivities with the smallest interquartile range and smallest maximum value. This confirms that parallelotope volume maximization leads to more homogenous measurements. Other interesting observation is that, according to their respective distributions, both L1-norm and L2-norm maximizations result in measurements sensitive to conductivity changes more or less in the entire oxygenator volume. This is quite surprising because there is no consideration of spatial homogeneity in norm maximization. The spatial distributions of sensitivities for electrode set 1 (depicted in Figure 12.4) show that the most sensitive elements are placed around electrodes, especially the ones not in the corners, which was expected. Other sensitive areas are around the separation grid near the borders of the oxygenator. These observations are valid for all other electrode sets, whose distributions are depicted in Appendix A. The analysis revealed also shortcomings of parallelotope volume maximization based measurement selection. Although it has the most homogenous coverage of the three selection methods, its sensitivity to conductivity changes is overall smaller then that of measurements chosen based on the L1 and L2 norms.

The final analysis over the 104 selected measurements for each selection method includes voltage differences. A homogenous simulation was followed by measurements on a few targets, chosen to illustrate differences among measurements. Each target (with a diameter of 1 cm) was placed in a different oxygenator quadrant and in various distances from the oxygenator center. Simulations were carried out on these targets and distributions of the measured voltages were observed. Both absolute and relative voltage differences between inhomogenous and homogenous cases were considered, the relative voltage difference being more indicative of change significance. In this section only two targets are depicted for electrode set 1 in Figure 12.5b for clarity. The rest of the data may be found in Appendix A. The boxplots in Figure 12.5b reveal that the L2-norm-selected measurements consistently provide the highest third quartile value in terms of relative voltage change. This contrast with the highest third quartile value in terms of absolute voltage change which is held by L1-norm-selected measurements. This can be caused by the fact that homogenous measurements for L2-norm based measurements are of a significantly lower magnitude. Furthermore, it is positive that even targets near the center of the oxygenator cause relative voltage changes of at least a few percent. However, the change is usually much bigger elsewhere, even hundreds of percent. The absolute measured voltage change oscillates around tenths of mV for all measurements, which should be detectable in real-life measurements.

From the results of this preliminary study, we can see the influence of measurements on important quantities tied to the EIT method. Measurements affect not only absolute and relative voltage differences, but also the distribution of used electrodes and the sensitivity of elements inside the measured volume. What's more, these parameters are affected differently based on the method, chosen for measurement selection. This points toward the fact that there is still work to be done in the area of measurement selection optimization and that the selection is worth optimizing.

12.2 Influence of electrode positions

To determine the significance of the influence of electrode positions on the measured signal, the four predefined electrode sets (depicted in Figure 7.1) were compared using all 1560 measurements from the designed I-M pattern (depicted in figures 7.2 and 7.3). Firstly, a sensitivity analysis was conducted. Absolute values of Jacobian matrix elements were summed both per measurement (over rows) and per finite element (over columns). The left part of Figure 12.6 shows the absolute Jacobian values summed over measurements, sorted for each electrode set separately. It appears that the least sensitive measurements are of similar magnitude for all electrode sets, whereas for the most sensitive measurements, magnitude differs. The most sensitive measurements overall belong to electrode set 4. Measurements of an average sensitivity also differ among the electrode sets. The right part of Figure 12.6 compares absolute values of Jacobian elements summed over all finite elements which are again sorted for each electrode set separately. All electrode sets have similar values corresponding to both the least and most sensitive element. Elements with average sensitivities differ among the electrode sets. Figure 12.7 shows the detail of these distributions. The interquartile range is similar for all electrode sets with the median differing slightly. However, the difference in mean ranks is statistically significant between all pairs of groups according to the conducted nonparametric Kruskal-Wallis test (distributions are not normal) and consequent multiple comparison of mean ranks. The results of the Kruskal-Wallis test were evaluated at a significance level of $\alpha = 0.05$ and gave a test value of $\mathcal{X}^2(3) = 28366.06$ and p-value of $p < 10^{-12}$. This points to the fact that there are statistically significant differences among mean ranks of the studied groups. Multiple comparison results are depicted in detail in Table 12.1. They show statistically significant differences between all pairs of electrode sets.

Electrode set #1	Electrode set #2	significant difference	p-value
1	2	yes	$<10 \times 10^{-12}$
1	3	yes	$<10 \times 10^{-12}$
1	4	yes	$<10 \times 10^{-12}$
2	3	yes	$<10 \times 10^{-12}$
2	4	yes	7.8×10^{-5}
3	4	yes	$<10 \times 10^{-12}$

Table 12.1: Results of multiple comparison following the Kruskal-Wallis test on finite element sensitivity differences among electrode sets.

A voltage difference analysis for the different electrode positions was carried out next. Both absolute and relative voltage differences between homogenous and inhomogenous cases were explored for all 600 targets in the defined grid. Voltage differences were summed either over targets or over measurements for all electrode sets. A similar interquartile range and slightly differing medians were observed for all electrode sets in both cases. Boxplots are depicted in the upper row of Figure 12.8. Relative voltage differences were captured as 95th percentile values again both per target and per measurement (depicted in the bottom row of Figure 12.8). This percentile was chosen to eliminate high outlier values. The biggest outlier among electrode sets is electrode set 4 in the relative voltage difference taken per target. Its mean relative voltage as well as interquartile range is visibly very different. Statistical analysis was performed to reveal other significant differences as well. Because of the non-normal distributions of the data, a nonparametric Kruskal-Wallis test was used again. Results for absolute voltage differences per target were assessed at a significance level of $\alpha = 0.05$ and gave a test value of $\mathcal{X}^2(3) = 1203.43$ and a p-value of $p < 10^{-12}$. A consequent multiple comparison showed differences in mean ranks for several group pairs (details are depicted in Table 12.2). The result of relative voltage differences per measurement were also assessed at a significance level of α

= 0.05 and gave test values: $\mathcal{X}^2(3) = 11.75, p = 0.0083$. The consequent multiple comparison showed only one pair of significantly differing electrode sets - electrode set 2 and electrode set 3. Details of multiple comparison are depicted in Table 12.3).

Electrode set #1	Electrode set #2	significant difference	p-value
1	2	no	3.74×10^{-1}
1	3	yes	2.77×10^{-7}
1	4	yes	$<10 \times 10^{-12}$
2	3	yes	6.67×10^{-4}
2	4	yes	$<10 \times 10^{-12}$
3	4	yes	$<10 \times 10^{-12}$

Table 12.2: Results of multiple comparison following the Kruskal-Wallis test on relative voltage difference per target among electrode sets.

Electrode set #1	Electrode set #2	significant difference	p-value
1	2	no	8.94×10^{-1}
1	3	no	6.21×10^{-2}
1	4	no	1
2	3	yes	7.65×10^{-3}
2	4	no	8.86×10^{-1}
3	4	no	6.52×10^{-2}

Table 12.3: Results of multiple comparison following the Kruskal-Wallis test on relative voltage difference per measurement among electrode sets.

The analysis of electrode set influence on Jacobian and voltage measurements showed that the most significant changes are Jacobian-related. Only one pair differed significantly in terms of relative voltage difference. However, the spatial distribution of finite elements and voltage differences wasn't considered. This means that relevant spatial-related differences might be hidden.

12.3 Influence of I-M pattern

The following experiments were conducted using different I-M patterns to uncover the effect on final measurements. Injection-measurement patterns were chosen based on typical I-M nomenclature and compared to the custom I-M created for this thesis. To get a good scope of I-M patterns a representative digest was made, I-M patterns 1-1, 2-4, 3-3, 3-5, 4-5, 6-4, 7-7 and 8-8 were chosen. Firstly, sensitivity analysis on these I-M patterns was done. Absolute values of Jacobian matrix elements were summed, this time only per finite element. Different I-M patterns contained different number of measurements, so all sums for the finite elements of each pattern were scaled by the respective number of measurements corresponding to this pattern. Distributions of this sensitivity parameter of all selected I-M patterns are depicted in Figure 12.9. Statistical analysis was again carried out using the Kruskal-Wallis test (data distributions are not normal) to find significant differences in mean ranks.

The result of the Kruskal-Wallis test was assessed on a significance level of $\alpha = 0.05$: $\mathcal{X}^2(8) = 1.25 \times 10^6, p < 10^{-12}$. A subsequent multiple comparison showed differences in mean ranks between all pairs of I-M patterns. Results of the multiple comparison are not included because of numerous combinations.

Voltage difference analysis for the I-M patterns was carried out next. Both absolute and relative voltage differences between homogenous and inhomogenous cases were explored for all 600 targets in the defined grid. Voltage differences were summed over either targets or measurements for all electrode sets and scaled by the number of measurements for respective I-M patterns. Differing interquartile ranges and medians were observed for different I-M patterns in both cases (for absolute and relative voltage differences). Boxplots are depicted in the upper row of Figure 12.10. Relative voltage differences were captured as 95th percentile values again both per target and measurement (depicted in the bottom row of Figure 12.10). Statistical analysis was performed to confirm difference significance. Because of non-normal distributions a nonparametric Kruskal-Wallis test was again used. Result for relative voltage difference per target are reported for a significance level of $\alpha = 0.05$: $\mathcal{X}^2(8) = 4028.66, p < 10^{-12}$. A subsequent multiple comparison showed differences in mean ranks for most of the I-M pattern pairs. Result for relative voltage difference per measurement were assessed at a significance level of $\alpha = 0.05$: $\mathcal{X}^2(8) = 274.42, p < 10^{-12}$. A subsequent multiple comparison showed differences in mean ranks for the majority of the I-M pattern pairs. Results of multiple comparisons are not included because of numerous combinations.

Analysis revealed that some patterns would bring much more information with the measurements than others. The patterns 1-1 and 8-8 were recognized not to be suitable for this spatial electrode arrangement, whereas patterns 2-4, 3-5, 7-7 and 6-4 were recognized as much better. The pattern 2-4 was evaluated as by far the best for relative voltage difference per target and measurement. This pattern includes both inter-plane and intra-plane measurements, which supports the original measurements proposed in designed I-M pattern. Sensitivity analysis values for the designed pattern are lower compared to other patterns because there are numerous measurements of low sensitivity included. When divided by 1560 measurements, the average value is really low.

12.4 Influence of target conductivity

The final set of preliminary experiments was aimed at voltage difference analysis for different target conductivity values. Electrode set 1 with designed I-M pattern were used. Both absolute and relative voltage differences between homogenous and inhomogenous cases were explored for all 600 targets in the defined grid. The conductivites of the targets were varied between 10^{-6} and 10^3 multiples of background conductivity (6.62×10^{-1} S.m^{-1}). Voltage differences were summed over either targets or measurements. Boxplots are depicted in the upper row of Figure 12.11. Relative voltage differences were captured as 95th percentile values again both per target and measurement (depicted in the bottom row of Figure 12.11). From the boxplots, we can see that two distinct groups have seemingly formed for all analyzed parameters. The first group consists of targets with a conductivity value lower than that of the background. The actual conductivity value within this group doesn't appear to have much of an effect on the observed features. On the other hand, for target conductivities higher than that of the background, increasing target conductivity values leads to the increase in medians and a general shift of the distribution towards higher voltage values. However, differences seem to vanish with further increased conductivity as well. Statistical analysis was performed to confirm significance of differences between the given measurements. Because of the non-normal distributions of data, the nonparametric Kruskal-Wallis test was again utilized. The results of absolute voltage difference per target are given at a significance level of $\alpha = 0.05$ and resulting test variables are: $\mathcal{X}^2(9) = 2450.46, p < 10^{-12}$. A subsequent multiple comparison showed differences in mean ranks between the group of less conductive targets and more conductive targets. There is not a statistically significant difference within the lower conductivity group. The result for the relative voltage difference per measurement were assessed at a significance level of $\alpha = 0.05$ with the following outcome: $\mathcal{X}^2(9) = 7365.92, p < 10^{-12}$. The subsequent multiple comparison provided the same result as in the previous case. Results of multiple comparisons are not included because of numerous combinations. A saturation property of the EIT was demonstrated on the targets especially with low conductivity values. Nevertheless, This will not be a problem for future thrombus reconstruction because the conductivity difference doesn't span multiple orders of magnitude.

From this preliminary analysis, we can see that all parameters have a statistically significant effect on both the measured voltages and Jacobian values. An analysis of different measurement selection methods revealed significant influence on electrode utilization and spatial relations of injecting and measuring pairs. Therefore, the optimization of electrode positions and I-M patterns has the potential to bring more information from the measurement and lead to a better image reconstruction as opposed to an unoptimized source of voltage measurements. Additionally, the effect of target conductivity on the measurements was also shown. This information is important mainly when dealing with specific thrombi types, but will not be discussed in more detail in this work. An important consideration for future development is the size limit for thrombi detectability which wasn't covered here.

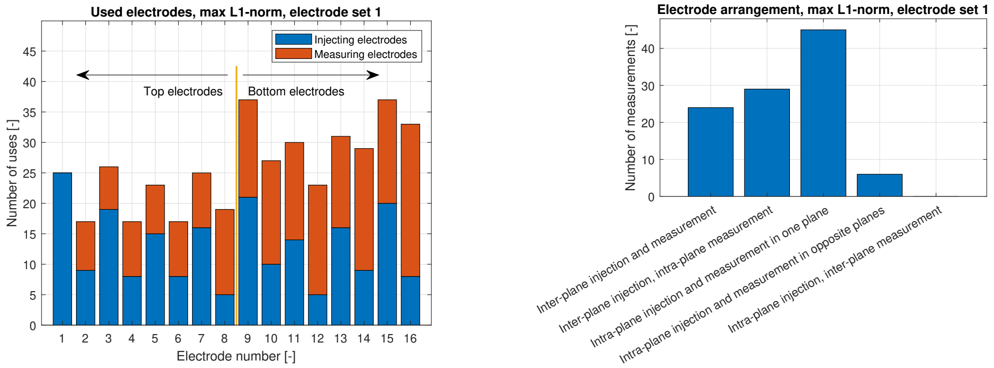

(a) : Statistics of electrode usage for electrode set 1 and max L1-norm measurements.

(b) : Electrode arrangement statistics for electrode set 1 and max L1-norm measurements.

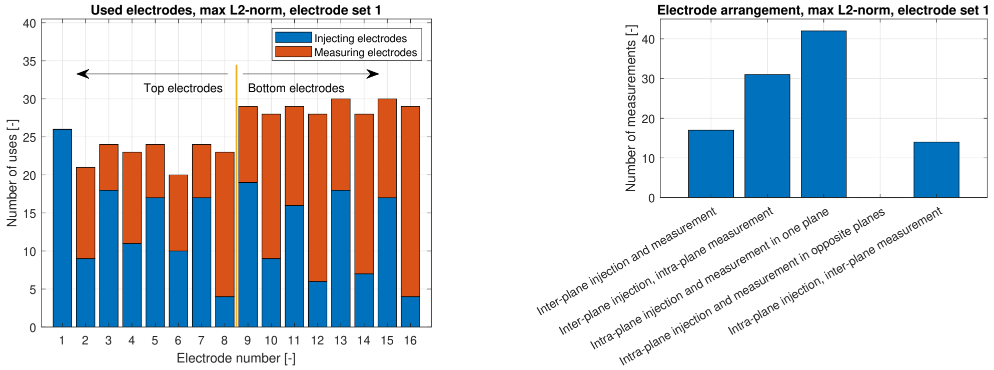

(c) : Statistics of electrode usage for electrode set 1 and max L2-norm measurements.

(d) : Electrode arrangement statistics for electrode set 1 and max L2-norm measurements.

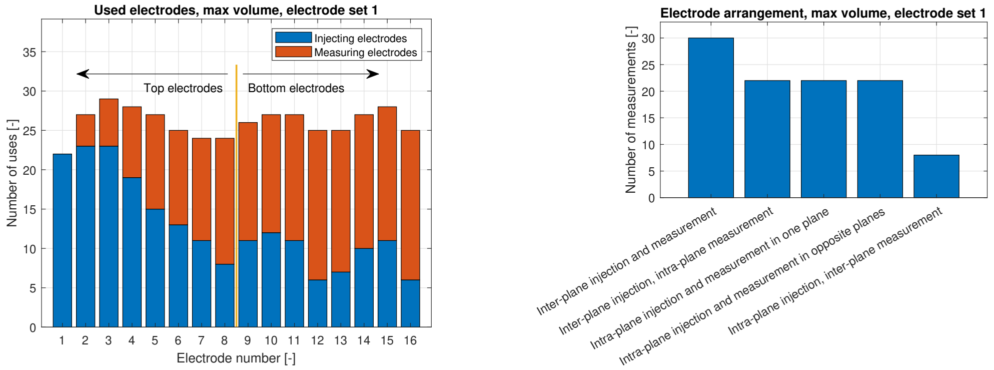

(e) : Statistics of electrode usage for electrode set 1 and max parallelotope volume measurements.

(f) : Electrode arrangement statistics for electrode set 1 and max parallelotope volume measurements.

Figure 12.1: Electrode utilization analysis for measurement selection, electrode set 1.

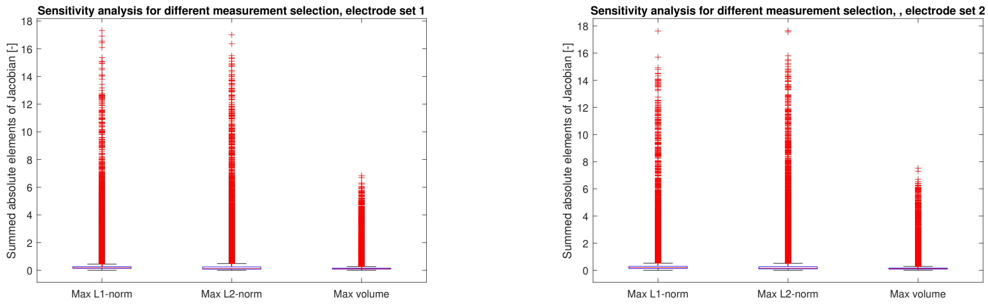

(a) : Finite elements sensitivity analysis for electrode set 1

(b) : Finite elements sensitivity analysis for electrode set 2

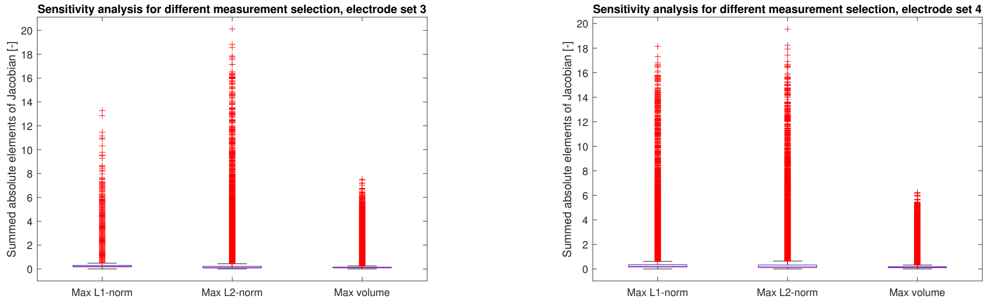

(c) : Finite elements sensitivity analysis for electrode set 3

(d) : Finite elements sensitivity analysis for electrode set 4

Figure 12.2: Finite elements sensitivity analysis

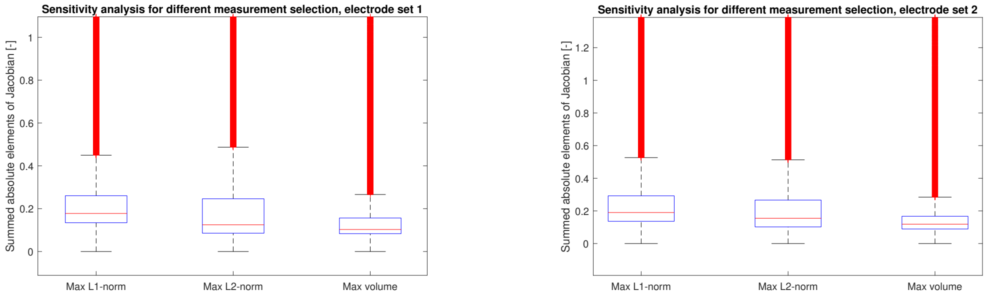

(a) : Finite elements sensitivity analysis for electrode set 1 – detail.

(b) : Finite elements sensitivity analysis for electrode set 2 – detail.

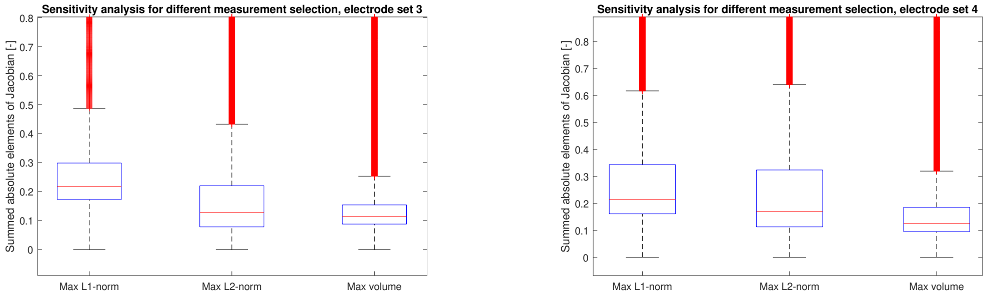

(c) : Finite elements sensitivity analysis for electrode set 3 – detail.

(d) : Finite elements sensitivity analysis for electrode set 4 – detail.

Figure 12.3: Finite elements sensitivity analysis – detail.

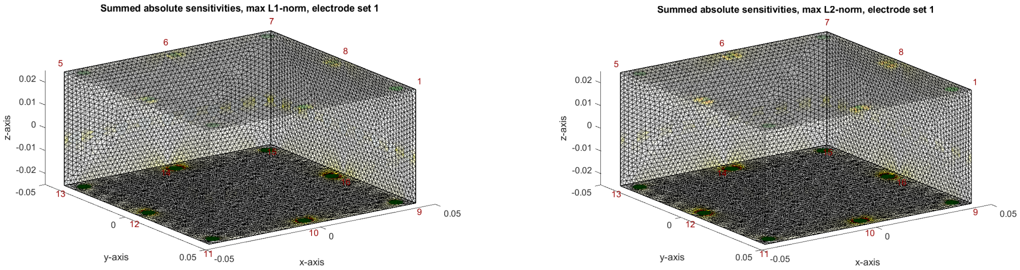

(a) : Spatial finite element sensitivity distribution, max L1-norm, electrode set 1,

(b) : Spatial finite element sensitivity distribution, max L2-norm, electrode set 1.

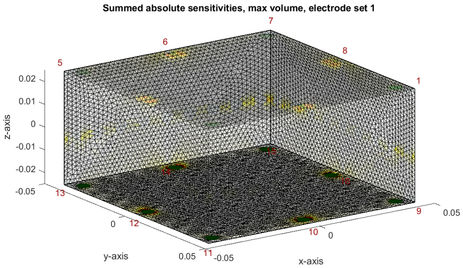

(c) : Spatial finite element sensitivity distribution, max volume, electrode set 1.

Figure 12.4: Spatial finite element sensitivity distribution for electrode set 1, where sensitivity hot spots are depicted in yellow.

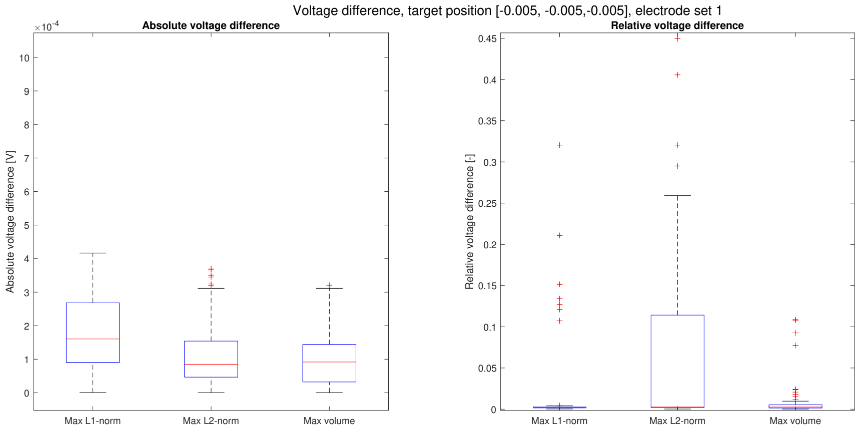

(a) : Absolute and relative voltage differences, target near oxygenator center, electrode set 1

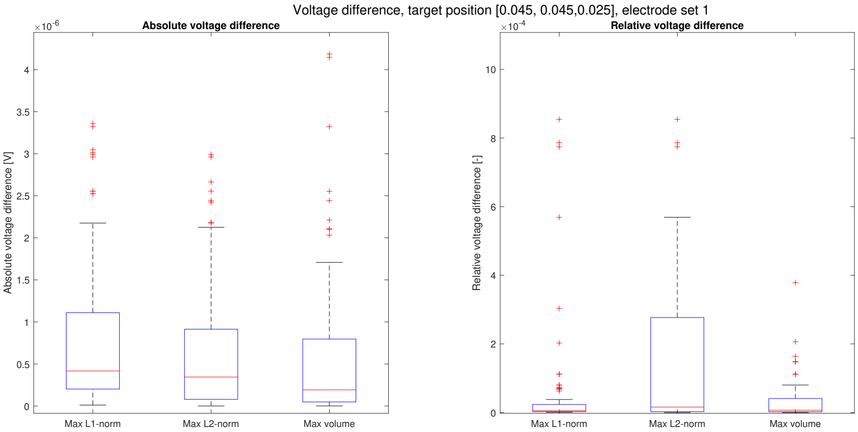

(b) : Absolute and relative voltage differences, target in the corner, electrode set 1

Figure 12.5: Absolute and relative voltage differences for two targets, electrode set 1

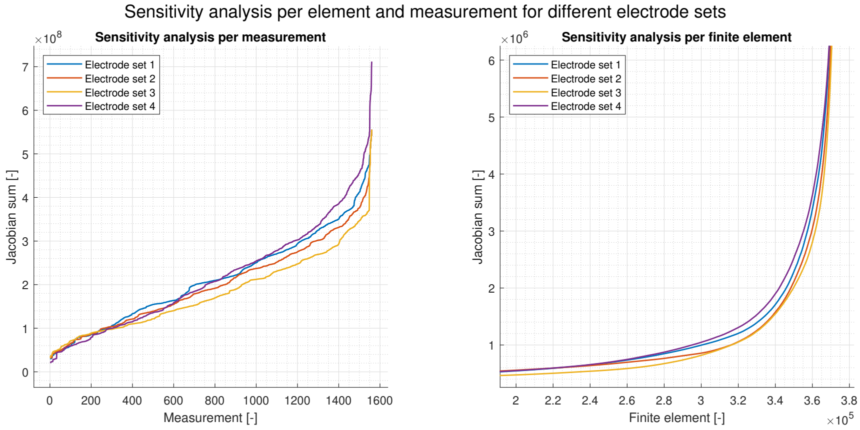

Figure 12.6: Sensitivity analysis of different the electrode sets.

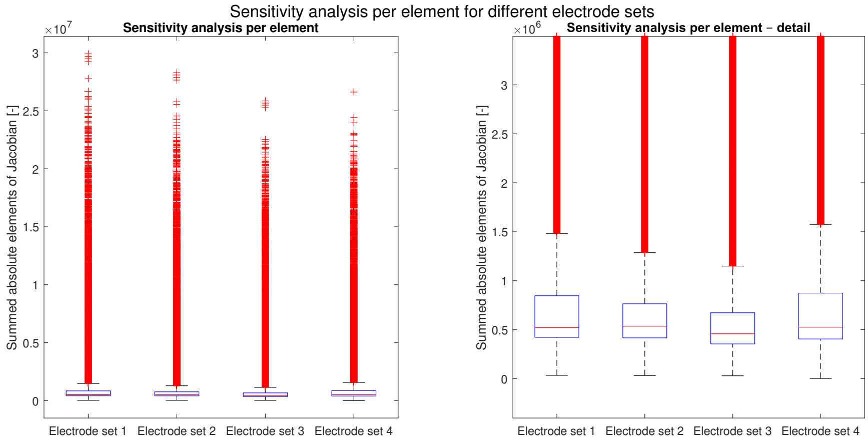

Figure 12.7: Boxplot sensitivity analysis of the different electrode sets.

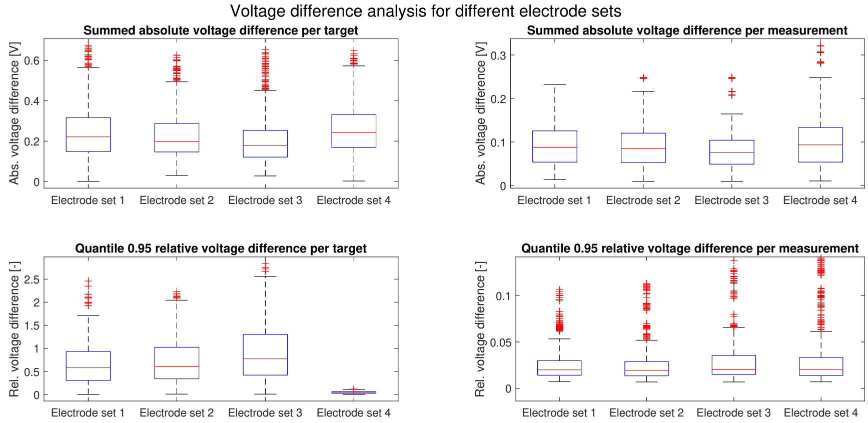

Figure 12.8: Voltage difference analysis for different electrode sets

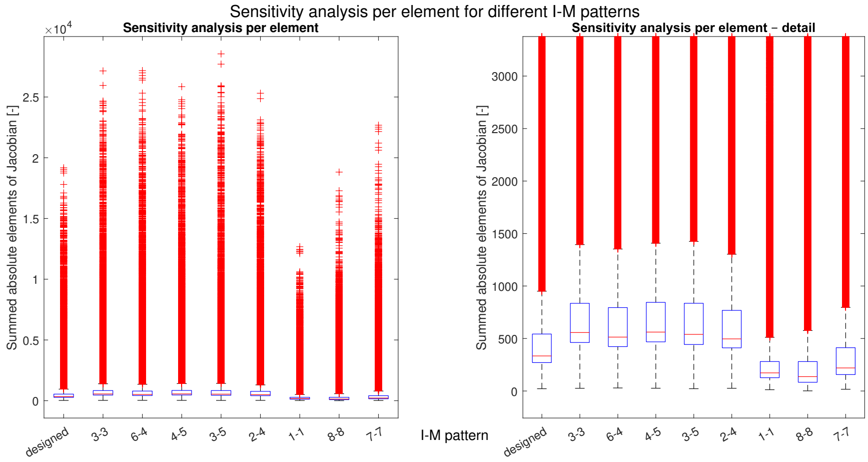

Figure 12.9: Sensitivity analysis of different I-M patterns.

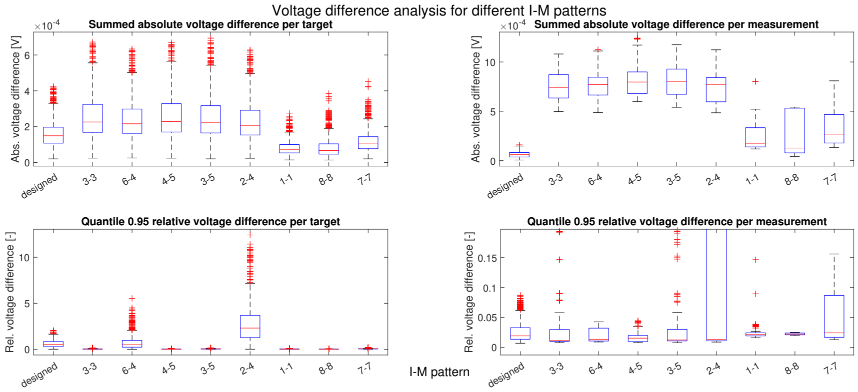

Figure 12.10: Voltage difference analysis for different I-M patterns

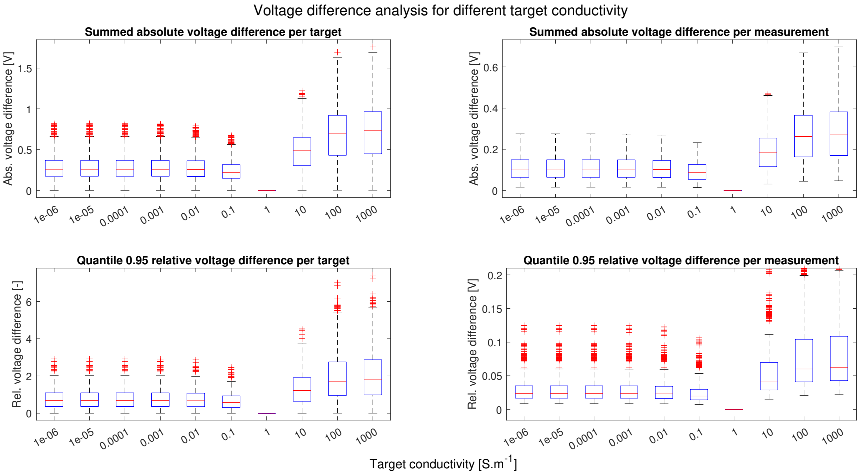

Figure 12.11: Voltage difference analysis for target conductivity.

Chapter 13

Electrode positions and I-M pattern optimization

Due to the results of the preliminary experiments, the optimization of electrode positions and the I-M pattern was attempted next. For the 2918 unique electrode sets, 208 measurements from the designed I-M pattern and twelve sets of six targets, 35016 input factor combinations were at disposal for NN training. 80 percent of the input data were used for the real NN training, 10 percent for training validation and the final 10 percent for the testing of the NN.

13.1 Training data for NN

In the article by Smyl and Liu (2020),[66] NN input features consist of the reconstruction difference and condition number of the Hessian matrix. These two input parameters were chosen as an indicator of EIT data quality, and a measure of ill-conditioning and reconstruction quality. In my thesis, reconstruction was excluded from position optimization on purpose, therefore it wasn't considered as a possible input in this case. Additionally, because of the huge number of finite elements of the Hessian matrix H (which is computed from the Jacobian J according to Equation (13.1)), even the computation of the Hessian alone isn't feasible memory-wise. It would contain more than 100 billion elements and would take up tens of gigabytes alone.

$$H = J^T J \tag{13.1}$$

Therefore, alternative features had to be designed as replacements. Features described in Section 8.1 were considered. Three more features were created by combining the listed features. The Jacobian condition number ξ_J, defined as a ratio of maximum and minimum Jacobian singular values σ_k and calculated according to equation (13.2) was used as an ill-conditioning metric. The next two features were designed to capture the homogenous coverage of the oxygenator volume by the electrodes. The first is defined as ψ_J - the ratio of the median of the Jacobian sensitivity vector L1-norm and the minimum L1-norm of the Jacobian sensitivity vectors according to Equation (13.3). The other was denoted as $\psi_{\Delta V}$ and is calculated as the ratio of the median relative voltage difference ΔV to the minimum relative voltage difference ΔV according to Equation (13.4). The added features are summarized in Table 13.1.

$$\xi_J = \frac{\max \sigma_k}{\min \sigma_k} \tag{13.2}$$

$$\psi_J = \frac{\mathrm{median} J}{\min J} \tag{13.3}$$

$$\psi_{\Delta V} = \frac{\mathrm{median}\Delta \mathrm{V}}{\min \Delta \mathrm{V}} \tag{13.4}$$

#	Feature	Description
16	median J / min J	measure of Jacobian homogeneity
17	max σ_k / min σ_k	Jacobian condition number
18	median ΔV / min ΔV	measure of measurement homogeneity

Table 13.1: Features designed for electrode position optimization using NN training.

With these features added to the list, 18 features in total were available for selection. A correlation analysis was performed on the full NN input dataset to discover redundant features. All features were scaled using respective maximum feature values which resulted in a range of $[0, 1]$ for all features as all the values of these features are positive. Pearson correlation was then performed over these features. A visualized correlation matrix is depicted in Figure 13.1. Below, I would like to point out some of the interesting results originating from this analysis. They show mainly a divergence between ΔV and the Jacobian.

- Mean ΔV is weakly correlated to medianΔV ($\mathrm{r} = 8.84 \times 10^{-2}$), whereas mean J is strongly correlated to median J (r = 0.93).
- Mean ΔV is strongly correlated to max ΔV (r = 0.99), whereas mean J is weakly correlated to max J (r = -0.11).
- Both $\mathrm{Q}_1(\Delta \mathrm{V})$ and $\mathrm{Q}_3(\Delta \mathrm{V})$ are strongly correlated to medianΔV (r=0.76). This applies to the Jacobian as well: $\mathrm{Q}_1(\mathrm{J})$ and $\mathrm{Q}_3(\mathrm{J})$ are strongly correlated to median J (r=0.75, r=0.90).
- Rank(J) is strongly negatively correlated to most of the features tied to the Jacobian (e.g. r = -0.61 for mean J and r = -0.65 for min J).
- Median J / min J is strongly negatively correlated to max J (r = -0.87).

After performing correlation analysis, five different feature sets were selected for NN training. They are described in Table 13.2.

13.2 NN training

Five different NNs were trained based on feature sets 1 to 5. NN labels correspond to feature set numbers listed above. All networks finished 100 epochs without overfitting to training data. Validation loss and validation root-mean-square error (RMSE) decreased steadily with training loss and training RMSE, respectively. On

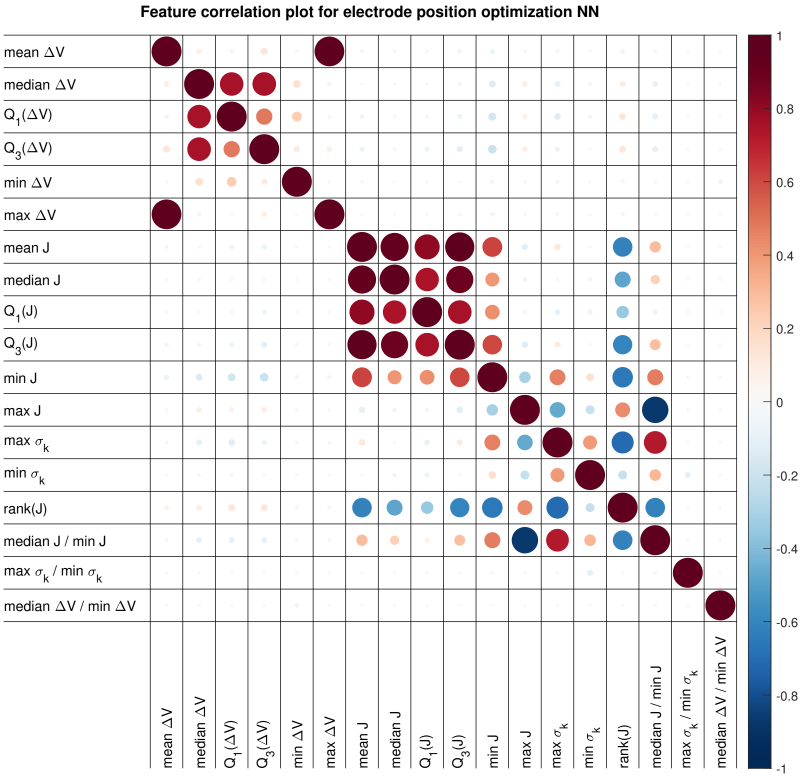

Figure 13.1: A visualization of the correlation matrix for electrode position optimization NN input features, the red color represents a positive correlation and blue a negative correlation; the sizes of circles are proportional to absolute correlation coefficients.

the other hand, neither the loss, nor error showed any change in the last epochs. The training can therefore be considered sufficient without being over-trained. Training statistics for NN 1 and NN 2 are depicted in Figure 13.2. The rest of the statistics are depicted in Appendix A.

13.3 Optimized electrode positions

To get the optimized electrode positions, scaled input feature values theoretically corresponding to an optimal electrode set were used as an input vector to the NN. Afterwards, a forward pass was carried out and optimal electrode set coordinates were read from NN output. For this analysis, a set of optimal values for all features had to be created (values are summarized in Table 13.3). Optimal values were chosen based on generated input data with an emphasis on maximum values being close to minimum values in order to increase homogeneity.

The output coordinates from the NN output were assigned to nearest plausible positions using the created `findNearestPlausibleElectrodePosition` function.

Set	Features contained in the set	Remarks
1	all features	redundancy wasn't considered
2	mean ΔV, median ΔV, min ΔV, median J, max J, min σ_k, max σ_k / min σ_k, median ΔV / min ΔV	all non-redundant features
3	mean ΔV, median ΔV, min ΔV, median ΔV / min ΔV	non-redundant voltage related features
4	median J, max J, min σ_k, max σ_k / min σ_k	non-redundant Jacobian related features
5	median J / min J, max σ_k / min σ_k, median ΔV / min ΔV	homogeneity and ill-conditioning related features

Table 13.2: Selected feature sets for electrode position optimization NN.

Electrode sets computed as the forward pass of optimal feature sets 4 and 5 with electrodes placed at plausible positions are depicted in Figure 13.3. The remaining electrode sets are depicted in Appendix A.

Resulting electrode positions are sometimes slightly outside of the oxygenator and mostly not directly on either of the electrode planes. The final plausible positions for two electrodes may sometimes end up in the same place, which is the reason for the lower number of visible electrodes in some figures. A comparison of the resulting electrode sets revealed that the network trained on "homogeneity" feature set 5 actually lead to the most homogenous electrode placement, which is highly similar in both planes. However, it doesn't cover oxygenator edges and corners. This is probably caused by the fact that there is no training penalisation for the case when these regions aren't covered. Other electrode sets show significant grouping of electrodes with electrode arrangement differing in both planes of the oxygenator. Training electrode sets corresponding to individual input feature values closest to the optimal feature values were explored to attempt to discern the reasons behind this. It was observed that some of these training electrode sets show similar arrangements, which then probably translates to grouping in the resulting electrode sets. The electrode set for the best value of the rank(J) feature is depicted in Figure 13.4 and the electrode set for the best value of the median J feature is depicted in Figure 13.5. The figures for the remaining features are depicted in Appendix A.

13.4 Final electrode positions and I-M pattern selection

The electrode sets given by the previous NN optimization aren't suitable to cover regions with a high likelihood of thrombus occurrence. Therefore, it was decided that the final selection of the electrode set and I-M pattern will be made from the designed electrode sets. The analysis of NN output electrode sets shows that electrodes closer to the oxygenator center are advantageous and therefore electrode set 2 (depicted in 7.1b) and electrode set 3 (depicted in 7.1c) were selected as final candidates. Each electrode set was assigned measurements from the designed I-M

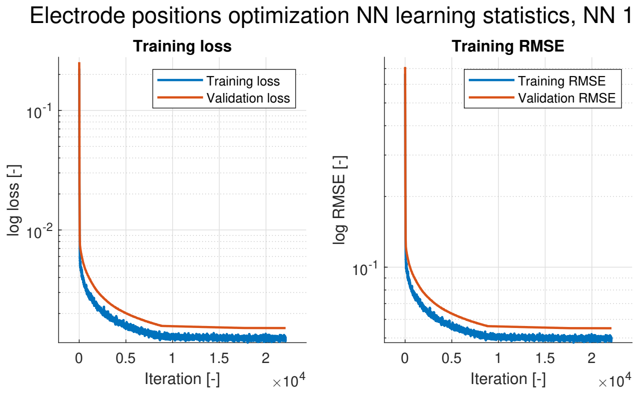

(a) : Training statistics for NN 1

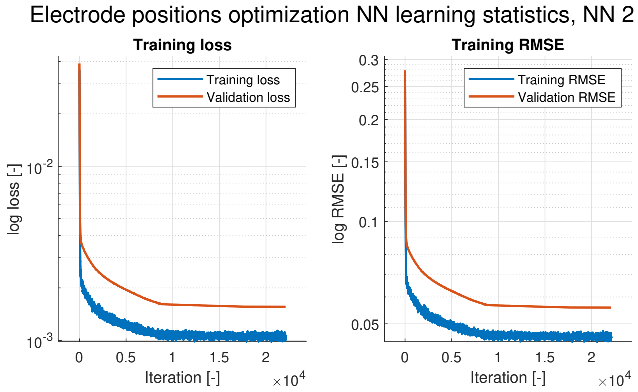

(b) : Training statistics for NN 2

Figure 13.2: Training statistics – training loss, training RMSE, validation loss and validation RMSE – for electrode position optimization NN 1 and NN 2

pattern based on a previously performed sensitivity vector analysis. Overall, 208 measurements were utilised, 104 measurements based on maximum parallelotope volume, 64 measurements based on maximum L1-norm and 40 measurements based on maximum L2-norm. Afterwards, Jacobian and voltage difference analysis was performed in order to choose between the electrode sets.

Distributions of absolute Jacobian values that reflect element sensitivities were compared first. Results are depicted in Figure 13.6. Electrode set 2 has a higher maximum sensitivity value and a bigger interquartile range with a higher Q_3 value. Next, absolute Jacobian values were summed over finite elements. For each finite element, the accumulated sensitivity was compared between the electrode sets. The result of this analysis is depicted in Figure 13.7. Electrode set 2 has more sensitivity across finite elements. Afterwards, 0.95 quantiles of both absolute and relative voltage differences were computed and compared for the two electrode sets. Results are depicted in Figure 13.8. In this analysis, electrode set 3 provided a greater voltage difference for both absolute and relative cases.

A final comparison was aimed at electrode utilization. Both electrode set 2 and 3 utilize bottom electrodes for measurements more than top electrodes. This

#	Feature	Optimal value
1	mean ΔV	1×10^{-1}
2	median ΔV	1×10^{-1}
3	$Q_1(\Delta V)$	1×10^{-2}
4	$Q_3(\Delta V)$	1.5×10^{-1}
5	min ΔV	1×10^{-3}
6	max ΔV	2
7	mean J	1×10^{6}
8	median J	1×10^{6}
9	$Q_1(J)$	5×10^{4}
10	$Q_3(J)$	1.5×10^{6}
11	min J	5×10^{3}
12	max J	1×10^{7}
13	max σ_k	10
14	min σ_k	1×10^{-1}
15	rank(J)	208
16	median J / min J	1
17	max σ_k / min σ_k	1
18	median ΔV / min ΔV	1

Table 13.3: Optimal feature values for electrode position optimization NN

effect is even more significant for electrode set 3. Both electrode sets utilize mostly measurements from groups 1, 2, and 3 (as described in Section 12.1). Electrode utilization statistics are depicted in figure 13.9.

Electrode set 2 with the respective I-M pattern was selected for future experiments because of better sensitivity and a more homogeneous utilization of electrodes. It will perform slightly worse in the center of the oxygenator, but slightly better around oxygenator edges, where thrombi are more often expected. The respective I-M pattern contains 56 different injecting pairs with number of measuring pairs in range from 1 to 11 for each injecting pair, a total of 208 measurements. Half of the chosen measurements stem from sensitivity vector parallelotope maximization, which brings the best possible homogenous coverage of all finite elements. The other half comes from maximization of L1 and L2 norms of sensitivity vectors. These measurements bring amplification of useful signal and mitigate noise influence.

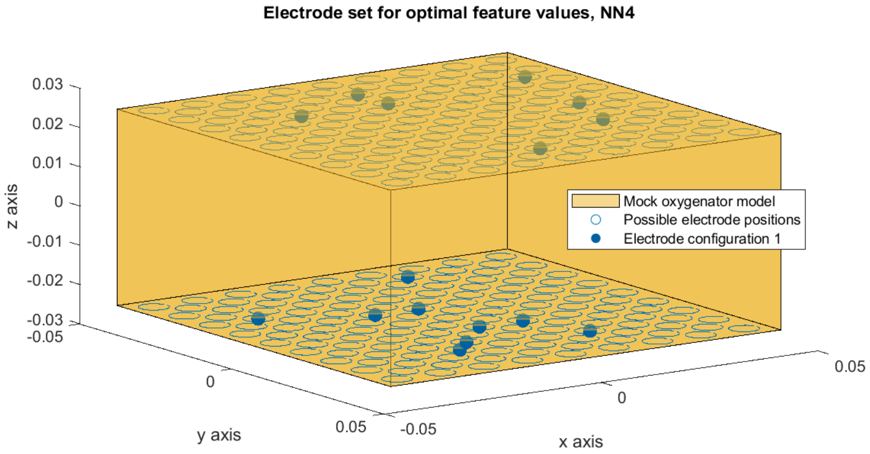

(a) : Electrode set for optimal feature set 4

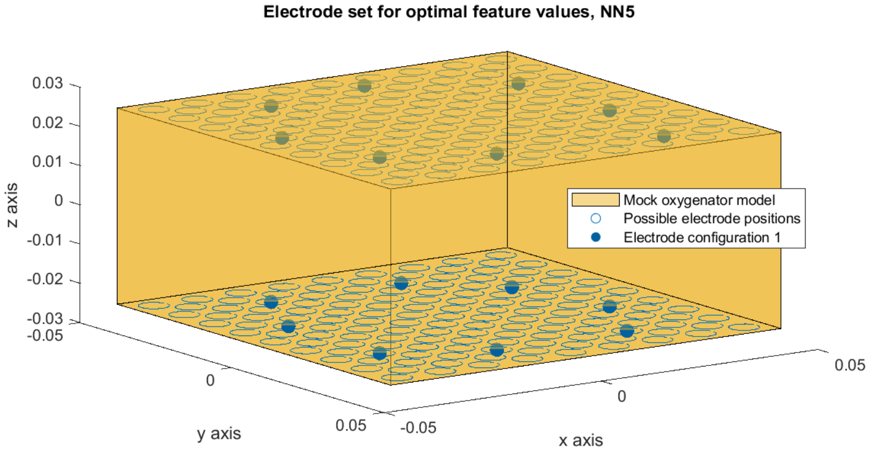

(b) : Electrode set for optimal feature set 5

Figure 13.3: Electrode sets computed as the forward pass of optimal feature sets 4 and 5 (electrode position optimization using a NN)

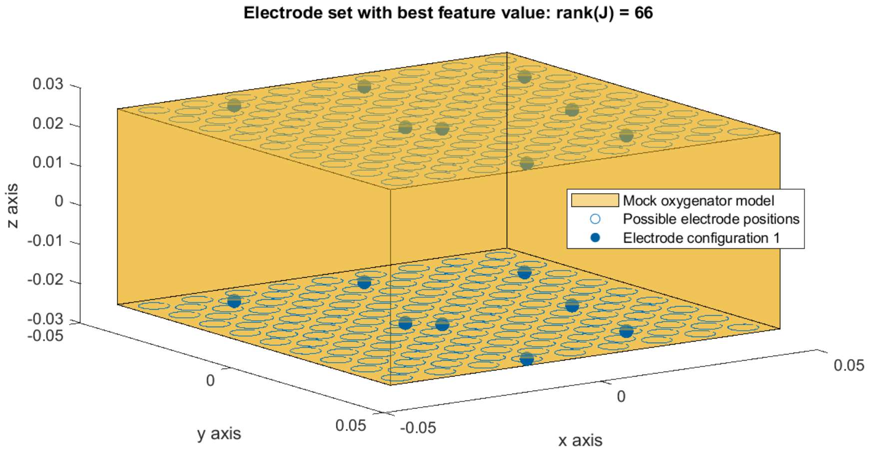

Figure 13.4: A training electrode set with a minimum difference between the computed rank(J) feature and the optimal feature value.

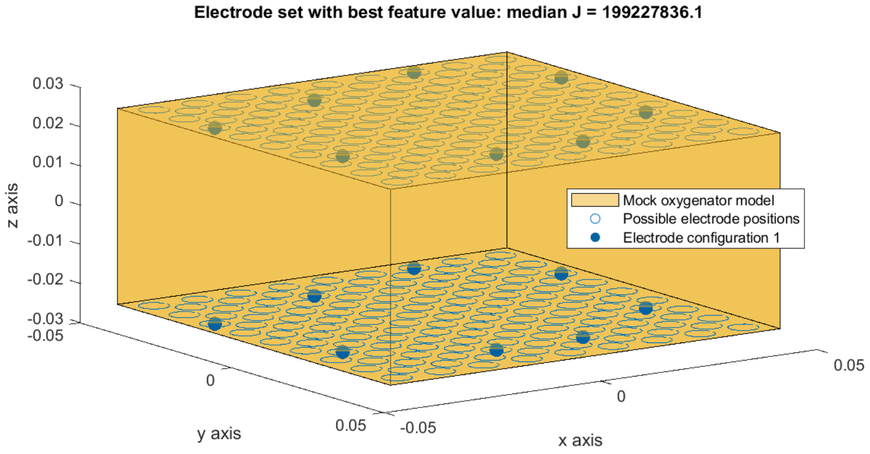

Figure 13.5: A training electrode set with a minimum difference between the computed median J feature and the optimal feature value.

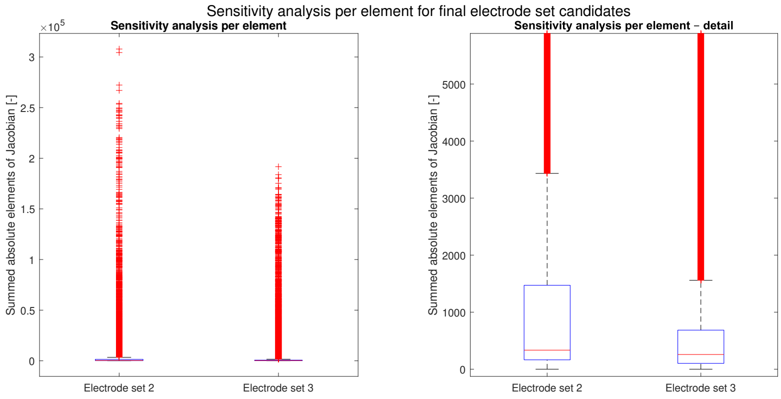

Figure 13.6: The comparison of absolute sensitivity distribution for electrode sets 2 and 3.

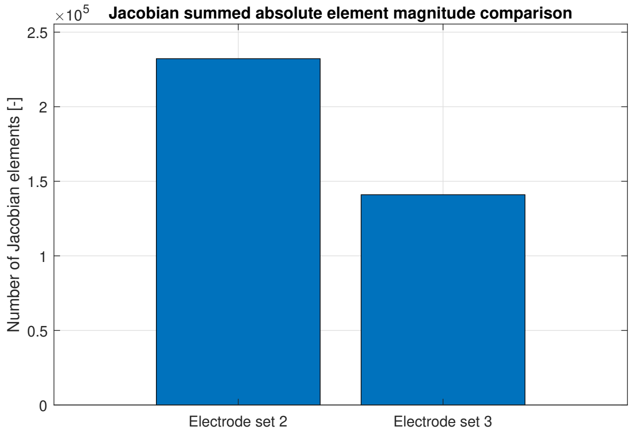

Figure 13.7: The comparison of accumulated absolute finite element sensitivities for electrode sets 2 and 3.

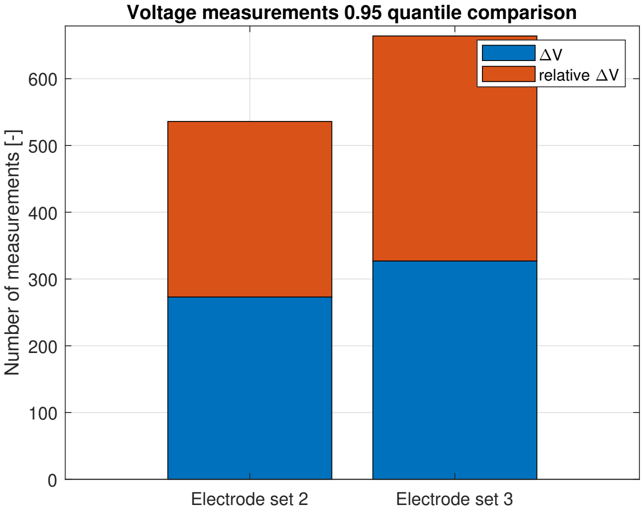

Figure 13.8: The comparison of 0.95 quantile of absolute (blue) and relative (red) voltage differences (ΔV) for electrode sets 2 and 3.

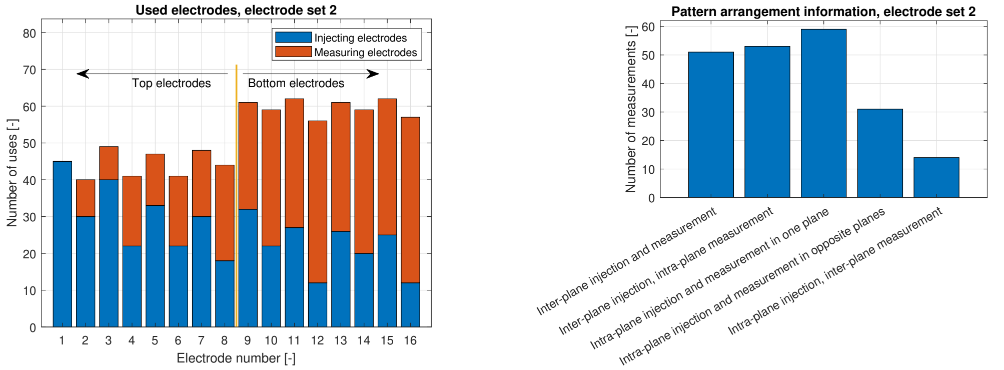

(a) : Statistics of electrode usage for electrode set 2.

(b) : Electrode arrangement statistics for electrode set 2.

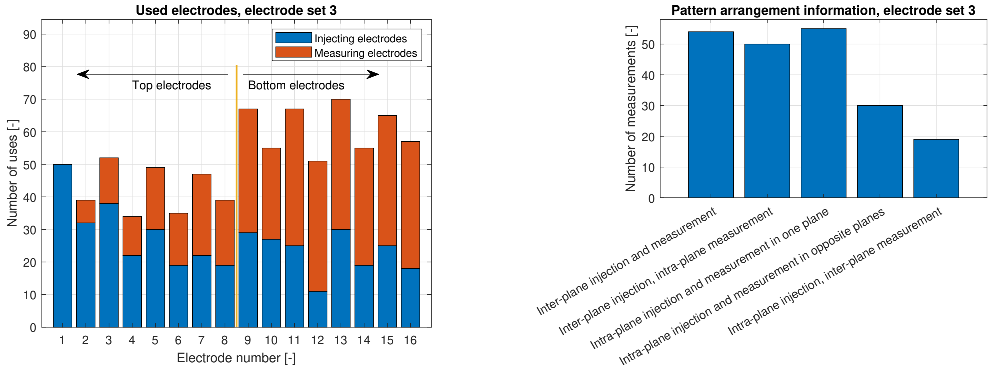

(c) : Statistics of electrode usage for electrode set 3.

(d) : Electrode arrangement statistics for electrode set 3.

Figure 13.9: Electrode utilization analysis, electrode set 2 and 3.

Chapter 14

Image reconstruction and processing

Based on the selected electrode set and the respective I-M pattern a GREIT reconstruction matrix was trained as well as a reconstruction NN.

14.1 GREIT reconstruction

The GREIT reconstruction matrix was trained on 6600 generated targets using the EIDORS `mk_GREIT_model` function. This function optimizes a weight value which scales noise importance in the process of reconstruction matrix computation to achieve the goal NF value. Three different GREIT reconstruction matrices were trained this way for an NF of 1, 2 and 3. The NF of 0.5, which is often mentioned in literature as the ideal value, couldn't be reached with any weight value.

The three generated GREIT matrices were compared based on FoM computed by the EIDORS `eval_GREIT_fig_merit` function. A boxplot analysis was conducted for each FoM metric separately. Results are depicted in Figure 14.1.

The boxplots reveal that the greater the NF value the greater the dispersion of the reconstruction. There are several reconstruction cases where the AR metric reaches negative values which is indicative of the reconstruction of training targets of a conductivity higher than that of the background to targets less conductive relative to background conductivity. The most significantly negative AR values appear for NF = 3, making it ill-disposed for reconstruction. The most compact distribution for both AR and RNG metrics were found for NF = 1. This compact property prevails in the PE, SD and RNG metrics as well.

Visual inspection was carried out on four targets with a diameter of 1 cm. Their center positions are marked in Table 14.1. Reconstructions for NF = 1 are depicted in Figure 14.2. Reconstructions for other values of NF are depicted in Appendix A. Targets that are close to the oxygenator walls are reconstructed far better than targets near the oxygenator center. However, there are still significant ringing artefacts of positive conductivity change present. Targets near the center are shifted much closer to the walls than in ground truth simulations and voxels signalizing lower conductivity regions are dispersed almost everywhere around the oxygenator. It was confirmed from the figures that the greater the NF the greater the dispersion of reconstruction, meaning voxels tied to target conductivity change were reconstructed to a wider area surroundings the target.

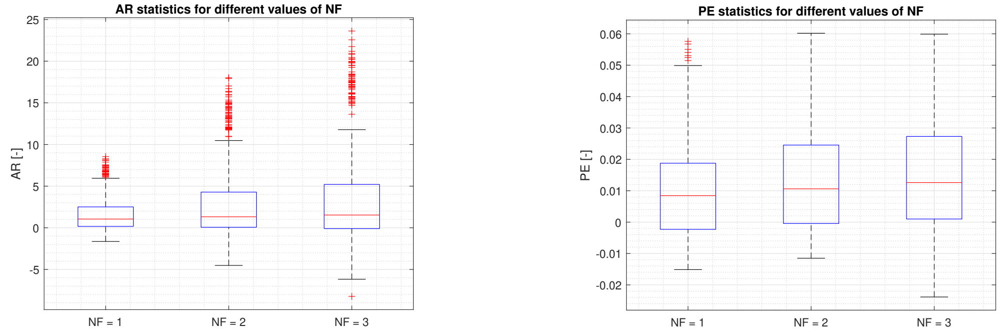

(a) : AR metric statistics.

(b) : PE metric statistics.

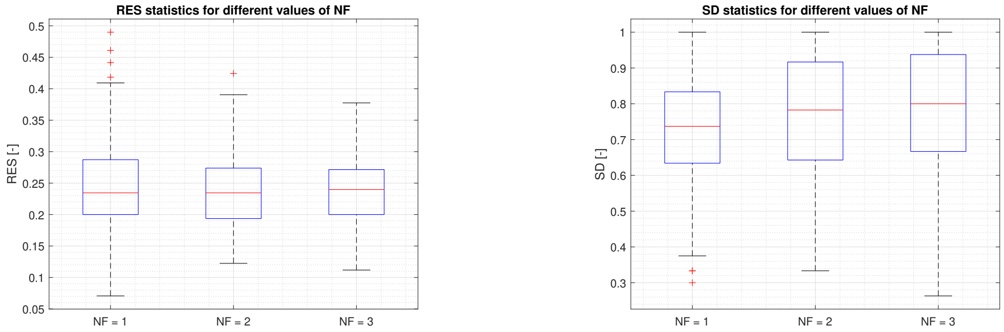

(c) : RES metric statistics.

(d) : SD metric statistics.

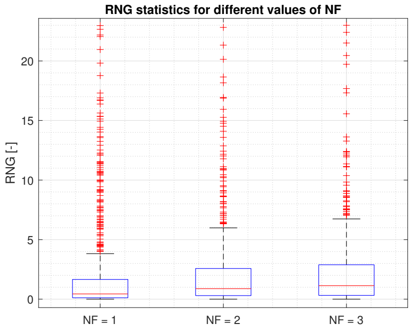

(e) : RNG metric statistics.

Figure 14.1: Comparison of FoM metrics for different GREIT reconstruction matrices corresponding to NF of 1, 2, and 3.

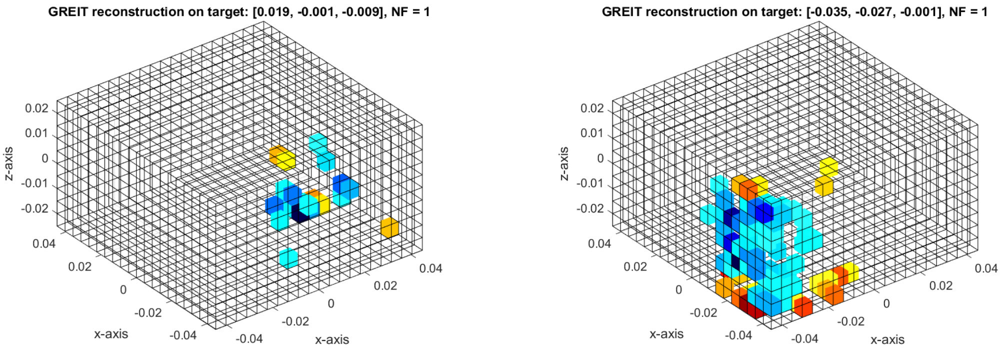

GREIT reconstruction on target: [0.019, -0.001, -0.009], NF = 1

GREIT reconstruction on target: [-0.035, -0.027, -0.001], NF = 1

(a) : Target # 1 reconstruction.

(b) : Target # 2 reconstruction.

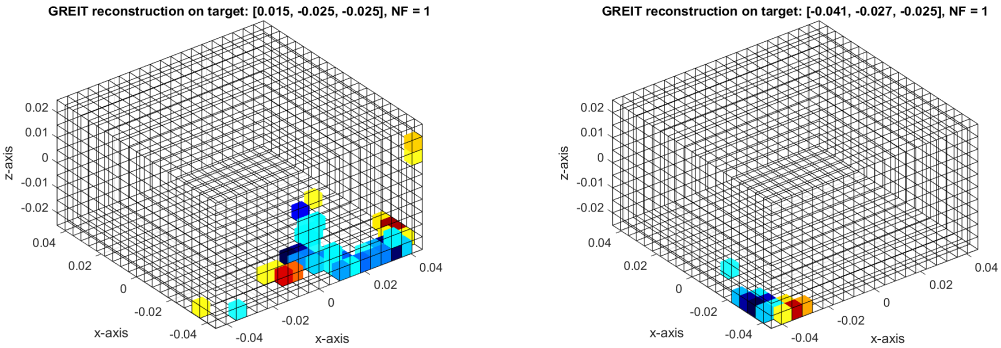

GREIT reconstruction on target: [0.015, -0.025, -0.025], NF = 1

GREIT reconstruction on target: [-0.041, -0.027, -0.025], NF = 1

(c) : Target # 3 reconstruction.

(d) : Target # 4 reconstruction.

Figure 14.2: GREIT reconstruction for NF = 1 and four different targets.

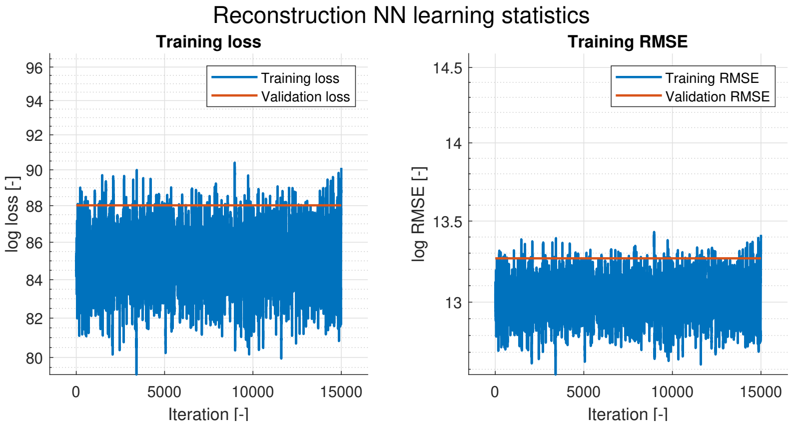

Figure 14.3: Training statistics – training loss, training RMSE, validation loss and validation RMSE – for reconstruction NN.

14.2 Reconstruction NN

The reconstruction NN was trained on 3,971 inhomogenous target simulations and 3,971 noise simulations. Relative voltage differences were used as NN inputs. Unfortunately, even after 300 epochs, learning wasn't successful and didn't converge. Both training loss and training RMSE remained approximately stable throughout the whole training process. The same applies also for validation loss and validation RMSE. Detailed training statistics are depicted in Figure 14.3.

Target #	Center position [x, y, z]
1	[1.9, -0.1, -0.9]
2	[-3.5, -2.7, -0.1]
3	[1.5, -2.5, -2.5]
4	[-4.1, -2.7, -2.5]

Table 14.1: GREIT test target positions in cm from oxygenator center.

Several modifications were performed both on NN architecture and learning parameters, but no improvement was observed. This means a successful LeNet application on 3D oxygenator reconstruction isn't too probable, or would need significant architecture changes and enhancements. There are several other NN architectures, e.g. U-Net, worth testing in the future. There is certainly significant potential for NNs to solve the reconstruction problem.

Chapter 15

Thrombus detection and characterization

Four different NNs were trained on respective training dataset. The main goal was to detect thrombus presence and thrombosis severity based on voltage measurements and reconstructed images. Training statistics for all cases are available in Appendix A. In all cases, the validation accuracy and loss decrease together with the training accuracy and loss which indicates that overfitting to training data didn't occur. This was confirmed on test data classification which resulted in a similar detection accuracy as for the validation data.

Accuracy over 94 % was achieved for test data on the thrombus-detection NN based on voltage measurements. The confusion matrix depicted in Figure 15.1 reveals 3.9 % of false negative cases of measurement classification. These correspond to thrombus being present in the oxygenator and not being detected, which would be very dangerous for patients. The number of false negatives should be mitigated in practice as much as possible. False positives were present in 1.3 % of cases. They would mean more work for the personnel to check the oxygenator, but wouldn't endanger the patient life.

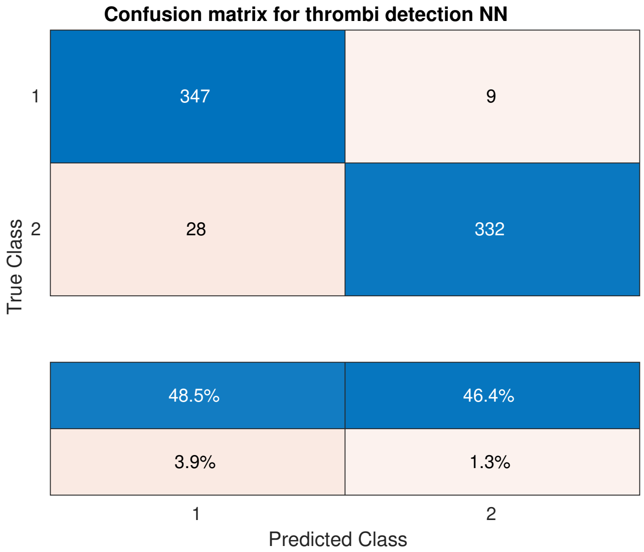

Figure 15.1: Confusion matrix for the thrombus-detection NN with voltage measurements as input data. Class #1 corresponds to thrombi not present and class #2 corresponds to thrombi present.

An accuracy over 70 % was achieved for test data on thrombi detection NN based on reconstructed images. The confusion matrix depicted in Figure 15.2 reveals

18.4 % of false negatives, which is unacceptable. This further confirms that the reconstruction is not good and provides far worse results for thrombus detection than the pure voltage measurements. False positives were present in 9.7 % of cases.

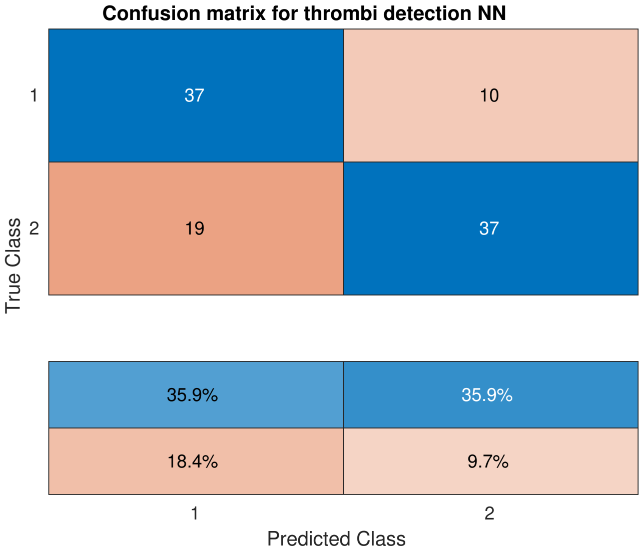

Figure 15.2: Confusion matrix for the thrombus-detection NN with reconstructed images as input data. Class #1 corresponds to thrombi not present and class #2 corresponds to thrombi present.

Over 89 % accuracy was achieved for test data on thrombosis severity classification NN based on voltage measurements. The confusion matrix depicted in Figure 15.3 reveals dangerous situations when thrombi volume is underestimated occurred in almost 8 % of cases. This leads to the underestimation of the thrombosis severity and may lead to critical situations. In almost 6 % of cases the thrombosis severity was overestimated.

Over 82 % accuracy was achieved for test data on thrombosis severity classification NN based on reconstructed images. The confusion matrix depicted in Figure 15.4 reveals dangerous situation when thrombi volume is underestimated in more than 6 % of cases. This is a surprisingly good result because the thrombus detection based on reconstructed images wasn't reliable at all (accuracy only ca. 70%). In more than 6 % of cases the thrombosis severity was overestimated, especially for thrombosis severity cases classified into group 2.

A better reconstruction algorithm may lead to better prediction capabilities of thrombus detection and thrombosis severity assessment models. However, the currently used GREIT reconstruction generally lead to worse classification results than when using measured voltages alone. The approach of detecting thrombi directly from voltage measurements seems to be the most promising, until an enhanced 3D reconstruction method is developed.

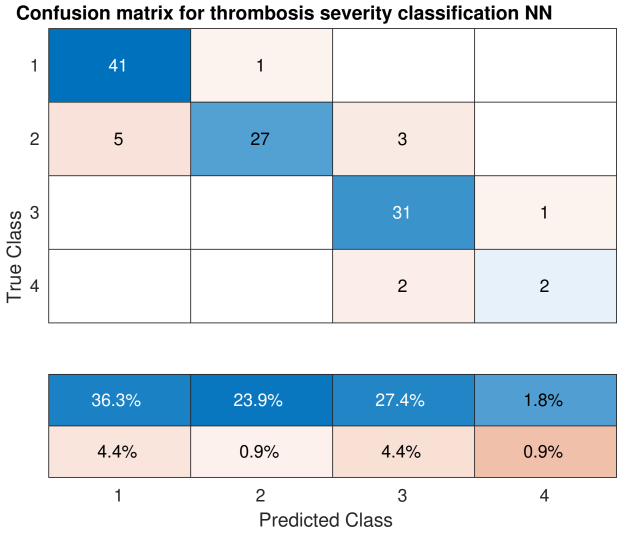

Confusion matrix for thrombosis severity classification NN

True Class	1	2	3	4
1	41	1		
2	5	27	3	
3			31	1
4			2	2

	1	2	3	4
	36.3%	23.9%	27.4%	1.8%
	4.4%	0.9%	4.4%	0.9%

Predicted Class

Figure 15.3: Confusion matrix for thrombosis severity classification NN with voltage measurements as input data. Class #1 corresponds to thrombi not present and class #2 corresponds to thrombi present.

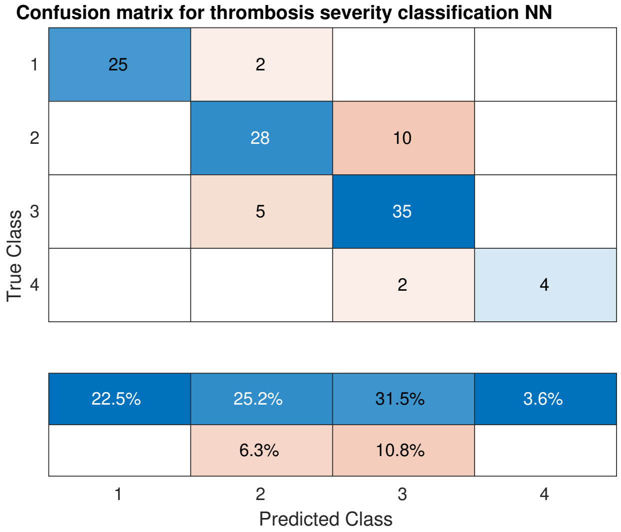

Confusion matrix for thrombosis severity classification NN

True Class	1	2	3	4
1	25	2		
2		28	10	
3		5	35	
4			2	4

	1	2	3	4
	22.5%	25.2%	31.5%	3.6%
		6.3%	10.8%	

Predicted Class

Figure 15.4: Confusion matrix for thrombosis severity classification NN with reconstructed images as input data. Class #1 corresponds to thrombi not present and class #2 corresponds to thrombi present.

Chapter 16

Real mock experiments

The developed methods were tested on the real mock over the course of several measurements. For each of the three balloon target positions five measurements were completed and averaged. The same averaging approach was used also for the homogenous measurement. GREIT reconstruction lead to results depicted in Figure 16.1. It is obvious that the reconstruction isn't accurate and the balloon positions couldn't be recovered easily from the reconstructed images.

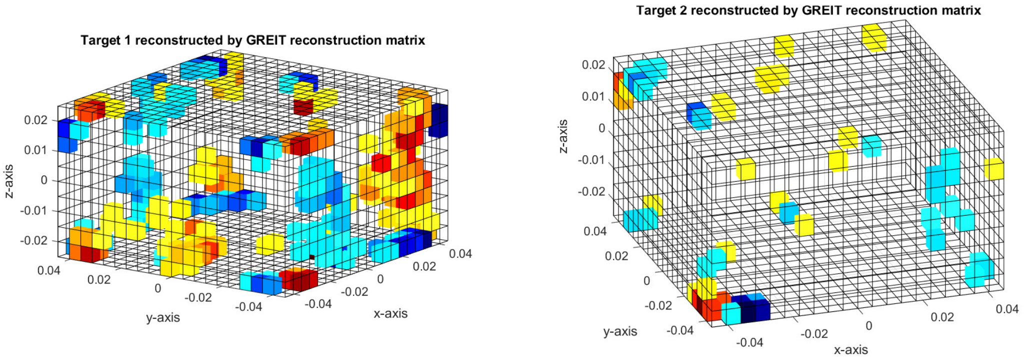

(a) : Reconstructed target 1.

(b) : Reconstructed target 2.

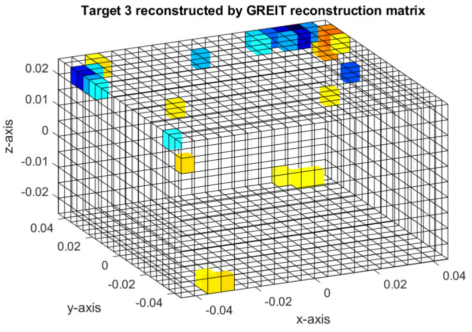

(c) : Reconstructed target 3.

Figure 16.1: Mock oxygenator GREIT reconstruction of three test targets.

Even though the reconstruction wasn't useful for determining the target position, tests were done to inspect whether it is still possible to detect at least thrombus presence. The relative voltage differences were also used as thrombi presence predictors. The option of thrombosis severity prediction was also explored. Results for all targets from the classification tasks performed by respective NNs are described in Table 16.1. Thrombus detection based on voltage measurements was successful for two targets, whereas detection based on reconstructed image was not successful at all. Thrombosis severity was correctly assigned in all three cases from voltage measurements and wrongly assigned in all three cases from reconstructed images. It was confirmed that the reconstruction perturbed the voltage differences in such a way that thrombi detection and thrombosis severity assessment became unstable.

Classification task	Input data source	Predicted outputs
Thrombus detection	Voltage measurement	[0, 1, 1]
Thrombus detection	Reconstructed image	[0, 0, 0]
Thrombosis severity	Voltage measurement	[1, 1, 1]
Thrombosis severity	Reconstructed image	[4, 2, 4]

Table 16.1: Summarized results of classification tasks on a real mock for test targets 1, 2 and 3; predicted outputs are in following format: [target 1, target 2, target 3].

Increased robustness of the measuring process as well as better reconstruction approaches might bring better reconstruction results in the future. Better electrodes and system of their connection to the measuring device should be considered for future development.

Chapter 17

Conclusions and future outlook

In this thesis, a complete pipeline for the early detection and characterization of thrombi in oxygenators was proposed. All simulations and data processing were done in MATLAB and EIDORS. Many functions complementing EIDORS' abilities were implemented along the way to support the method development, e.g. thrombus generation based a likelihood distribution or electrode position generation. Firstly, preliminary experiments were conducted to reveal the optimization potential of electrode placement and I-M patterns. Measurement selection criteria were designed as well. Afterwards, the search for an optimal electrode placement was conducted using an NN. This arrangement of electrodes should result in successful thrombi detection in all oxygenator areas. The optimization didn't lead to an electrode set with the desired oxygenator coverage, so a predefined electrode set with an optimized I-M pattern was used for further stages. 3D image reconstruction was performed next. A GREIT reconstruction matrix was trained on predefined targets, which enabled me to include information about the spatial thrombus deposition likelihood. Though the reconstruction proved to be inadequate for high quality image reconstruction, some information about thrombi could still be extracted. Secondly, A LeNet CNN architecture which performs well on 2D EIT reconstruction in practice was chosen for an extension to 3D. However, training wasn't successful even though the spatial relationship of measurements was considered in the LeNet input data. Thrombus detection and thrombosis severity estimation were inspected next. Four FC NNs were trained to detect thrombi and assess thrombosis severity both from voltage measurements and from GREIT reconstructed images. Voltage measurements were found to be better for these classification tasks. An accuracy of more than 90 % on test dataset was achieved for thrombi detection based on voltage measurements. In the end, the proposed approaches were tested on a real mock oxygenator with air balloon targets. Measured voltages proved to be valuable for thrombi presence estimation and thrombosis severity assessment even in these real-life measurements. Overall, it was confirmed that the detection of thrombi in oxygenators using EIT is possible. The detection of thrombi and determination of thrombosis severity was achieved using voltage measurements from electrodes. The biggest drawback was image reconstruction, for which extensive method development is still necessary. The entire pipeline was set up to facilitate easy modifications of the implemented algorithms in the future. In this way, it enables a future research continuity.

There are several key aspects that should be considered in the future for a follow-up of this thesis. Firstly, it is crucial to find out the theoretical limit of thrombi size detectability for oxygenator. It would be advantageous for practice if thrombi even several mm in size could be detected. Next, it should be considered whether the mock oxygenator isn't an over-simplified model. The real oxygenator consists of thousands of tiny non-conductive tubes which certainly significantly alter the current propagation. There is also a potential to explore influence of different electrode materials, shapes and amounts. It might be of interest to also simulate measurements with electrode placements on oxygenator sides. It is possible that this approach may bring a significant improvement in the method's detection and reconstruction capabilities. After static experiments are carried out, a dynamic experiment with flowing blood should be conducted to evaluate the influence of flow on conductivity and thrombus detection.

All of these suggestions are aimed mainly at the distant future. As of now, a better reconstruction approach should be proposed. I think that NNs are the right way to go as they can perfectly capture the nonlinear essence of EIT. There are many different architectures that can be tested for improvements in image reconstruction.

Bibliography

[1] A. Löf, J. P. Müller, and M. A. Brehm, "A biophysical view on von willebrand factor activation," *Journal of Cellular Physiology*, vol. 233, pp. 799–810, may 2017.

[2] D. Monroe and M. Hoffman, "A cell-based model of hemostasis," *Thrombosis and Haemostasis*, vol. 85, no. 06, pp. 958–965, 2001.

[3] G. Lippi and E. Favaloro, "Venous and arterial thromboses: Two sides of the same coin?," *Seminars in Thrombosis and Hemostasis*, vol. 44, pp. 239–248, sep 2017.

[4] D. R. Kumar, E. Hanlin, I. Glurich, J. J. Mazza, and S. H. Yale, "Virchow's contribution to the understanding of thrombosis and cellular biology," *Clinical Medicine & Research*, vol. 8, pp. 168–172, aug 2010.

[5] K. Neubauer and B. Zieger, "Endothelial cells and coagulation," *Cell and Tissue Research*, vol. 387, pp. 391–398, may 2021.

[6] J. S. O'Donnell, J. M. O'Sullivan, and R. J. S. Preston, "Advances in understanding the molecular mechanisms that maintain normal haemostasis," *British Journal of Haematology*, vol. 186, pp. 24–36, mar 2019.

[7] H. M. O. van Straaten, J. A. Kellum, and R. Bellomo, "Clinical review: Anticoagulation for continuous renal replacement therapy - heparin or citrate?," *Critical Care*, vol. 15, no. 1, p. 202, 2010.

[8] K. A. Bauer, "Pros and cons of new oral anticoagulants," *Hematology*, vol. 2013, pp. 464–470, dec 2013.

[9] B. Illum, M. Odish, A. Minokadeh, C. Yi, R. L. Owens, T. Pollema, and J. N. LaBuzetta, "Evaluation, treatment, and impact of neurologic injury in adult patients on extracorporeal membrane oxygenation: a review," *Current Treatment Options in Neurology*, vol. 23, mar 2021.

[10] W. C. Wrisinger and S. L. Thompson, "Basics of extracorporeal membrane oxygenation," *Surgical Clinics of North America*, vol. 102, pp. 23–35, feb 2022.

[11] F. Sangalli, N. Patroniti, and A. Pesenti, eds., *ECMO-Extracorporeal Life Support in Adults*. Springer Milan, 2014.

[12] E. L. S. Organization, "Elso." https://www.elso.org/, July 2023.

[13] I. Halaweish, A. Cole, E. Cooley, W. R. Lynch, and J. W. Haft, “Roller and centrifugal pumps,” *ASAIO Journal*, vol. 61, pp. 496–501, sep 2015.

[14] E. Papadimas, L. Leow, Y. K. Tan, L. Shen, K. Ramanathan, A. M. Choong, and G. MacLaren, “Centrifugal and roller pumps in neonatal and pediatric extracorporeal membrane oxygenation: A systematic review and meta-analysis of clinical outcomes,” *ASAIO Journal*, vol. 68, pp. 311–317, may 2021.

[15] Y. S. Moon, S. Ohtsubo, M. R. Gomez, J. K. Moon, and Y. Nose, “Comparison of centrifugal and roller pump hemolysis rates at low flow,” *Artificial Organs*, vol. 20, pp. 579–581, may 1996.

[16] K. N. Johnson, B. Carr, G. B. Mychaliska, R. B. Hirschl, and S. K. Gadepalli, “Switching to centrifugal pumps may decrease hemolysis rates among pediatric ECMO patients,” *Perfusion*, vol. 37, pp. 123–127, jan 2021.

[17] Özge Erdem, J. W. Kuiper, R. J. Houmes, C. H. van Ommen, J. van Rosmalen, D. Tibboel, and E. D. Wildschut, “Coagulation complications after conversion from roller to centrifugal pump in neonatal and pediatric extracorporeal membrane oxygenation,” *Journal of Pediatric Surgery*, vol. 56, pp. 1378–1385, aug 2021.

[18] B. Meyns, L. Vercaemst, E. Vandezande, H. Bollen, and D. Vlasselaers, “Plasma leakage of oxygenators in ECMO depends on the type of oxygenator and on patient variables,” *The International Journal of Artificial Organs*, vol. 28, pp. 30–34, jan 2005.

[19] E. Khoshbin, N. Roberts, C. Harvey, D. Machin, H. Killer, G. J. Peek, A. W. Sosnowski, and R. K. Firmin, “Poly-methyl pentene oxygenators have improved gas exchange capability and reduced transfusion requirements in adult extracorporeal membrane oxygenation,” *ASAIO Journal*, vol. 51, pp. 281–287, may 2005.

[20] S. Gregory, M. Stevens, and J. Fraser, eds., *Mechanical Circulatory and Respiratory Support.* Academic Press, Oct. 2017.

[21] S. Yamane, Y. Ohashi, A. Sueoka, K.Sato, J. Kuwana, and Y. Nosé, “Development of a silicone hollow fiber membrane oxygenator for ecmo application,” *ASAIO Journal*, vol. 44, pp. 384–387, sep 1998.

[22] A. Funakubo, T. Higami, I. Sakuma, Y. Fukui, R. Kawamura, K. Sato, and A. Sueoka, “Development of a membrane oxygenator for ecmo using a novel fine silicone hollow fiber,” *ASAIO Journal*, vol. 42, pp. 837–840, sep 1996.

[23] A. Moreau, B. Levy, F. Annoni, R. Lorusso, F. Su, M. Belliato, and F. S. Taccone, “The use of induced hypothermia in extracorporeal membrane oxygenation: A narrative review,” *Resuscitation Plus*, vol. 13, p. 100360, mar 2023.

[24] Getinge, “Getinge.” https://www.getinge.com/, July 2023.

[25] R. G. Conway, J. Zhang, J. Jeudy, C. Evans, T. Li, Z. J. Wu, and B. P. Griffith, “Computed tomography angiography as an adjunct to computational fluid dynamics for prediction of oxygenator thrombus formation,” *Perfusion*, vol. 36, pp. 285–292, jul 2020.

[26] S. Staessens, M. D. Moussa, A. Pierache, A. Rauch, N. Rousse, E. Boulleaux, A. Ung, L. Desender, B. Pradines, A. Vincentelli, O. Mercier, J. Labreuche, A. Duhamel, E. V. Belle, F. Vincent, A. Dupont, K. Vanhoorelbeke, D. Corseaux, S. F. D. Meyer, and S. Susen, “Thrombus formation during ECMO: Insights from a detailed histological analysis of thrombus composition,” *Journal of Thrombosis and Haemostasis*, vol. 20, pp. 2058–2069, sep 2022.

[27] S. M. Hastings, D. N. Ku, S. Wagoner, K. O. Maher, and S. Deshpande, “Sources of circuit thrombosis in pediatric extracorporeal membrane oxygenation,” *ASAIO Journal*, vol. 63, pp. 86–92, jan 2017.

[28] C. Dornia, A. Philipp, S. Bauer, M. Lubnow, T. Müller, K. Lehle, C. Schmid, R. Müller-Wille, P. Wiggermann, C. Stroszczynski, and A. G. Schreyer, “Analysis of thrombotic deposits in extracorporeal membrane oxygenators by multidetector computed tomography,” *ASAIO Journal*, vol. 60, pp. 652–656, nov 2014.

[29] J. J. Hathcock, “Flow effects on coagulation and thrombosis,” *Arteriosclerosis, Thrombosis, and Vascular Biology*, vol. 26, pp. 1729–1737, aug 2006.

[30] M. Lubnow, A. Philipp, M. Foltan, T. B. Enger, D. Lunz, T. Bein, A. Haneya, C. Schmid, G. Riegger, T. Müller, and K. Lehle, “Technical complications during veno-venous extracorporeal membrane oxygenation and their relevance predicting a system-exchange – retrospective analysis of 265 cases,” *PLoS ONE*, vol. 9, p. e112316, dec 2014.

[31] M. Türkmen, T. Lauwigi, T. Fechter, F. Gries, A. Fischbach, T. Gries, R. Rossaint, C. Bleilevens, and P. Winnersbach, “Bioimpedance analysis as early predictor for clot formation inside a blood-perfused test chamber: Proof of concept using an in vitro test-circuit,” *Biosensors*, vol. 13, p. 394, mar 2023.

[32] A. Kaesler, F. Hesselmann, M. O. Zander, P. C. Schlanstein, G. Wagner, P. Bruners, T. Schmitz-Rode, U. Steinseifer, and J. Arens, “Technical indicators to evaluate the degree of large clot formation inside the membrane fiber bundle of an oxygenator in an in vitro setup,” *Artificial Organs*, vol. 43, pp. 159–166, oct 2018.

[33] T. Dowrick, C. Blochet, and D. Holder, “In vivo bioimpedance measurement of healthy and ischaemic rat brain: implications for stroke imaging using electrical impedance tomography,” *Physiological Measurement*, vol. 36, pp. 1273–1282, may 2015.

[34] M. Noshiro, S. Nebuya, A. Fujimaki, R. Smallwood, and B. Brown, “Frequency characteristics of the electrical conductivity in normal and coagulated blood,” in *IFMBE Proceedings*, pp. 70–72, Springer Berlin Heidelberg, 2007.

[35] S. Gelfan and J. P. Quigley, "CONDUCTIVITY OF BLOOD DURING COAGULATION," *American Journal of Physiology-Legacy Content*, vol. 94, pp. 531–534, sep 1930.

[36] H. Chen, J. Yao, L. Yang, K. Liu, B. Chen, J. Li, and M. Takei, "Development of a portable electrical impedance tomography device for online thrombus detection in extracorporeal-circulation equipment," *IEEE Sensors Journal*, vol. 21, pp. 3653–3659, feb 2021.

[37] A. Sapkota, T. Fuse, M. Seki, O. Maruyama, M. Sugawara, and M. Takei, "Application of electrical resistance tomography for thrombus visualization in blood," *Flow Measurement and Instrumentation*, vol. 46, pp. 334–340, dec 2015.

[38] N. Istuk, A. L. Gioia, H. Benchakroun, A. Lowery, B. McDermott, and M. O'Halloran, "Relationship between the conductivity of human blood and blood counts," *IEEE Journal of Electromagnetics, RF and Microwaves in Medicine and Biology*, vol. 6, pp. 184–190, jun 2022.

[39] S. Leonhardt and B. Lachmann, "Electrical impedance tomography: the holy grail of ventilation and perfusion monitoring?," *Intensive Care Medicine*, vol. 38, pp. 1917–1929, sep 2012.

[40] M. Bodenstein, M. David, and K. Markstaller, "Principles of electrical impedance tomography and its clinical application," *Critical Care Medicine*, vol. 37, pp. 713–724, feb 2009.

[41] E. L. Costa, R. G. Lima, and M. B. Amato, "Electrical impedance tomography," *Current Opinion in Critical Care*, vol. 15, pp. 18–24, feb 2009.

[42] A. Adler and D. Holder, *Electrical Impedance Tomography.* CRC Press, nov 2021.

[43] D. Nguyen, W. Chik, R. Kosobrodov, M. Barry, J. Pouliopoulos, C. Jin, A. McEwan, and A. Thiagalingam, "Pulmonary embolism detection with electrical impedance tomography," *Heart, Lung and Circulation*, vol. 22, pp. S192–S193, jan 2013.

[44] A. Adler and W. R. B. Lionheart, "Uses and abuses of EIDORS: an extensible software base for EIT," *Physiological Measurement*, vol. 27, pp. S25–S42, apr 2006.

[45] P. M. Faia, R. Silva, M. G. Rasteiro, F. A. P. Garcia, A. R. Ferreira, M. J. Santos, J. B. Santos, and A. P. Coimbra, "Imaging particulate two-phase flow in liquid suspensions with electric impedance tomography," *Particulate Science and Technology*, vol. 30, pp. 329–342, jul 2012.

[46] D. Pepper and J. Heinrich, *The Finite Element Method: Basic Concepts and Applications with MATLAB, MAPLE, and COMSOL, Third Edition.* Computational and Physical Processes in Mechanics and Thermal Sciences, CRC Press, 2017.

[47] B. Brown, “Electrical impedance tomography (EIT): a review,” *Journal of Medical Engineering & Technology*, vol. 27, pp. 97–108, jan 2003.

[48] E. Smela, “EIT for tactile sensing:considerations regarding the injection-measurement pattern,” *Engineering Research Express*, vol. 4, p. 045041, dec 2022.

[49] A. Adler, P. O. Gaggero, and Y. Maimaitijiang, “Adjacent stimulation and measurement patterns considered harmful,” *Physiological Measurement*, vol. 32, pp. 731–744, jun 2011.

[50] T. A. Khan and S. H. Ling, “Review on electrical impedance tomography: Artificial intelligence methods and its applications,” *Algorithms*, vol. 12, p. 88, apr 2019.

[51] X. Zheng and G. Kou, “Research on EIT image reconstruction based on improved GREIT algorithm,” in *2019 IEEE International Conference on Signal, Information and Data Processing (ICSIDP)*, IEEE, dec 2019.

[52] A. Adler, J. H. Arnold, R. Bayford, A. Borsic, B. Brown, P. Dixon, T. J. C. Faes, I. Frerichs, H. Gagnon, Y. Gärber, B. Grychtol, G. Hahn, W. R. B. Lionheart, A. Malik, R. P. Patterson, J. Stocks, A. Tizzard, N. Weiler, and G. K. Wolf, “Greit: a unified approach to 2d linear eit reconstruction of lung images,” *Physiological Measurement*, vol. 30, pp. S35–S55, jun 2009.

[53] K. Suzuki, ed., *Artificial Neural Networks - Methodological Advances and Biomedical Applications*. InTech, apr 2011.

[54] R. Yamashita, M. Nishio, R. K. G. Do, and K. Togashi, “Convolutional neural networks: an overview and application in radiology,” *Insights into Imaging*, vol. 9, pp. 611–629, jun 2018.

[55] F. Alrasheedi, X. Zhong, and P.-C. Huang, “Padding module: Learning the padding in deep neural networks,” *IEEE Access*, vol. 11, pp. 7348–7357, 2023.

[56] J. Gu, Z. Wang, J. Kuen, L. Ma, A. Shahroudy, B. Shuai, T. Liu, X. Wang, G. Wang, J. Cai, and T. Chen, “Recent advances in convolutional neural networks,” *Pattern Recognition*, vol. 77, pp. 354–377, may 2018.

[57] F. Mehmood, S. Ahmad, and T. K. Whangbo, “An efficient optimization technique for training deep neural networks,” *Mathematics*, vol. 11, p. 1360, mar 2023.

[58] D. Singh and B. Singh, “Investigating the impact of data normalization on classification performance,” *Applied Soft Computing*, vol. 97, p. 105524, dec 2020.

[59] MetaCentrum, “Metacentrum (metavo).” https://metavo.metacentrum.cz/cs/, Aug. 2023.

[60] T. M. Inc., “Matlab version: 9.14.0.2206163 (r2023a),” 2023.

[61] S. S. I. GmbH, "Sciospec isx-3." https://www.sciospec.com/product/isx-3/, Aug. 2023.

[62] N. Polydorides and W. R. B. Lionheart, "A matlab toolkit for three-dimensional electrical impedance tomography: a contribution to the electrical impedance and diffuse optical reconstruction software project," *Measurement Science and Technology*, vol. 13, pp. 1871–1883, nov 2002.

[63] J. Schöberl, "NETGEN an advancing front 2d/3d-mesh generator based on abstract rules," *Computing and Visualization in Science*, vol. 1, pp. 41–52, jul 1997.

[64] I. Foundation, "Tissue frequency chart." https://itis.swiss/virtual-population/tissue-properties/database/tissue-frequency-chart/, Aug. 2023.

[65] C. Onsager, C. Wang, C. Costakis, C. Aygen, L. Lang, S. van der Lee, and M. A. Grayson, "Sensitivity analysis for optimizing electrical impedance tomography protocols," 2021.

[66] D. Smyl and D. Liu, "Optimizing electrode positions in 2-d electrical impedance tomography using deep learning," *IEEE Transactions on Instrumentation and Measurement*, vol. 69, pp. 6030–6044, sep 2020.

[67] C. Tan, S. Lv, F. Dong, and M. Takei, "Image reconstruction based on convolutional neural network for electrical resistance tomography," *IEEE Sensors Journal*, vol. 19, pp. 196–204, jan 2019.

Appendices

Appendix A

Additional results

A.1 Preliminary experiments

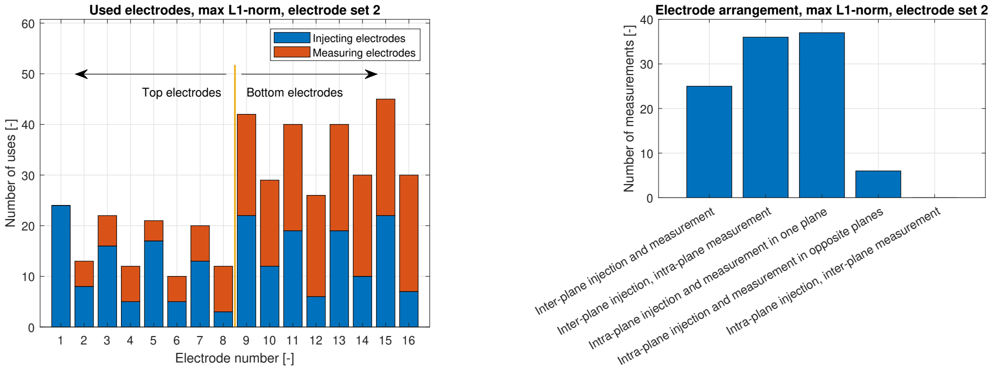

(a) : Statistics of electrode usage for electrode set 2 and max L1-norm measurements.

(b) : Electrode arrangement statistics for electrode set 2 and max L1-norm measurements.

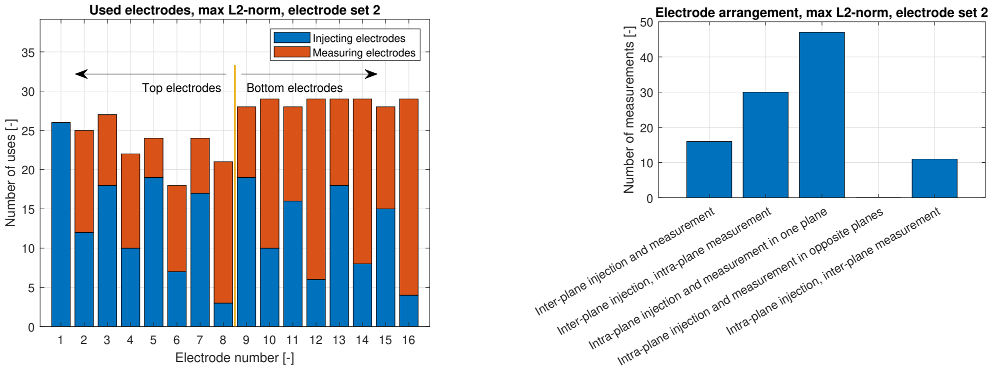

(c) : Statistics of electrode usage for electrode set 2 and max L2-norm measurements.

(d) : Electrode arrangement statistics for electrode set 2 and max L2-norm measurements.

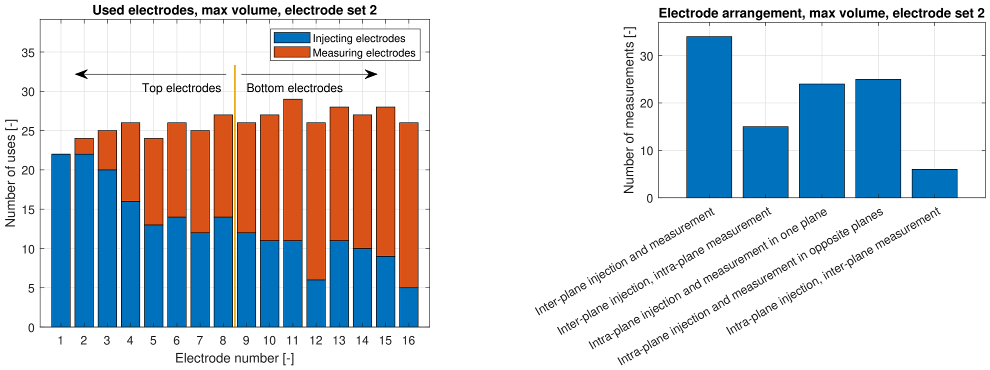

(e) : Statistics of electrode usage for electrode set 2 and max parallelotope volume measurements.

(f) : Electrode arrangement statistics for electrode set 2 and max parallelotope volume measurements.

Figure A.1: Electrode utilization analysis for measurement selection, electrode set 2.

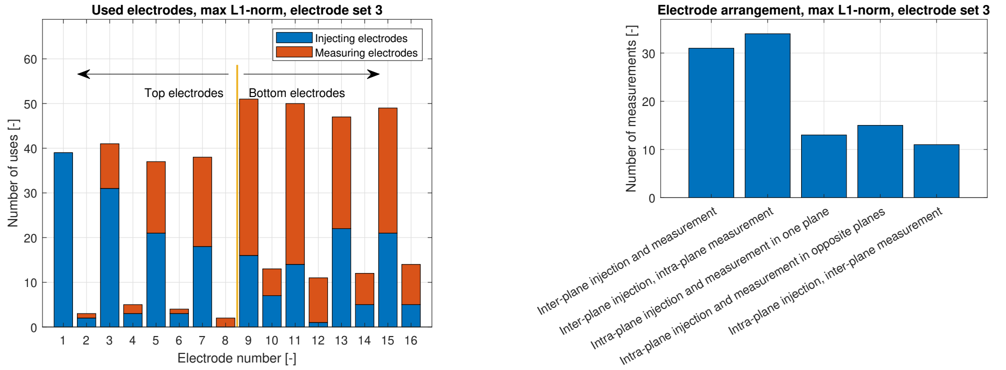

(a) : Statistics of electrode usage for electrode set 3 and max L1-norm measurements.

(b) : Electrode arrangement statistics for electrode set 3 and max L1-norm measurements.

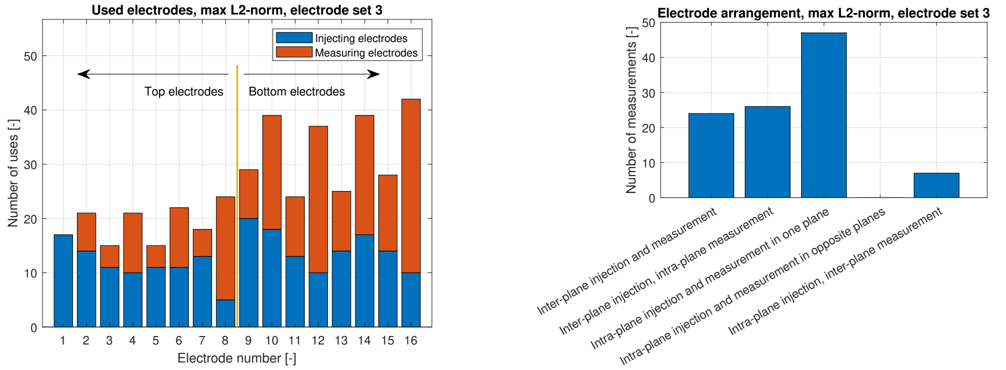

(c) : Statistics of electrode usage for electrode set 3 and max L2-norm measurements.

(d) : Electrode arrangement statistics for electrode set 3 and max L2-norm measurements.

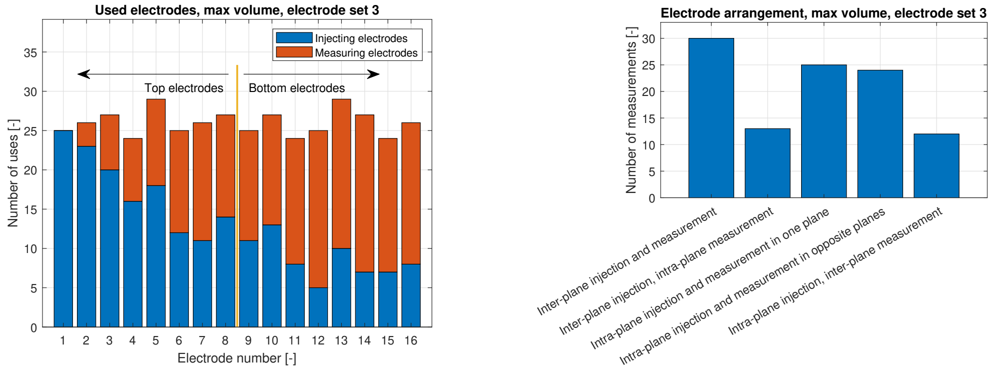

(e) : Statistics of electrode usage for electrode set 3 and max parallelotope volume measurements.

(f) : Electrode arrangement statistics for electrode set 3 and max parallelotope volume measurements.

Figure A.2: Electrode utilization analysis for measurement selection, electrode set 3.

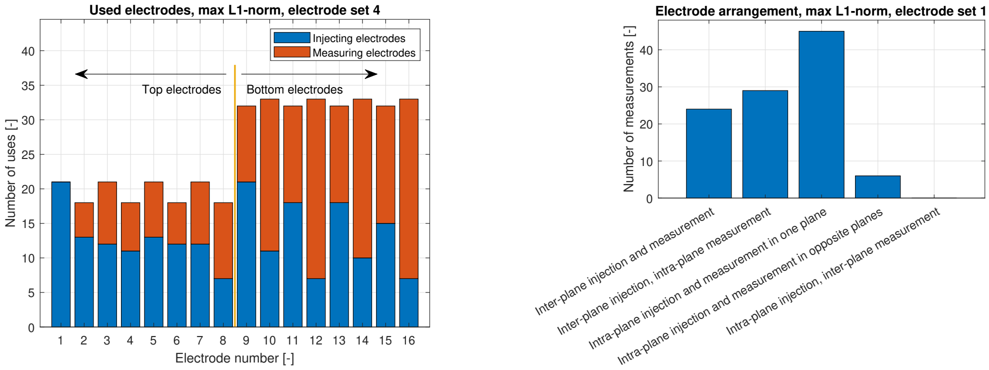

(a) : Statistics of electrode usage for electrode set 4 and max L1-norm measurements.

(b) : Electrode arrangement statistics for electrode set 4 and max L1-norm measurements.

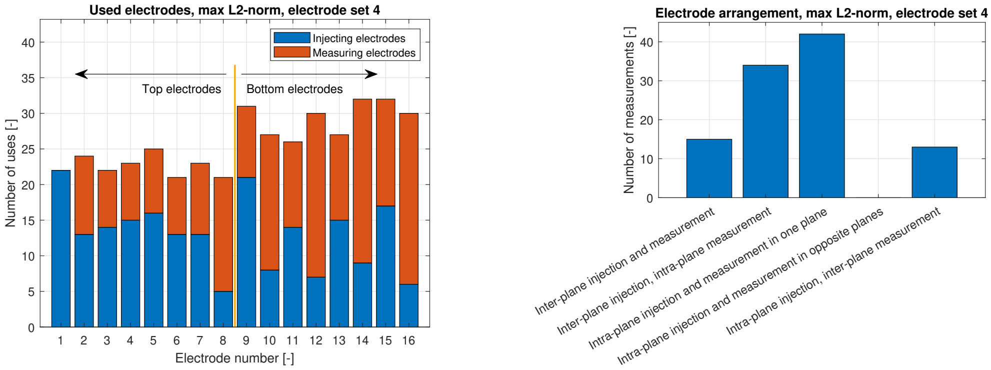

(c) : Statistics of electrode usage for electrode set 4 and max L2-norm measurements.

(d) : Electrode arrangement statistics for electrode set 4 and max L2-norm measurements.

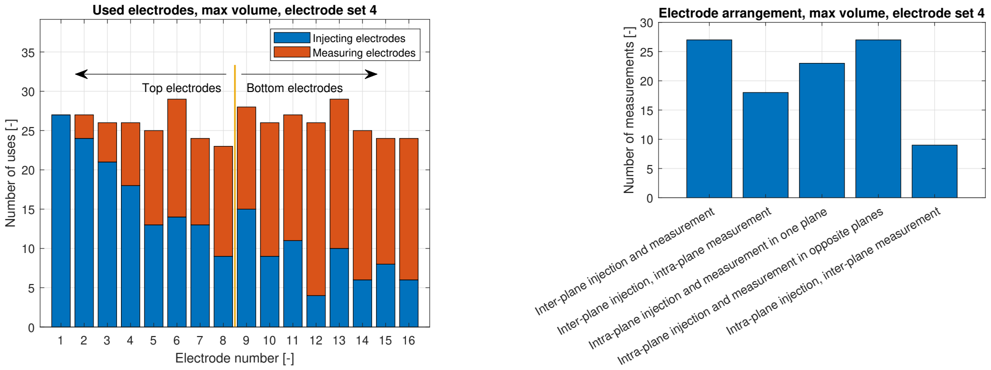

(e) : Statistics of electrode usage for electrode set 4 and max parallelotope volume measurements.

(f) : Electrode arrangement statistics for electrode set 4 and max parallelotope volume measurements.

Figure A.3: Electrode utilization analysis for measurement selection, electrode set 4.

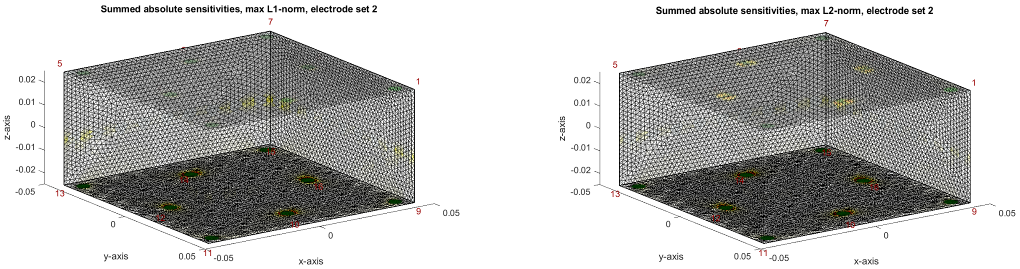

(a) : Spatial finite element sensitivity distribution, max L1-norm, electrode set 2.

(b) : Spatial finite element sensitivity distribution, max L2-norm, electrode set 2.

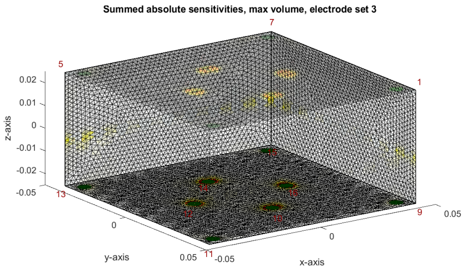

(c) : Spatial finite element sensitivity distribution, max volume, electrode set 2.

Figure A.4: Spatial finite element sensitivity distribution, electrode set 2.

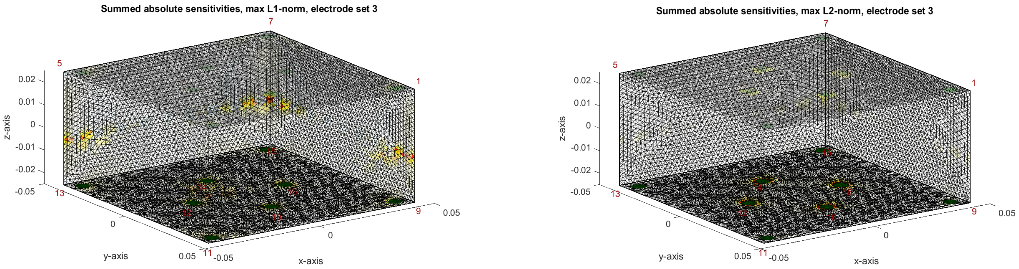

(a) : Spatial finite element sensitivity distribution, max L1-norm, electrode set 3.

(b) : Spatial finite element sensitivity distribution, max L2-norm, electrode set 3.

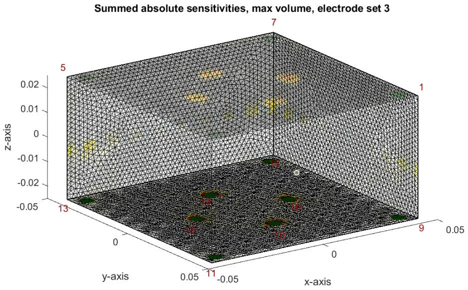

(c) : Spatial finite element sensitivity distribution, max volume, electrode set 3.

Figure A.5: Spatial finite element sensitivity distribution, electrode set 3.

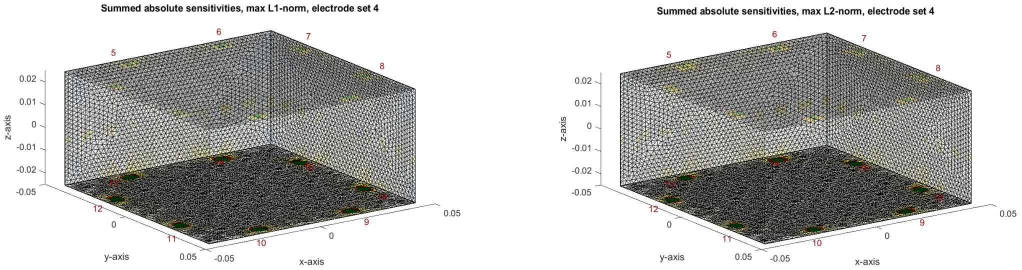

(a) : Spatial finite element sensitivity distribution, max L1-norm, electrode set 4.

(b) : Spatial finite element sensitivity distribution, max L2-norm, electrode set 4.

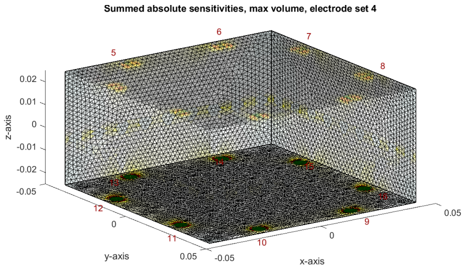

(c) : Spatial finite element sensitivity distribution, max volume, electrode set 4.

Figure A.6: Spatial finite element sensitivity distribution, electrode set 4.

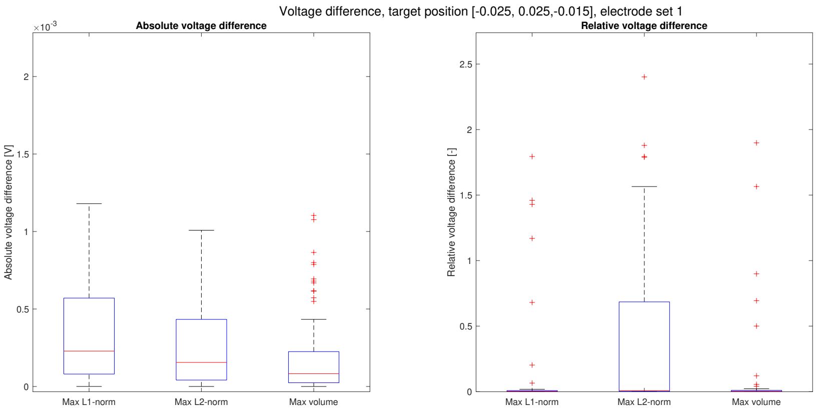

(a) : Absolute and relative voltage difference, target approximately in the middle of distance between center and wall, electrode set 1.

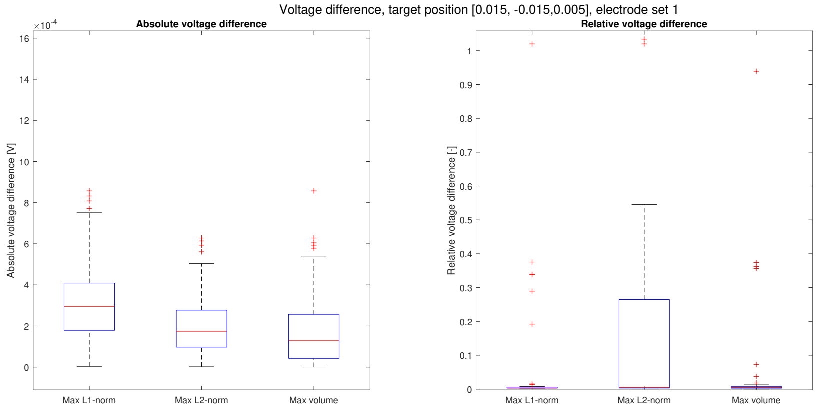

(b) : Absolute and relative voltage difference, target near the oxygenator center, electrode set 1.

Figure A.7: Absolute and relative voltage difference for two targets, electrode set 1.

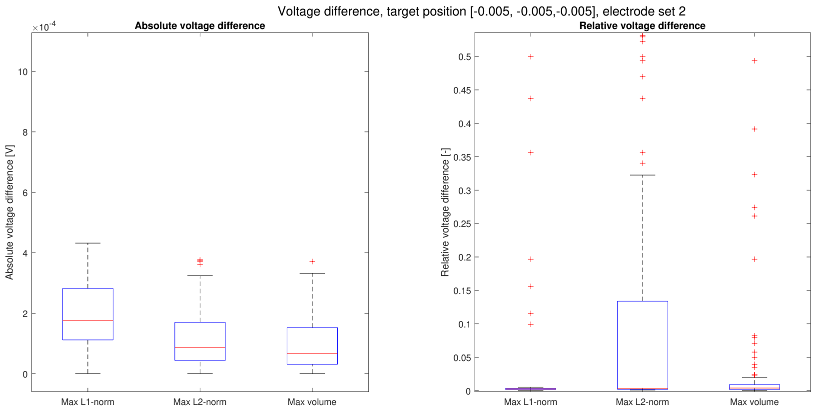

(a) : Absolute and relative voltage difference, target near oxygenator center, electrode set 2.

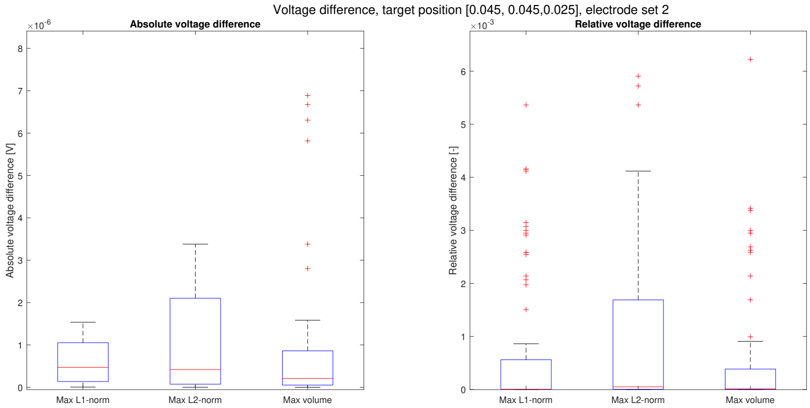

(b) : Absolute and relative voltage difference, target in the corner, electrode set 2.

Figure A.8: Absolute and relative voltage difference for two targets, electrode set 2.

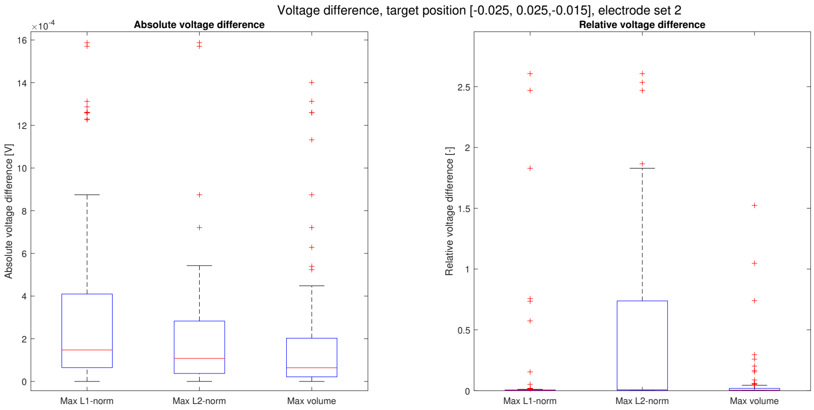

(a) : Absolute and relative voltage difference, target approximately in the middle of distance between center and wall, electrode set 2.

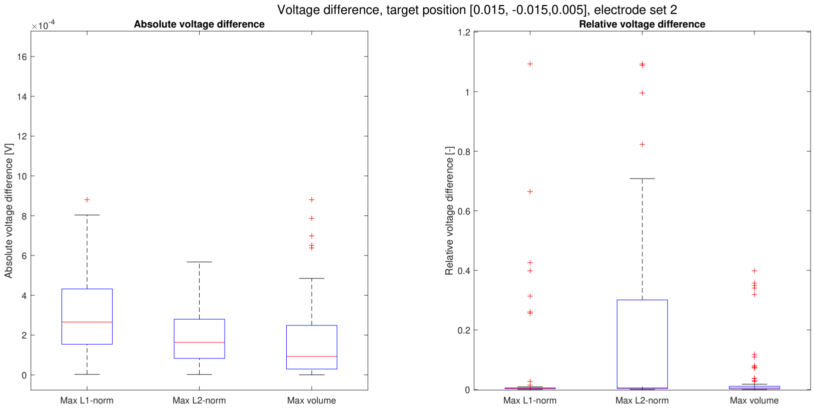

(b) : Absolute and relative voltage difference, target near the oxygenator center, electrode set 2.

Figure A.9: Absolute and relative voltage difference for two targets, electrode set 2.

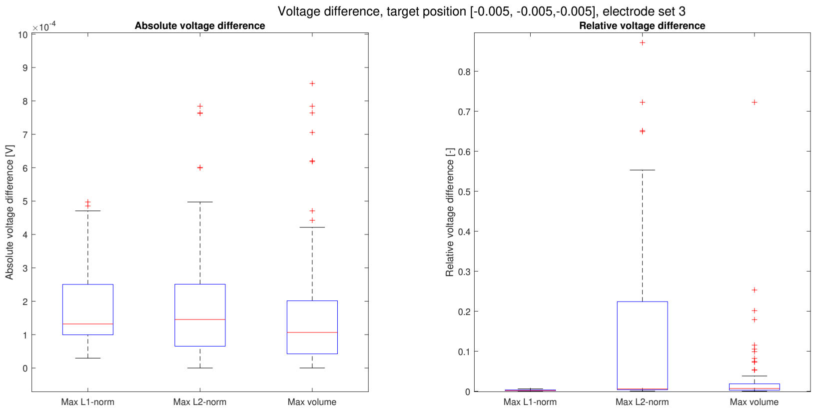

(a) : Absolute and relative voltage difference, target near oxygenator center, electrode set 3.

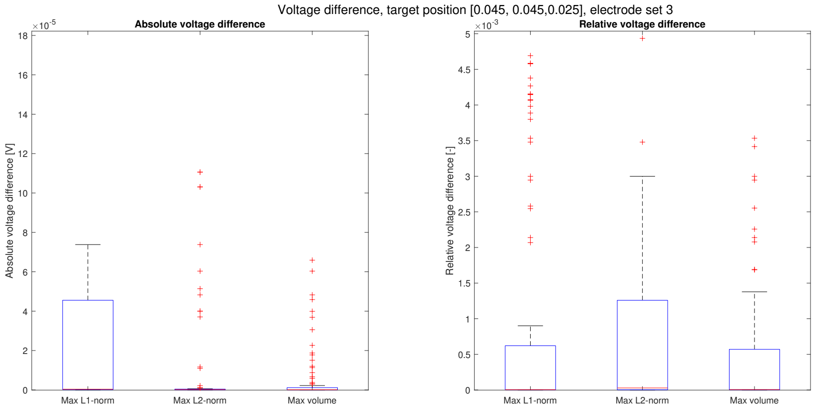

(b) : Absolute and relative voltage difference, target in the corner, electrode set 3.

Figure A.10: Absolute and relative voltage difference for two targets, electrode set 3.

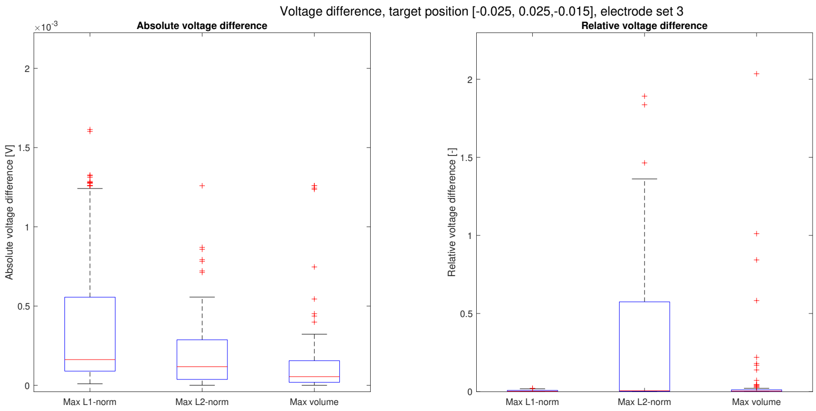

(a) : Absolute and relative voltage difference, target approximately in the middle of distance between center and wall, electrode set 3.

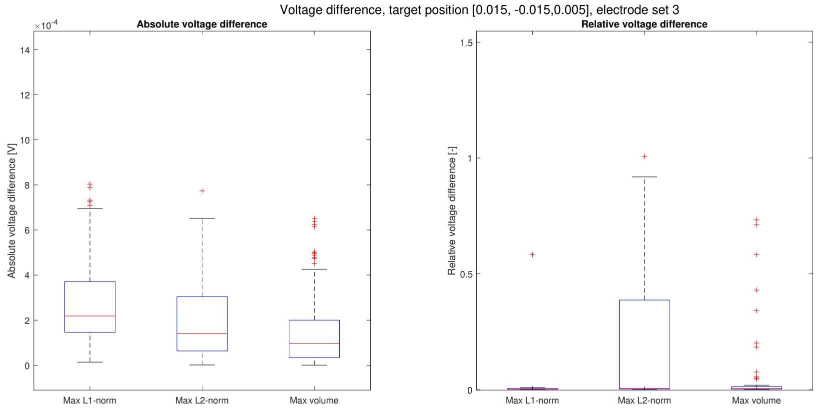

(b) : Absolute and relative voltage difference, target near the oxygenator center, electrode set 3.

Figure A.11: Absolute and relative voltage difference for two targets, electrode set 3.

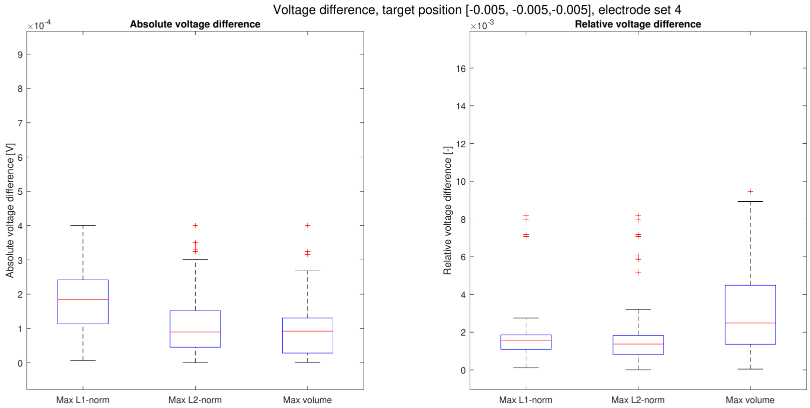

(a) : Absolute and relative voltage difference, target near oxygenator center, electrode set 4.

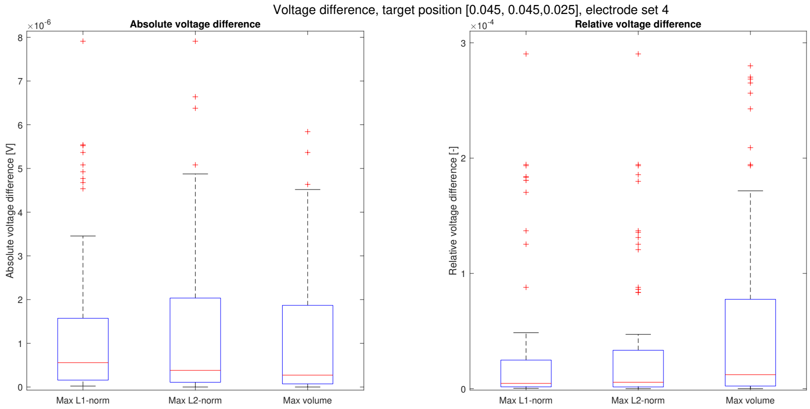

(b) : Absolute and relative voltage difference, target in the corner, electrode set 4.

Figure A.12: Absolute and relative voltage difference for two targets, electrode set 4.

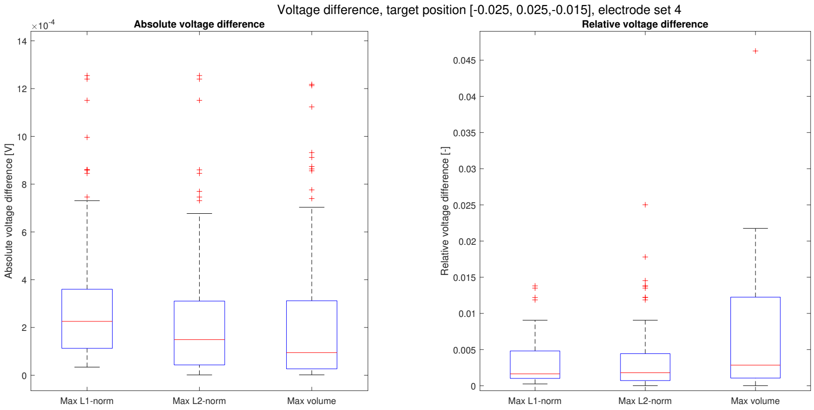

(a) : Absolute and relative voltage difference, target approximately in the middle of distance between center and wall, electrode set 4.

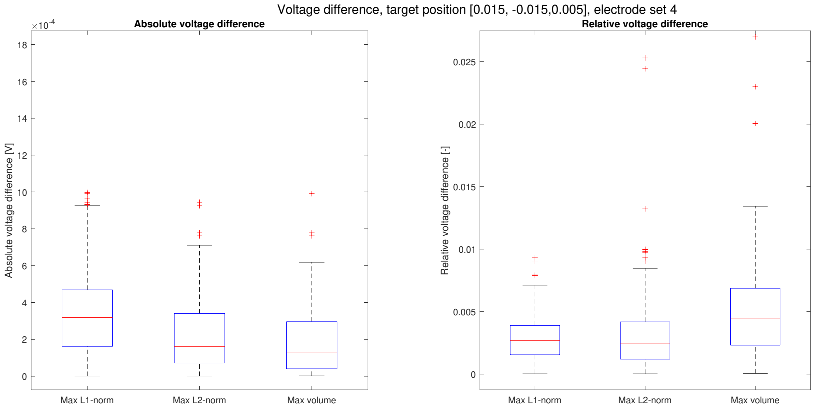

(b) : Absolute and relative voltage difference, target near the oxygenator center, electrode set 4.

Figure A.13: Absolute and relative voltage difference for two targets, electrode set 4.

A.2 Electrode positions and I-M pattern optimization

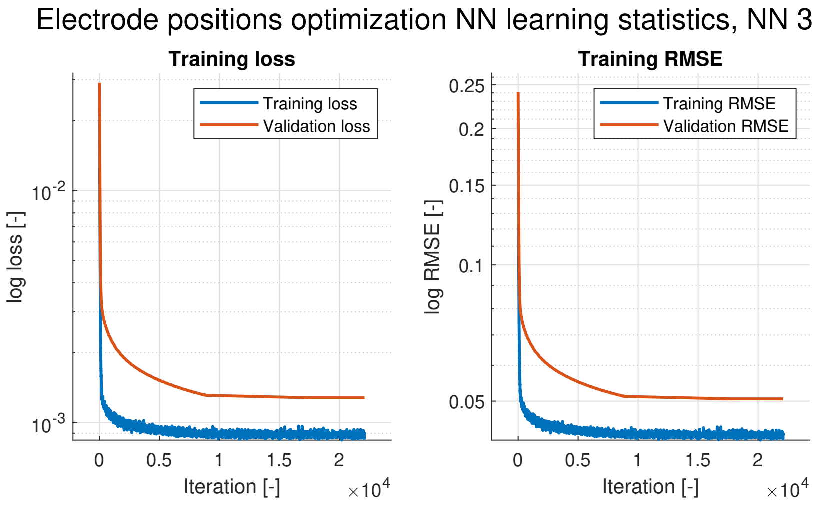

Figure A.14: Training statistics – training loss, training RMSE, validation loss and validation RMSE – for electrode position optimization NN 3.

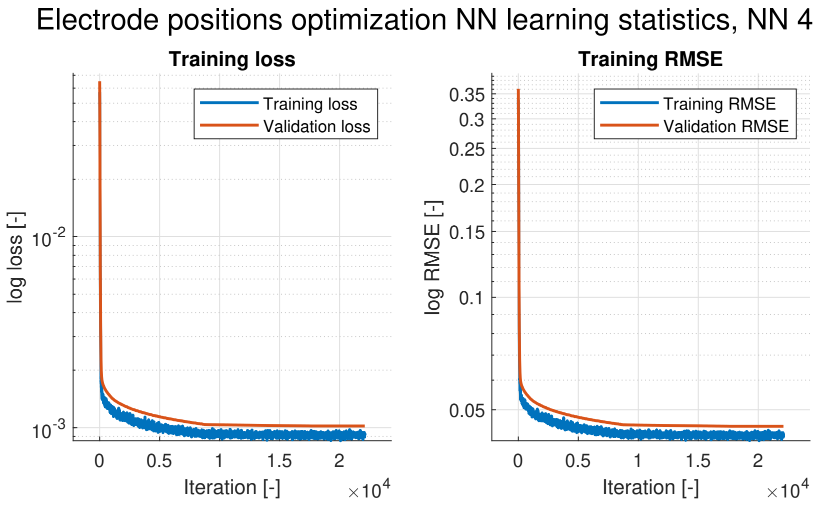

Figure A.15: Training statistics – training loss, training RMSE, validation loss and validation RMSE – for electrode position optimization NN 4.

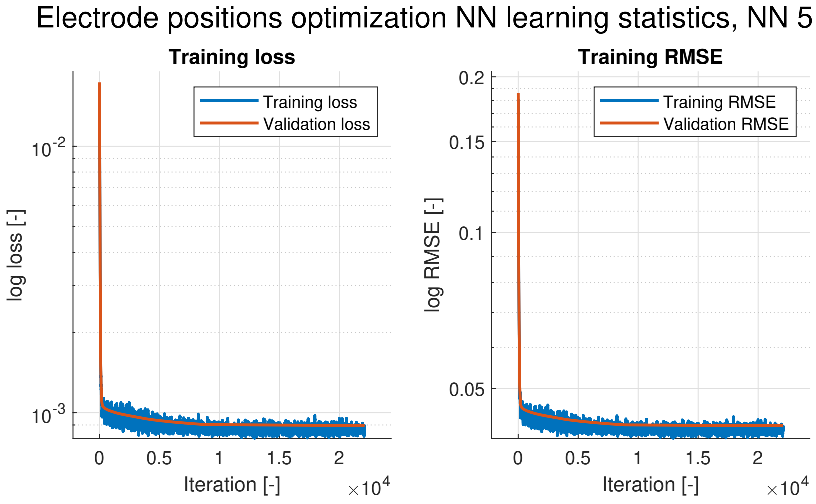

Figure A.16: Training statistics – training loss, training RMSE, validation loss and validation RMSE – for electrode position optimization NN 5.

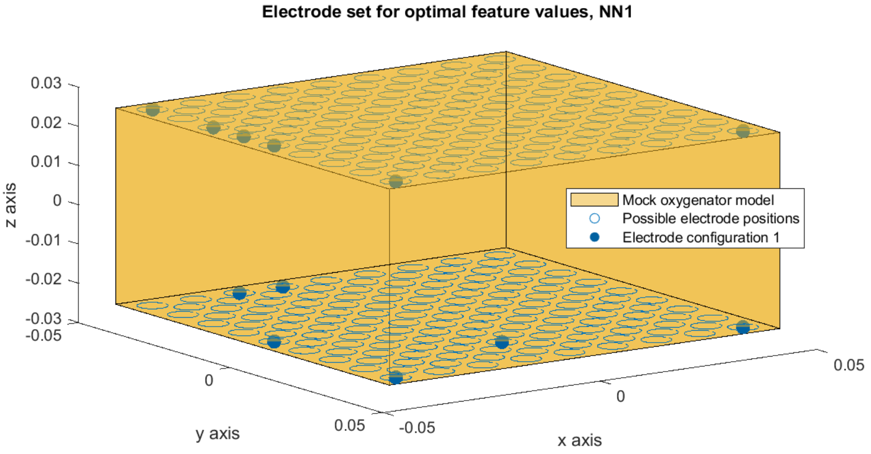

Figure A.17: Electrode sets computed as forward pass of optimal feature set 1 (electrode position optimization NN.

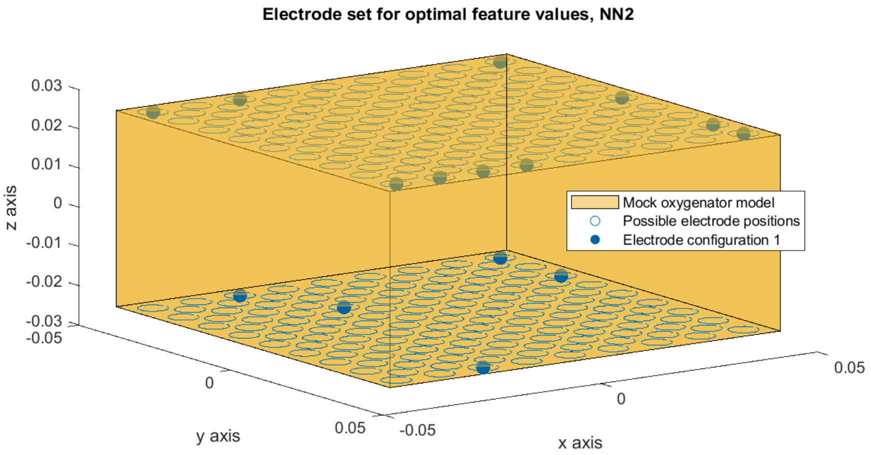

Figure A.18: Electrode sets computed as forward pass of optimal feature set 2 (electrode position optimization NN.

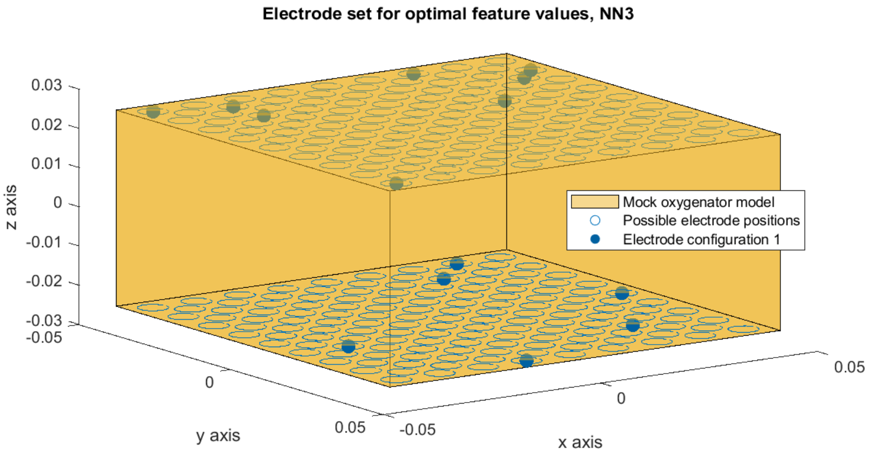

Figure A.19: Electrode sets computed as forward pass of optimal feature set 3 (electrode position optimization NN.

A.3 Optimized electrode positions

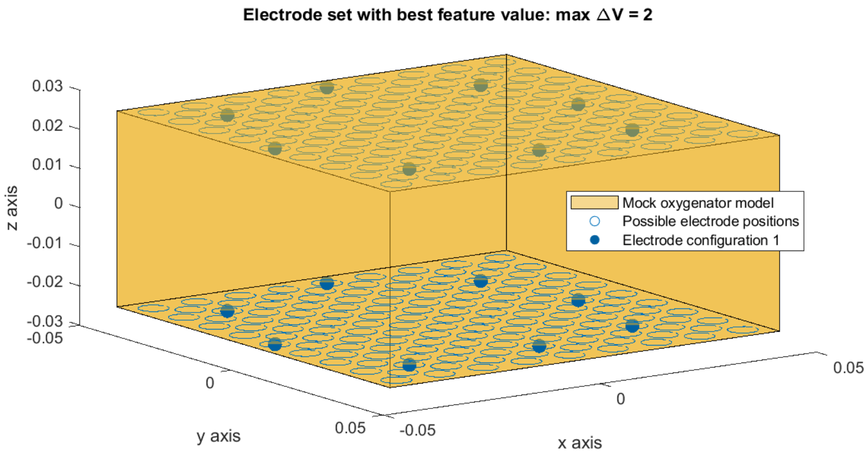

Figure A.20: A training electrode set with a minimum difference between the computed max ΔV feature and the optimal feature value.

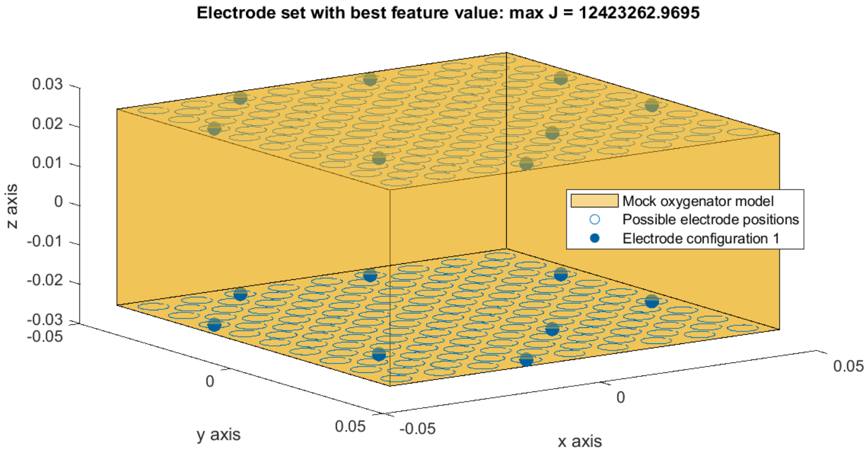

Figure A.21: A training electrode set with a minimum difference between the computed max J feature and the optimal feature value.

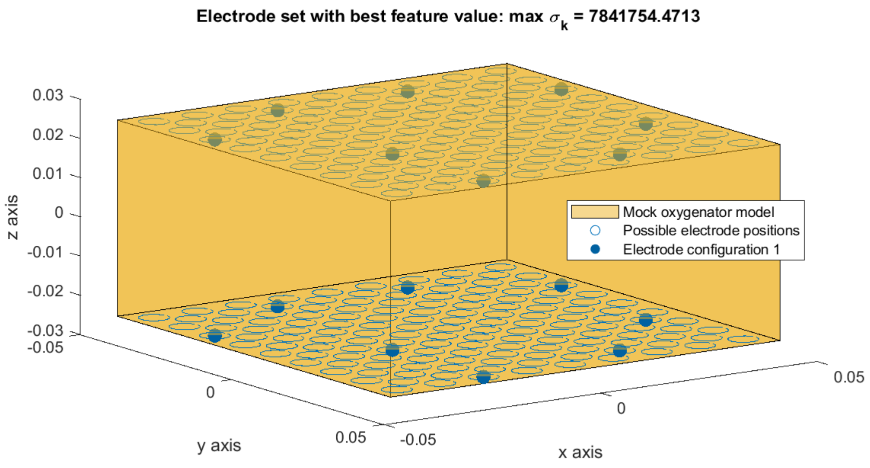

Figure A.22: A training electrode set with a minimum difference between the computed max σ_k feature and the optimal feature value.

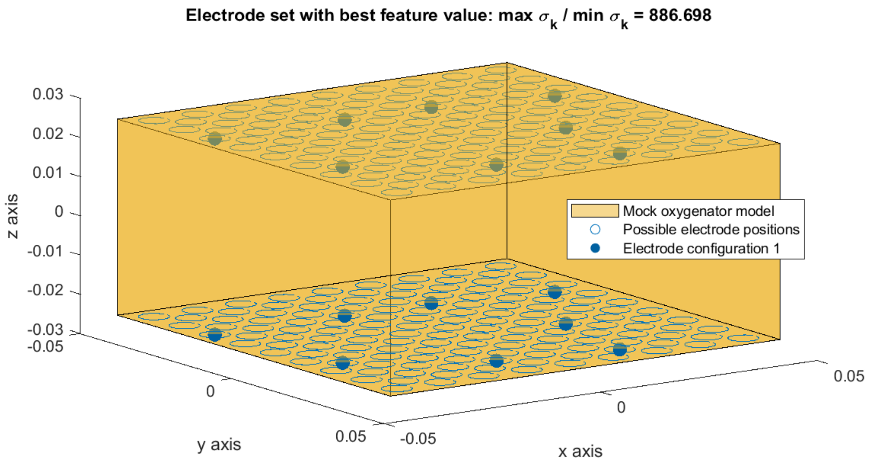

Figure A.23: A training electrode set with a minimum difference between the computed max σ_k / min σ_k feature and the optimal feature value.

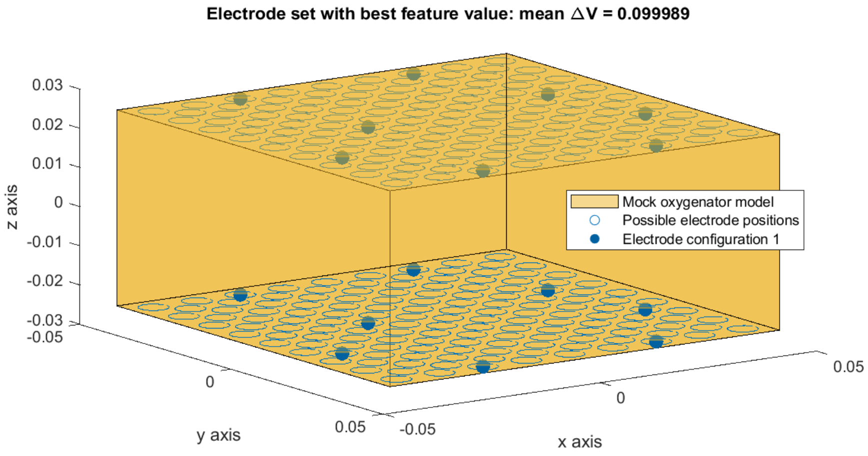

Figure A.24: A training electrode set with a minimum difference between the computed mean ΔV feature and the optimal feature value.

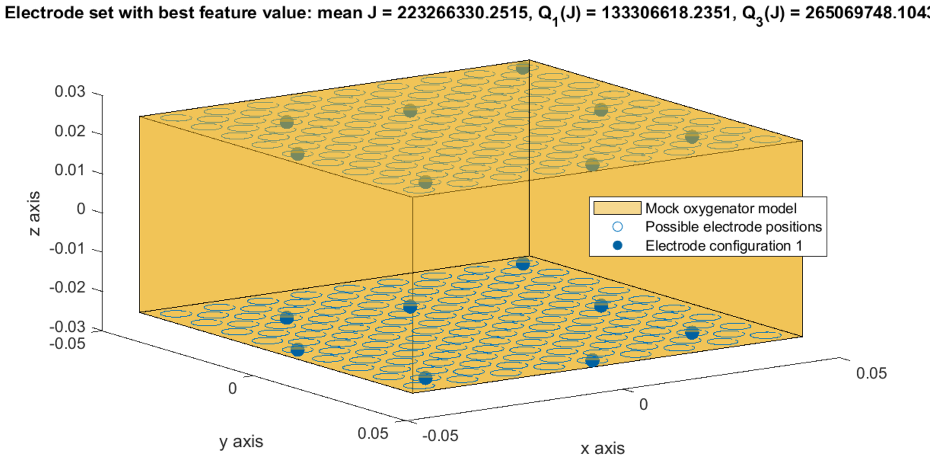

Figure A.25: A training electrode set with a minimum difference between the computed mean J, Q_1(J), and Q_3(J) features and the optimal feature value; electrode placement for all these features was identical.

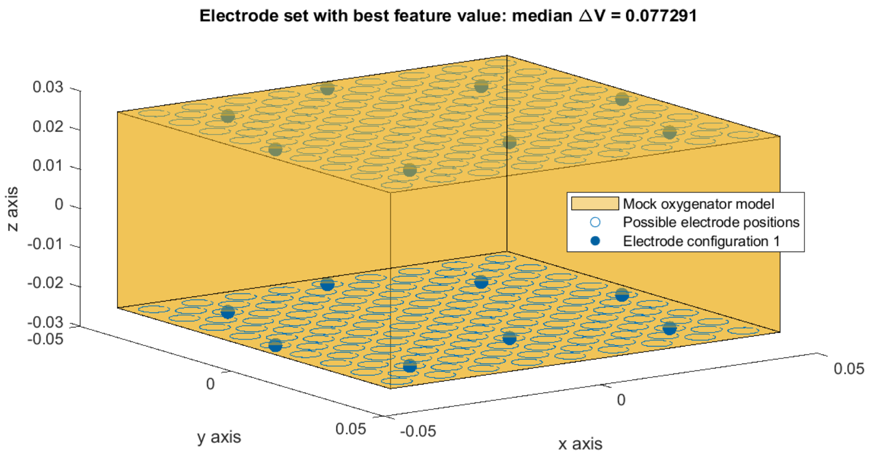

Figure A.26: A training electrode set with a minimum difference between the computed median ΔV feature and the optimal feature value.

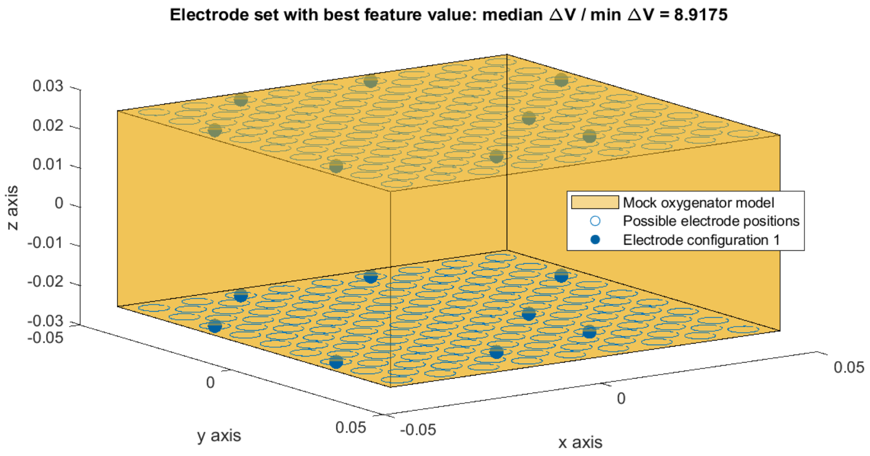

Figure A.27: A training electrode set with a minimum difference between the computed median ΔV / min ΔV feature and the optimal feature value.

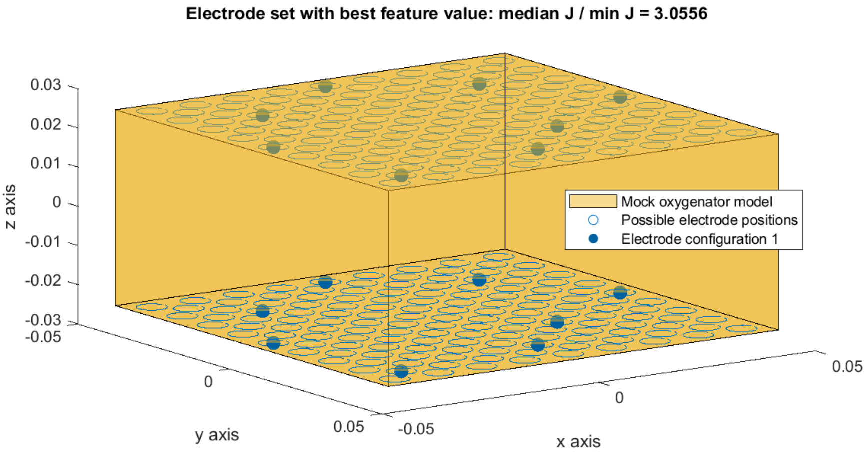

Figure A.28: A training electrode set with a minimum difference between the computed median J / min J feature and the optimal feature value.

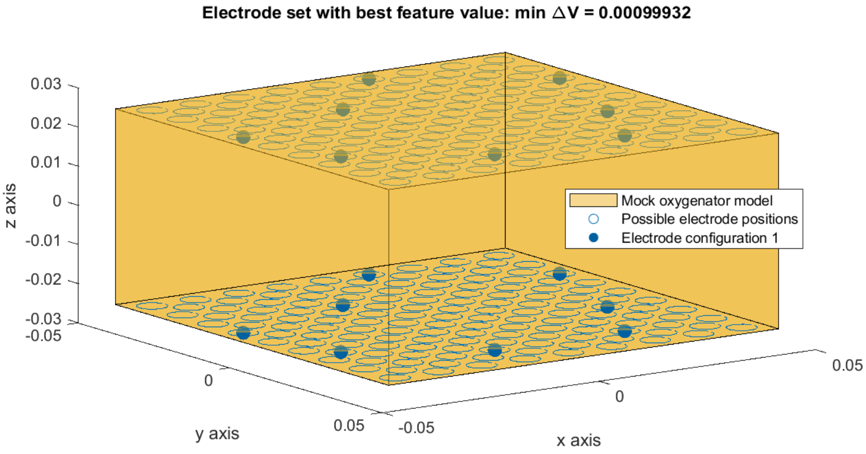

Figure A.29: A training electrode set with a minimum difference between the computed min ΔV feature and the optimal feature value.

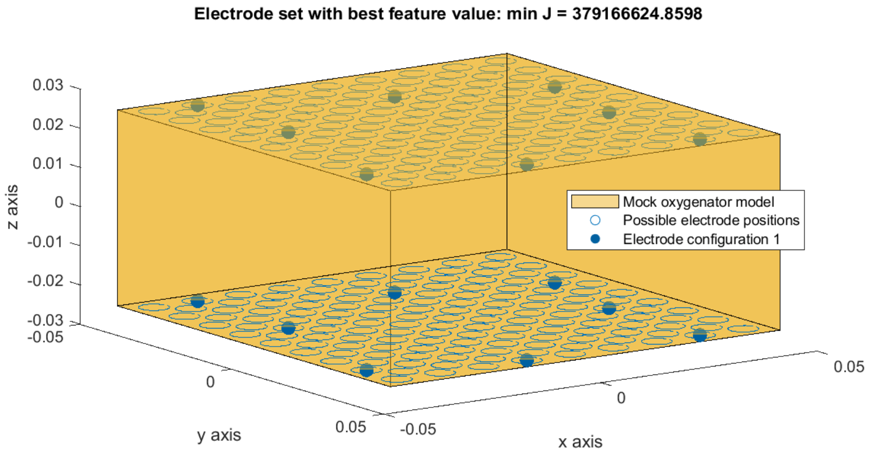

Figure A.30: A training electrode set with a minimum difference between the computed min J feature and the optimal feature value.

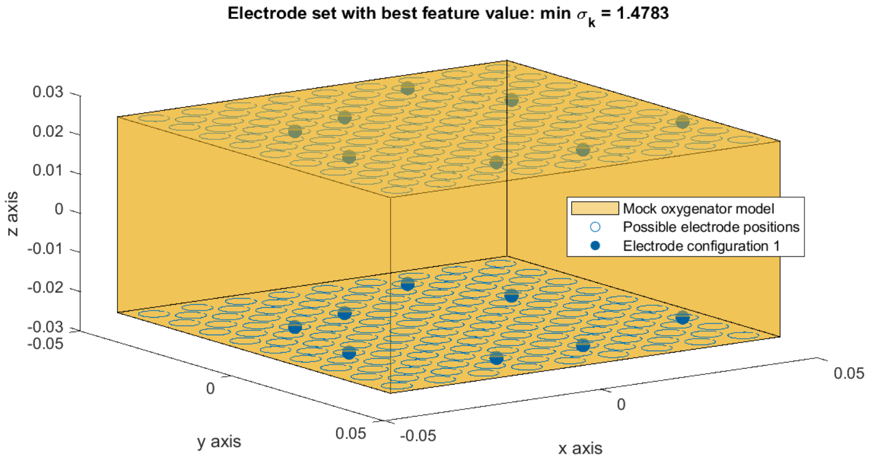

Figure A.31: A training electrode set with a minimum difference between the computed min σ_k feature and the optimal feature value.

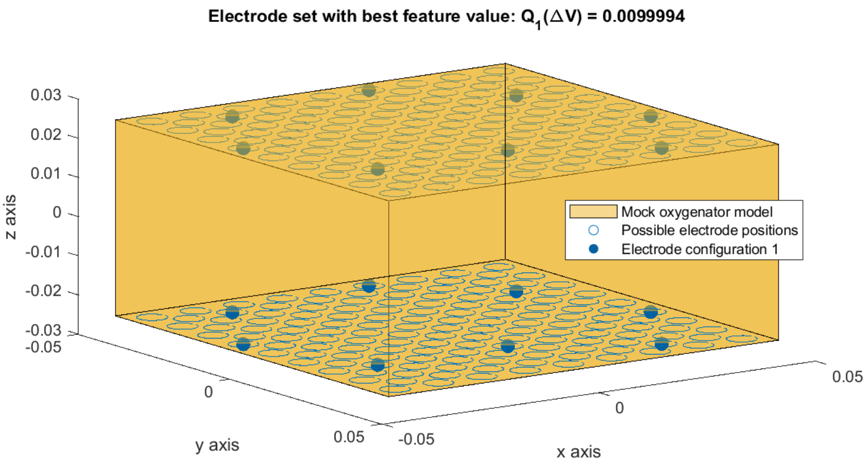

Figure A.32: A training electrode set with a minimum difference between the computed Q1 ΔV feature and the optimal feature value.

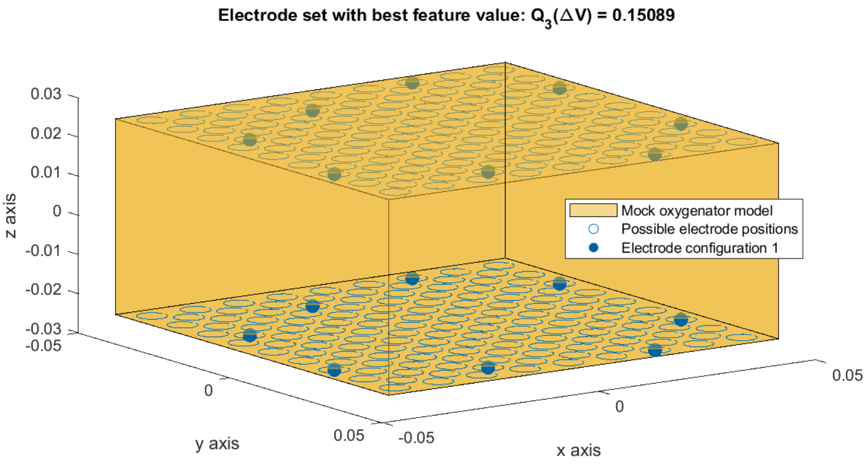

Figure A.33: A training electrode set with a minimum difference between the computed Q3 ΔV feature and the optimal feature value.

A.4 GREIT reconstruction

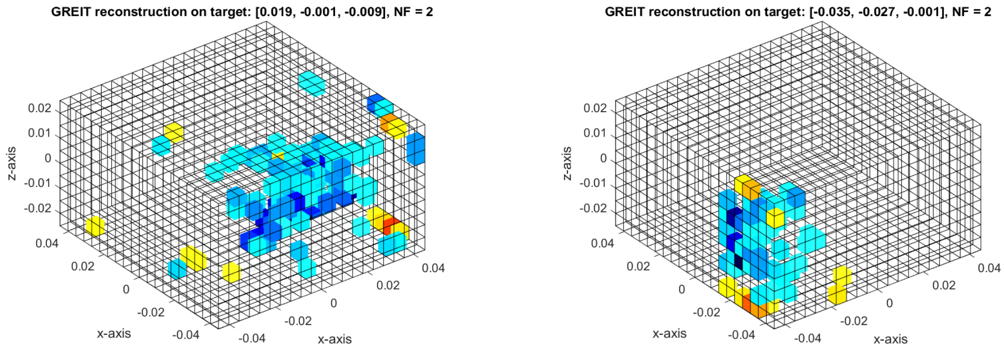
GREIT reconstruction on target: [0.019, -0.001, -0.009], NF = 2

GREIT reconstruction on target: [-0.035, -0.027, -0.001], NF = 2

(a) : Target # 1 reconstruction. **(b) :** Target # 2 reconstruction.

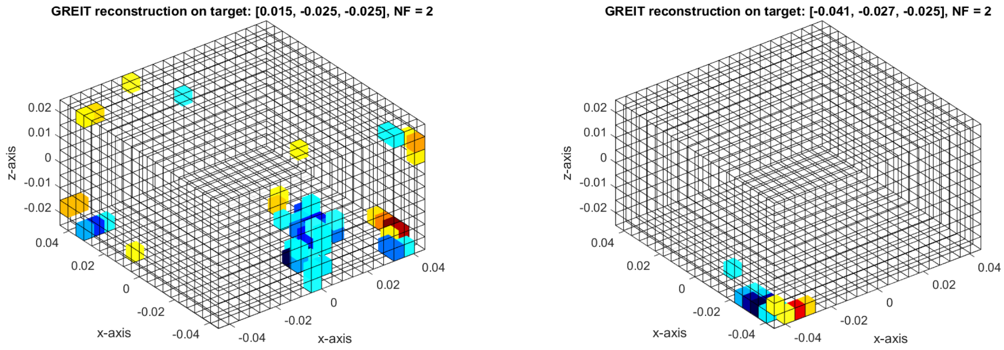
GREIT reconstruction on target: [0.015, -0.025, -0.025], NF = 2

GREIT reconstruction on target: [-0.041, -0.027, -0.025], NF = 2

(c) : Target # 3 reconstruction. **(d) :** Target # 4 reconstruction.

Figure A.34: GREIT reconstruction for NF $= 2$ and four different targets.

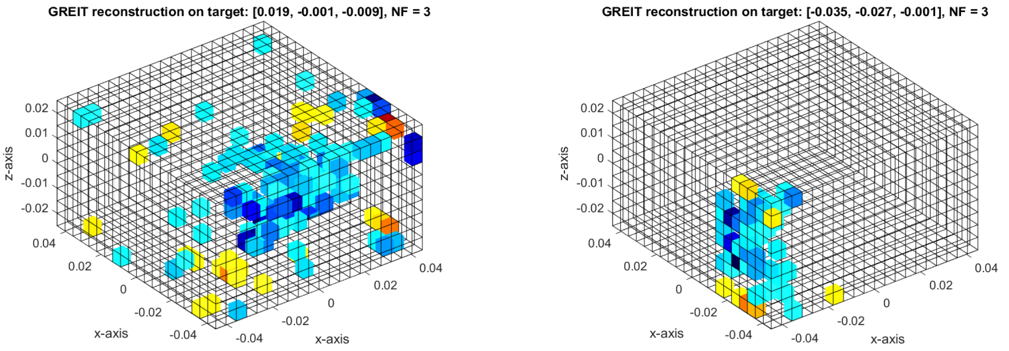

(a) : Target # 1 reconstruction.

(b) : Target # 2 reconstruction.

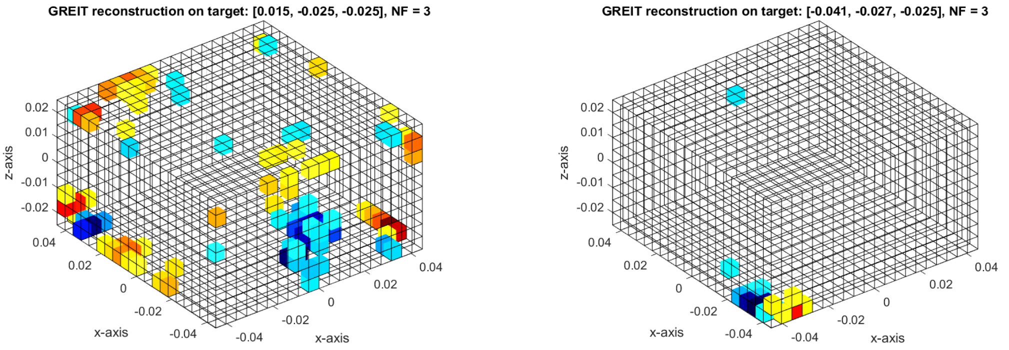

(c) : Target # 3 reconstruction.

(d) : Target # 4 reconstruction.

Figure A.35: GREIT reconstruction for NF = 3 and four different targets.

A.5 Thrombi detection and characterization

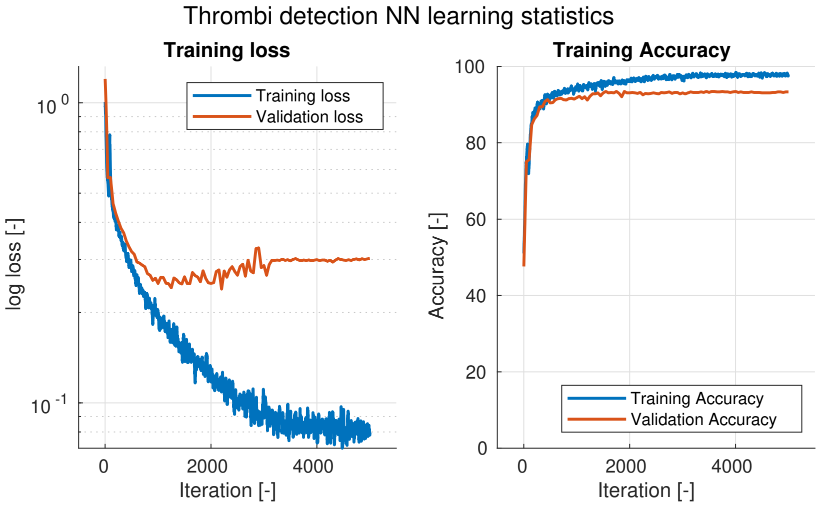

Figure A.36: Training statistics – training loss, training accuracy, validation loss and validation accuracy – for thrombi detection NN with voltage measurements as input data.

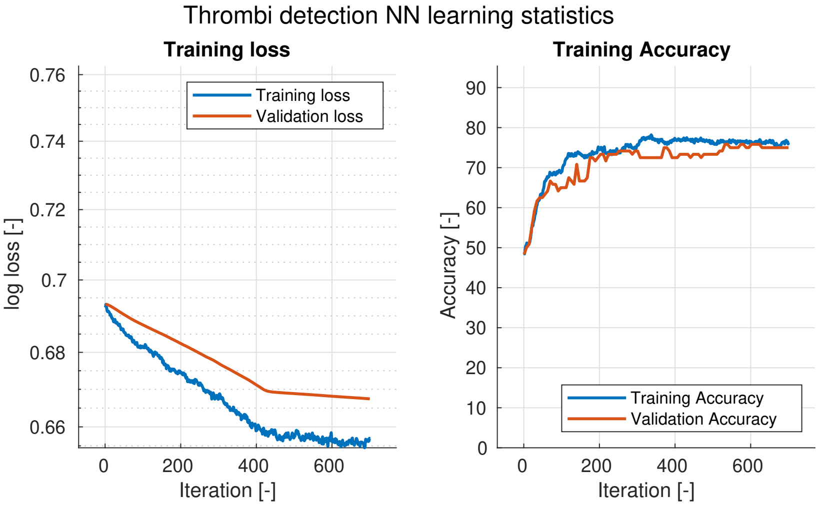

Figure A.37: Training statistics – training loss, training accuracy, validation loss and validation accuracy – for thrombi detection NN with reconstructed images as input data.

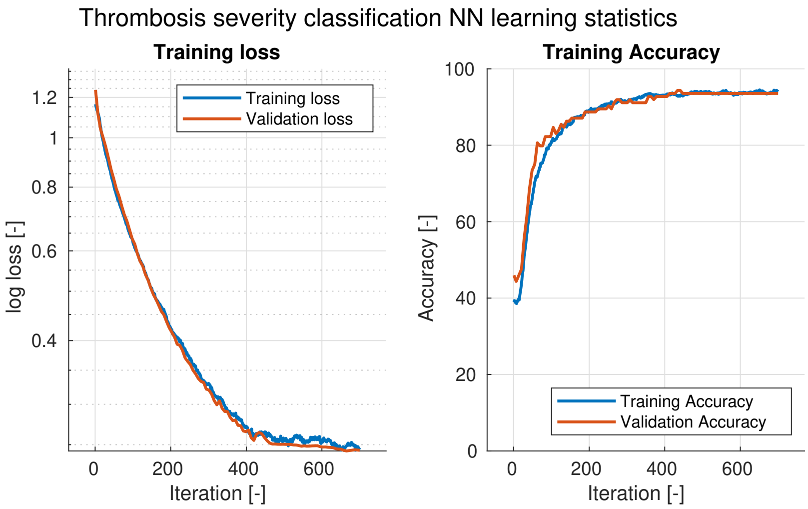

Figure A.38: Training statistics – training loss, training accuracy, validation loss and validation accuracy – for thrombosis severity classification NN with voltage measurements as input data.

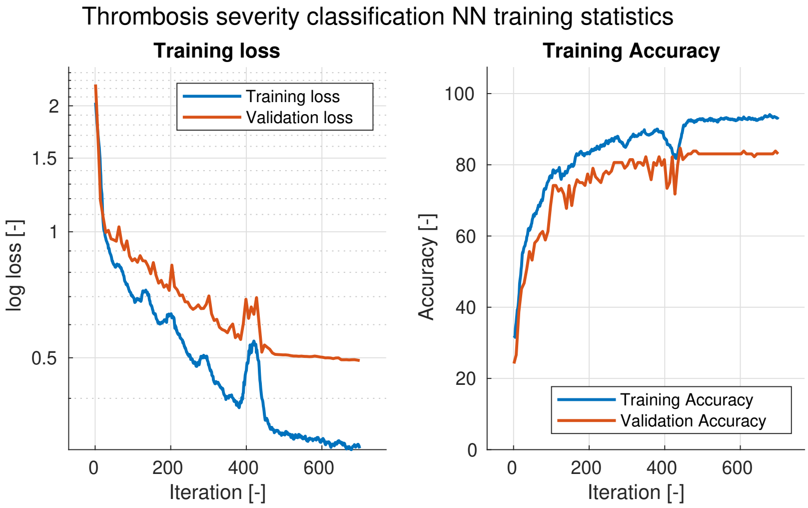

Figure A.39: Training statistics – training loss, training accuracy, validation loss and validation accuracy – for thrombosis severity classification NN with reconstructed images as input data.

Appendix B

Submitted files

- `Thesis.pdf`
- `scripts`
  - `checkDupliciteElectrodeSets.m`
  - `computeNdimensionalVolume.m`
  - `createInjectionMeasurementPattern.m`
  - `det_NNthrombiDetectionMeasurements.m`
  - `det_NNthrombiDetectionReconstruction.m`
  - `det_NNthrombiVolumeMeasurements.m`
  - `det_NNthrombiVolumeReconstruction.m`
  - `det_SVMthrombiDetectionMeasurements.m`
  - `det_generateTrainingDataDetection.m`
  - `det_generateTrainingDataVolume.m`
  - `el_generateTraningDataNN.m`
  - `el_selectIMpatternFinalCandidates.m`
  - `el_selectIMpatternNN.m`
  - `el_trainNN.m`
  - `exp_GREITreconstruction.m`
  - `exp_IMpatternInfluenceJacobian.m`
  - `exp_IMpatternInfluenceVoltage.m`
  - `exp_electrodePositionInfluenceJacobian.m`
  - `exp_electrodePositionInfluenceVoltage.m`
  - `exp_selectSensitiveMeasurementsMagnitude.m`
  - `exp_selectSensitiveMeasurementsVolume.m`
  - `exp_targetConductivityInfluenceVoltage.m`
  - `exp_targetSizeInfluenceVoltage.m`
  - `findElementId.m`
  - `findNearestPlausibleElectrodePosition.m`
  - `findTargetIndex.m`
  - `gaussian3D.m`
  - `generateElectrodePositions.m`
  - `generateTargets.m`
  - `generateTrainingDataNNpositionOptimization.m`
  - `getClassId.m`
  - `getElectrodeNodes.m`
  - `getElectrodePositionsNN.m`

- real_sciospecGREIT.m
- rec_GREITreconstruction.m
- rec_GREITtraining.m
- rec_NNthrombiReconstruction.m
- rec_SVMthrombiDetection.m
- rec_createNNinputMapping.m
- rec_generateTrainingDataNN.m
- rec_saveImdl.m
- selectMasurementsIMpattern.m
- selectMostSensitiveMeasurements.m
- setOxygenatorParams.m
- setupRunEIDORS.m
- swtest.m
- trainNNpositionOptimization.m
- viewOxygenatorFEM.m
- viewOxygenatorModel.m
- vis_el_featuresNNcorrelation.m
- vis_el_selectElPosIMP.m
- vis_el_targetsNNtraining.m
- vis_el_trainNNelectrodes.m
- vis_exp_FEMmodels.m
- vis_exp_electrodeSets.m
- vis_exp_preliminaryExperimentsAnalysis.m
- vis_exp_preliminaryExperimentsMeasurementSelection.m
- vis_exp_targetDistribution3D.m
- vis_ext_activationFunctions.m
- vis_ext_barPlot.m
- vis_ext_oxygenatorRadials.m
- vis_rec_GREITFoM.m
- vis_rec_GREITanalysis.m